Proceedings of:

Mechanisms and Controls for Ultraprecision Motion

1994 Spring Topical Meeting

April 6-8, 1994
Westward Look Resort
Tucson, Arizona

The American Society for Precision Engineering (ASPE) is a multidisciplinary professional and technical society concerned with research and development, design, manufacture and measurement of high accuracy components and systems. ASPE activities encompass relevant aspects of mechanical, electronic, optical and production engineering, physics, chemistry, and computer and materials science. Membership is open to anyone interested in any aspect of precision engineering.

Founded in 1986, ASPE provides a new focus for a diverse but important community. Other professional organizations have covered aspects of precision engineering, always as a sideline to their principal goals. ASPE is based on the core of generic concepts necessary to achieve precision in any application; independent of discipline, ASPE intends to be the focus for precision technology — and to represent all facets from research to application.

ASPE — The American Society for Precision Engineering
401 Oberlin Road, Suite 108
P.O. Box 10826
Raleigh, NC 27605-0826
Phone (919) 839-8444 Fax (919) 839-8039

Preface

This book comprises the proceedings of the 1994 Spring Topical Meeting. The contributions reflect the authors' opinions and are published as presented to ASPE, without change. Their inclusion in this publication does not necessarily constitute endorsement by the ASPE, or its editorial staff.

Individual readers of this book and nonprofit libraries acting for them are permitted to make fair use of the material contained in this book to be used in teaching or research; provided they copy said paper in total, as written by the author. Permission is granted to quote excerpts from the scientific or technical works in this book with proper acknowledgement of the source to include: the author's name, the book name, and the ASPE tag line. Reproduction of figures and tables is likewise permitted from the contents of this book, provided that the same acknowledgment of the same source and content is printed.

Any other type reproduction, systematic copying or multiple reproduction of any material in this book is expressly prohibited except with the written permission of the ASPE editorial staff, addressed to the Society's headquarters.

Printed in the United States of America
AMERICAN SOCIETY FOR PRECISION ENGINEERING

ISBN 1-887706-11-9

Corporate Members of the ASPE

3M Company
ADE Technologies, Inc.
Bausch & Lomb
Brown & Sharpe
Chardon Tool & Supply Company, Inc.
Contour Fine Tooling, Inc.
Cranfield Precision Engineering, Ltd.
Dover Instrument Corporation
Fabreeka International, Inc.
Lawrence Livermore National Laboratory
Moore Special Tool Company
Precitech, Inc.
Professional Instruments Company
Rank Pneumo, Inc.
Tencor Instruments
Zygo Corporation

1994 Spring Topical Meeting

Contents

Preface . . . . . *ii*

Contents . . . . . *iii*

Program . . . . . *iv*

Technical Paper Index . . . . . *v-vi*

Foreword . . . . . *vii*

Technical Papers *3-122*

Author Index *128*

1994 Spring Topical Meeting

Meeting Schedule

Tuesday, April 5		Wednesday, April 6	Thursday, April 7	Friday, April 8
	8:00	REGISTRATION	CONTINENTAL BREAKFAST	
	9:00 10:00	TECHNICAL SESSION I	TECHNICAL SESSION V	TECHNICAL SESSION VIII
		BREAK	BREAK	
	10:30 12:00	TECHNICAL SESSION II	TECHNICAL SESSION VI	TECHNICAL SESSION IX
		LUNCH		CLOSE OF CONFERENCE
	1:00 3:00	TECHNICAL SESSION III	OPEN FOR DISCUSSIONS	
		BREAK		
	3:30 5:00	TECHNICAL SESSION IV	TECHNICAL SESSION VII	
ON-SITE REGISTRATION AND REFRESHMENTS	6:30	REFRESHMENTS		
	7:30	DINNER		
	8:30 9:30	REVIEW & DISCUSSION REFRESHMENTS		

Technical Paper Index

Technical Session I
Wednesday, April 6, 9:00 - 10:00 a.m.

Welcome and Introductions
Conference Outline and Goals — *David H. Youden*

1. ***Nano-Drive: A New Kind of Air Bearing Based Transmission Gear***
   P. Langenbeck (INTOP) . . . . . *page 3*
2. ***High-Sensitivity Receiver for Increasing Multiplicity of Measurement Axes of Zygo's Heterodyne Interferometer***
   J. F. Beckwith (Lawrence Livermore National Laboratory) . . . . . *page 11*

Technical Session II
Wednesday, April 6, 10:30 a.m. - 12:00 p.m.

1. ***A Machine to Generate and Polish 8.5 Meter Mirrors***
   W. Davison, C. Kittrell, S. DeRigne (The University of Arizona Steward Observatory) . . . . . *page 14*
2. ***The Development of a Calibrated Atomic Force Microscope****
   T. H. McWaid, J. Schneir (National Institute of Standards and Technology)
3. ***Quiet Hydraulics for Ultraprecision Actuation***
   S. B. Peirce, H. Tran, M. Wiedemann, D. B. DeBra (Stanford University) . . . . . *page 20*

Technical Session III
Wednesday, April 6, 1:30 - 3:00 p.m.

1. ***Open Architecture Controls for Precision Machine Tools***
   B. N. Damazo, C. W. Yang, R. J. Gavin (National Institute of Standards and Technology) and D. Smith (Delta Tau Data Systems) . . . . . *page 26*
2. ***Open Architecture Controllers — a Development Platform for Machine Tool Control Applications***
   P. Orban, Y. Zhou (National Research Council of Canada), and I. Yellowley (University of British Columbia) . . . . . *page 32*
3. ***Precision Contouring Error Analysis***
   C. S. Wilson (Delta Tau Data Systems) . . . . . *page 37*

Technical Session IV
Wednesday, April 6, 3:30 - 5:00 p.m.

1. ***Retrofit of a 3-Axis Machining Center with a PC Based Controller****
   W. G. Brown, J. M. Edwards, A. A. Lopez (Los Alamos National Laboratory)
2. ***Master-Slave Positioning***
   G. Wyntjes, D. Mansur (OPTRA, Inc.) . . . . . *page 43*
3. ***Nanometric Motion Control of a Traction Drive***
   P. I. Ro, G. Rao, Q. Ma (North Carolina State University) . . . . . *page 46*

Technical Session V
Thursday, April 7, 9:00 - 10:00 a.m.

1. ***Development of Design Rules for Friction Wheel Drives***
   N. Rosielle (Eindhoven University of Technology) . . . . . *page 51*

*Paper not available at press time.

2. ***Experimental Analysis of Grinding Wheel Head Feed Mechanism on Plain Bearing Guideways with Force-operated Linear Actuator***
A. Kanai, M. Miyashita, Y. Kishimoto (Ashikaga Institute of Technology) . . . . . page 57

Technical Session VI

Thursday, April 7, 10:30 a.m. - 12:00 p.m.

1. ***Damping Characteristics of Air-lubricated Slideways for Ultraprecision Machine Tools***
S. Kato (Nippon Institute of Technology) . . . . . page 63
2. ***Low Cost, Highly Damped, Precision Linear Guideways Using Porous Carbon Air Bearings and Epoxy Replication***
M. Chiu, A. H. Slocum (Massachusetts Institute of Technology), B. N. Damazo (National Institute of Standards and Technology), and A. J. Devitt (Devitt Machinery Co.) . . . . . page 67
3. ***Do Hydrostatic Bearings Generate Mechanical Noise?***
D. H. Youden (Rank Pneumo, Inc.) . . . . . page 71

Technical Session VII

Thursday, April 7, 3:30 - 5:00 p.m.

1. ***Magnetic/Fluid-Bearing Stage for Atomic-Scale Motion Control***
D. L. Trumper (Massachusetts Institute of Technology) and M. Holmes, R. Behrouzjou, D. Batchelder (UNC-Charlotte) . . . . . page 78
2. ***Design Strategies for a Monolithic Micro-Tilt Face-Plate Piezo Flexure Stage***
H. Mizuno (NSK Ltd.) and A. E. Gee (Cranfield University) . . . . . page 83

Technical Session VIII

Friday, April 8, 9:00 - 10:00 a.m.

1. ***3-Meter Delay Line for Optical Interferometry in Astronomy***
J. M. Leblanc, M. Sghedoni (Aerospatiale), B. Lhenry (Framatome), P. Bourlon, A. Glentzlin (OCA), and M. Bonis, S. Mekid (UTC) . . . . . page 87
2. ***The Subtle Causes of "Apparent" Non-Repeatability***
H. Hauschildt (Lawrence Livermore National Laboratory) . . . . . page 92

Technical Session IX

Friday, April 8, 10:30 a.m. - 12:00 p.m.

1. ***High Precision Measurement System for a Rotary Table***
C. Zhang (University of Southampton) and F. Margrave (Lancaster University) . . . . . page 110
2. ***A Trial of Force Sensor with Actively Controlled Compliance***
K. Matsumoto, Y. Hatamura, M. Nakao (The University of Tokyo) . . . . . page 116
3. ***LLNL/Lion Precision LVDT Amplifier***
D. Hopkins (Lawrence Livermore National Laboratory) . . . . . page 122

Foreword

The 1994 ASPE Spring Topical Meeting deals with the very foundations of precision engineering. This year we examine the mechanisms which produce precision motion, and the control systems used to manage those mechanisms. The motions generated by the devices discussed here range in size from meters to nanometers, and the applications addressed run the gamut from astronomy to sub-atomic physics, with many stops along the way.

I am especially pleased by the number of presentations here which deal with controllers, as these systems are an integral part of precision engineering but they have not, until now, received an appropriate amount of attention within our society. Perhaps the seeds of interest generated here in Tucson will bear fruit at the upcoming annual meeting.

The Spring Topical Meeting is an informal gathering intended to be a forum where authors can report on ongoing work. Some of the results reported here may not be based on finished work. Because of this, and in keeping with the spirit of informality, I request that the individual authors be contacted prior to the use of their results in other publications.

David H. Youden
Meeting Chairman

Technical Papers

Nano - Drive
a new kind of air-bearing based transmission gear

Dr.-Ing. Peter Langenbeck
D-88699 Frickingen

1. Summary

Uniformity of motion of better than $\Delta v/v = 0{,}05\%$ at low speed (less than 1mm/sec.) along distances in the order of some hundred mm, and microstepping in the order of a few nm are stated needs in micromechanics. These needs occur typically in lithography and in NC micro-machining. Yet, these design goals are hard to accomplish using known drive techniques like worm wheels, belt drives and DC torque motors. Most suffer from stick-slip and relative speed variation resulting in positional inaccuracies. A new air-bearing based friction solution for a transmission gear is presented.

2. State of the art

Some problems are well solved by harmonic drive and cyclo-drive. They combine high torque with good uniformity of motion. Yet, the tooth wheel character still causes periodic speed variations, Fig.1. Microstepping is further impeded by play and back-lash.

Several results indicate that friction wheel-drives closely approach the desired performance, /1/. Their transmittable torque is usually low.

A popular approach to the above design goals is the combination of a normal leed screw drive with a piezo pushing element - requiring involved controls.

3. Nanodrive - a new solution

Our goal is to provide an inexpensive gear for rotary to linear transmission of utmost mechanical peformance in terms of uniformity and micro-stepping potential, prior to electronic controls taking place. The requirements to be fullfilled are:

- no stickslip, no wear - no sliding, only rolling contact
- high torque
- large speed range at low speed
- sub-arc-sec stepping potential on the rotary-drive
- no periodical speed variation (Fig.1).

The concept is explained by the schematic in Fig.2. It shows an air-bearing supported journal shaft in a housing, with a rotatable external air-pressure feed manifold. As the air- pressure supply gets obstructed in one peripheral location, pressure distribution in the annular gap will become non-uniform, building up a maximum on the side opposite to the obstruction. This causes the shaft to be grounded against the housing wall along a cylinder line, where pressure is min.. As the pressure supply obstruction is moved to the neighbouring inlet, clearing the first one, the zone of contact between shaft and housing will then be rolled to that location as well. One full revolution of the obstruction, i.e. of the pressure high, will cause the shaft to be rolled along the housing wall for an amount equalling the difference between housing and shaft circumferences. The two rotations have a transmission ratio of:

$T = (u_2 - u_1)/u_2$ $\quad T = \Delta D / D$

With D = 100mm and $\Delta D = 10\mu m$ (typical with air-bearings)

T = 0,01/100 = 1/10000, and dT = $d\Delta D/D = 10^{-5}$,

allowing for a 10% air-gap non-uniformity $d\Delta D$.

Uniformity of 10% in a gap being itself rather small is in the realm of normal air-bearing based compliance. As a matter of fact, a 10μm total gap may have much better uniformity than only 10%, as is evidenced by Fig.3 showing the TIR-curve of a cylinder ground on an air-bearing spindle. More likely the gaps non-uniformity will be less than 1% (=0,1 μm out of round), resulting in dT to be in the order of 10^{-6}.

The friction is independent of D, as it is a function of force and friction coefficient μ only. It may be estimated using the force executed by the hemi-cylinder (D,L) loaded with pressure p against the housing cylinder wall:

With μ = 0,1; p = 50N/cm D = 10cm; L = 5cm being typical for ultra precision techniques.

F = μ.p.D.L. = 250N, and torque M = 1250Ncm

Some features of such a transmission gear are evident:

1. No sliding - only rolling contact.
2. Low specific load - much different from other friction roller drives.
3. Torque controlled by fluid pressure, without loading or sur-charging the device providing the rotation of the obstruction.
4. No harmonics, no periods.

5. Both mating surfaces are bound to become gradually smoother as in rolling and/or burnishing /3/.
6. Voiding the obstruction lets the shaft rotate freely on its air-bearing, providing for a direct fast drive.
7. In-put/output drive directions are in opposition.

The cross-section of a real design applied to turntables is shown schematically in Fig.4. Here, the ball-bearing supported driving journal must support an unsymmetrical force upon the transmission ring, which itself is loaded against the outer transmission zone. The asymmetric load may be accomplished by air-pressure or by magnetic force. Independent of method of force-transmission will the transmission ring always run with rolling contact only. The bearing of the driving journal might again be an air-bearing, having to support the radially asymmetric force.

A further considerable reduction of transmission ratio is provided by the INTOP-Watt air-bearing spindle shown schematically in Fig.5 in its outlet restrictor mode. One will observe a nutation of the spindle rotor around its spherical center as a consequence of asymmetric load. The flat disc (diameter D) might even be grounded upon some excentric overload. And if the contactlessly exerted overload is made to rotate one will generate a rotation of the spindle rotor. The effective "air gap" is the difference between D and its projection after nutation: D = h.sin The transmission ratio now is $T = (h^2/r)/r = (h/r)^2$

It is seen that T may range in the order of $1:10^8$.

A demonstrator unit according to Fig.5 was shown at /4/ new products presentation. This unit produced 1 arc.sec. rotation upon one full revolution of the drive.

The eccentric load may be an asymetrically applied flat air-bearing. Or a permanent magnet. Or even mechanical devices like a manifold of sequentially loaded pneumatic pistons or other pushers connecting the device to nc-systems for microstepping.

Conclusion

Schematic and execution of a transmission gear were reported, which provide angular resolution of 1:10^{-4} to 10^{-8} with potential for high load, direct fast drive and for microstepping. Uniformity of motion of a gear produced on and operated with air-bearings is expected to be in the order of 10^{-3} %.

References

/1/ M.Weck, T.Bispink Untersuchung von hochgenauen, langsam laufenden Vorschubantrieben für den Submikrometer-Bereich.
Berichte der Forschungsgemeinschaft Ultrapräzisionstechnik am IPT/Aachen, Feb.92.

/2/ Tbd.

/3/ N.H.Loh + S.C.Tam Effects of ball burnishing Parameters on surface finish, a literature survey Prec. Engg. 10, 1988, 215

/4/ Langenbeck, P. An ultra-fine infeed controller Proc. of the 6th Inter. Prec. Engg. Conference Braunschweig 91, 347.

/5/ H. Moll
Schrittmotoren mit hoher Winkelauflösung F + M 86 (1978) 156

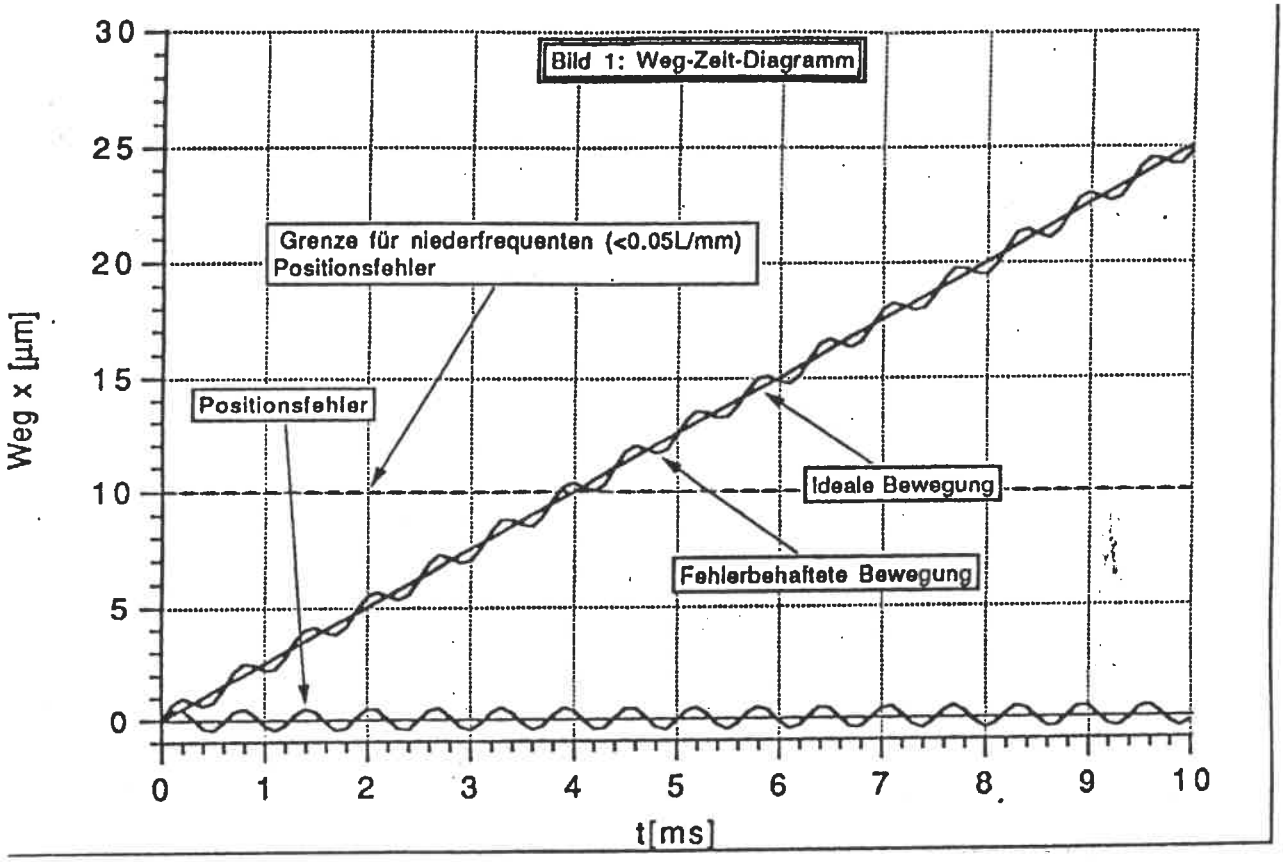

1. Displacement versus time diagram of a rather good real drive exhibiting residual positional errors connected to speed variation.

3 1 2 6 4 5

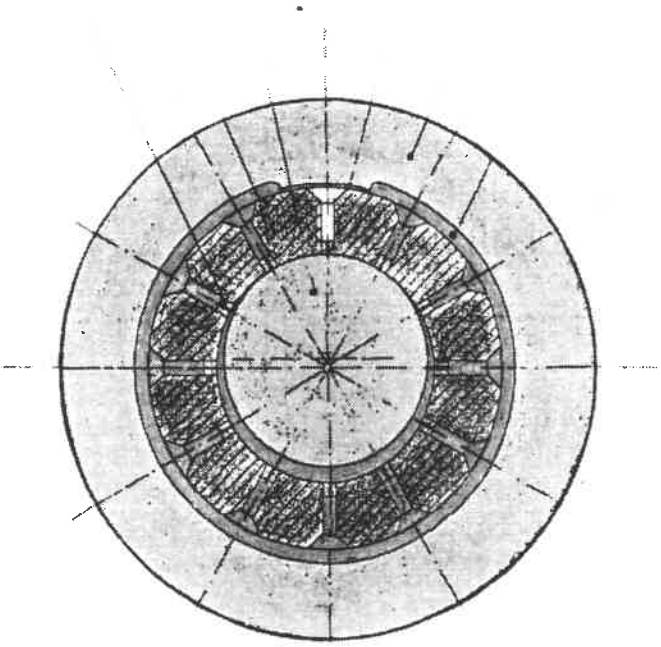

3. Nanodrive - schematic.

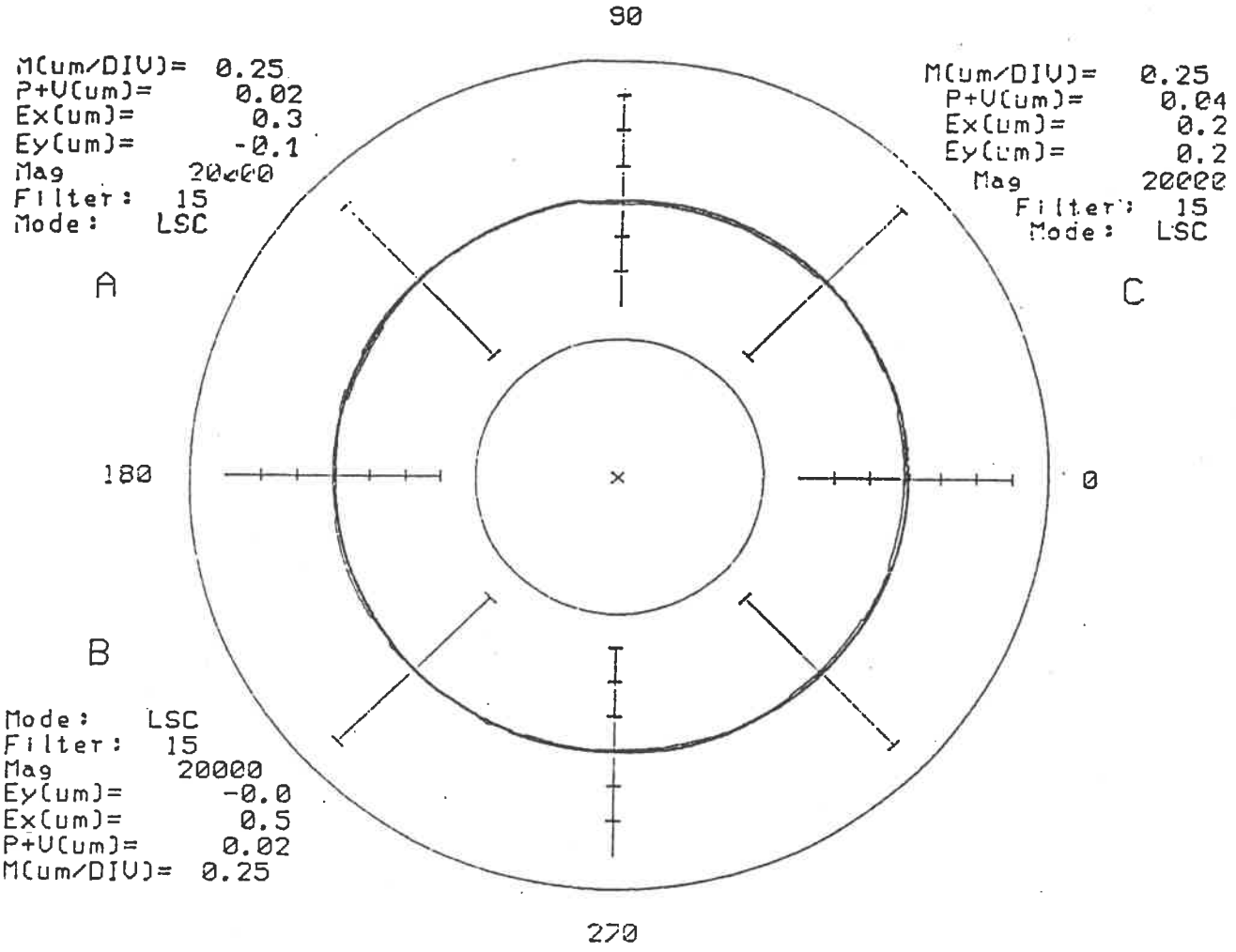

2. TIR - curve of a cylindrical component used to design and build Nanodrives.

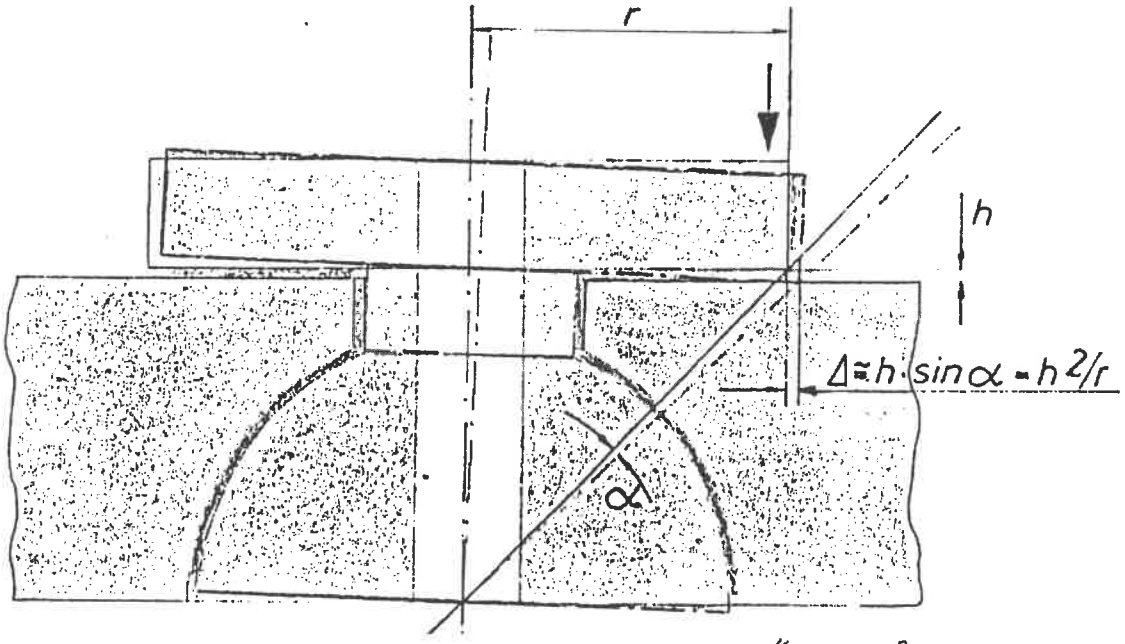

5. The INTOP-Watt spindle as a basis for 1:10^4 to 10^8 Nano-drive.

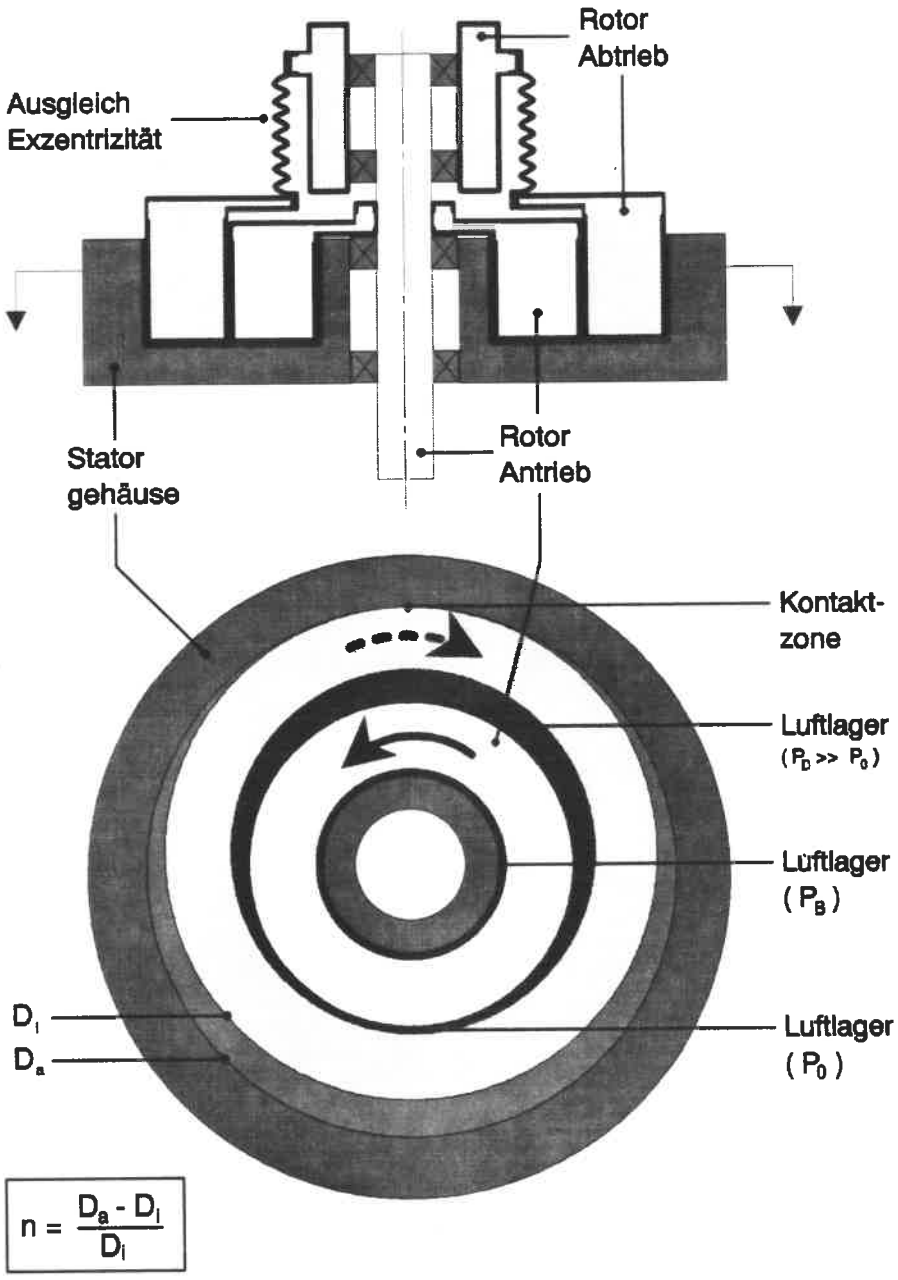

4. A practical solution to Nanodrive.

HIGH-SENSITIVITY RECEIVER FOR INCREASING MULTIPLICITY OF MEASUREMENT AXES OF ZYGO'S HETERODYNE INTERFEROMETER

JOHN F. BECKWITH
LAWRENCE LIVERMORE NATIONAL LABORATORY
MARCH, 1994

ABSTRACT

The number of measurement axes which can be simultaneously operated from a single laser source is limited by, among other factors, the minimum optical power required at the electronic receiver which detects the interferometric phase of the recombined measurement and reference beams. A high-sensitivity receiver has been designed and operated which decreases this required minimum power by about a factor of twenty for the Zygo Heterodyne distance-measuring interferometer. The receiver utilizes a tuned front end and a low-noise DMOSFET for the first amplifier stage. The tuned circuit, however, reduces the maximum slew rate, but this can be easily traded off against the increased sensitivity while maintaining a net increase in their product. Both the input and output employ fiber optics for maximum noise immunity. The fiber-optic connectors and output signal are compatible with Zygo's VME Measurement electronics.

INTRODUCTION AND SUMMARY

The most common architecture for a high-speed optical receiver is a PIN photodiode driving a transimpedance amplifier. This provides a broad bandwidth due to the low input impedance of the TIA shunting the parasitic capacitances of the PIN diode network, while also offering good sensitivity because this low impedance is achieved by the Miller effect upon a much larger value of feedback resistor around a quiet voltage amplifier. The thermal noise currents of this resistor are the dominant source of amplifier noise rather than the much larger noise currents that would be expected from the low value of input resistance. However, there are many applications in displacement-measuring interferometry where this large bandwidth is not needed and may be traded, in varying proportions, for increased receiver sensitivity by utilizing a different front-end configuration. Such a receiver was designed and built to enable a single Zygo laser head to drive the very complex interferometer system on the Large Optics Diamond Turning Machine at Lawrence Livermore National Laboratory. This receiver operated without signal degradation down to 200 nanowatts of optical power at the fiber optic pickup and maintained lock, but with some position noise jitter, to less than 100 nanowatts.

BLOCK DIAGRAM DISCUSSION

In reference to Fig. 1, a fiber optic pickup gathers the interferometer's output beam and directs it to a low capacitance PIN diode photodetector which in turn drives a variable gain FET/Bipolar Cascode input stage, the key to the high sensitivity, which will be discussed in more detail in the next section. From this point on the blocks are conventional: A commercial transimpedance amp, normally the first stage of an optical receiver, provides additional gain. An amp/limiter stage follows to minimize phase shift resulting from possible amplitude variations, and finally a power stage is used to drive the LEDs which feed the output fiber going to the optical receiver port on the Zygo VMEbus Measurement Board. Due to conversion inefficiencies from light to current and back to light, a very large overall electronic gain of about 120 db is required. To maintain stability, very extensive decoupling and isolation techniques are required.

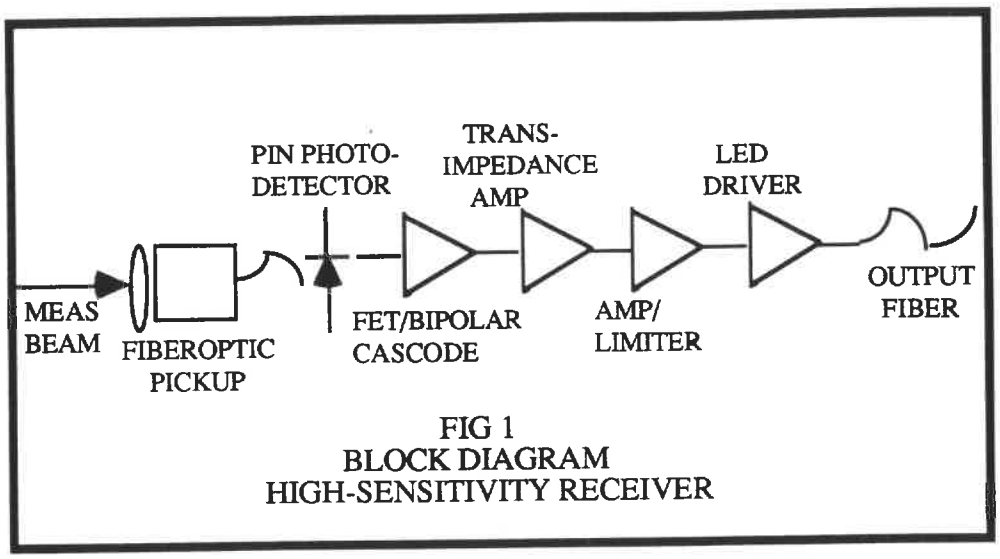

FIG 1
BLOCK DIAGRAM
HIGH-SENSITIVITY RECEIVER

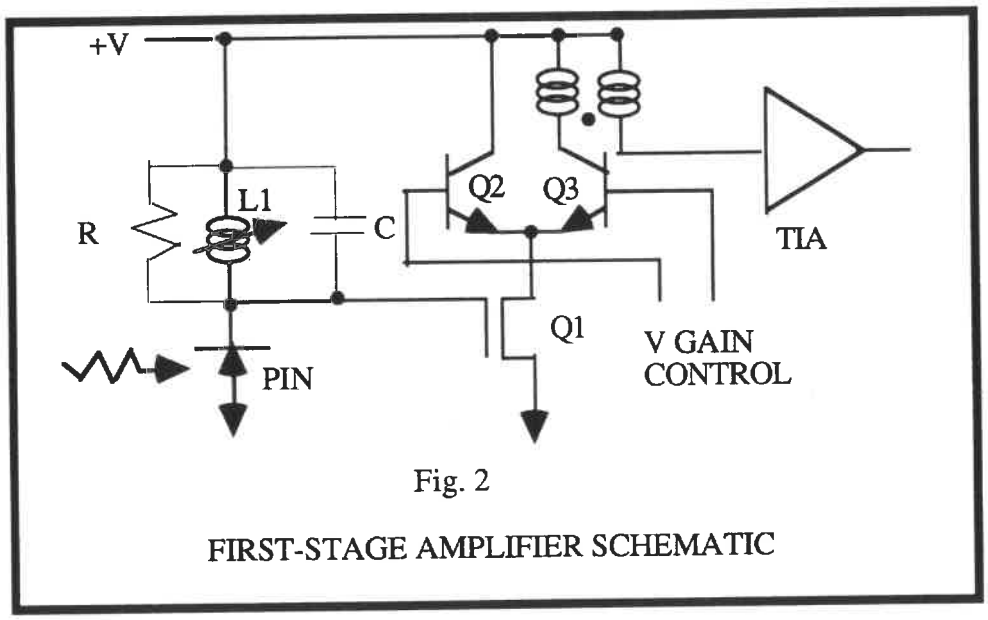

Fig. 2

FIRST-STAGE AMPLIFIER SCHEMATIC

FIRST-STAGE AMPLIFIER DISCUSSION

Fig. 2 shows a skeletal schematic of the key first-stage amplifier. The capacitor C represents the total capacitance of the input node including that of the FET, the PIN diode, the PC board, and the coil. The resistor R represents the losses of coil L1. The value of L1 is chosen to resonate with C at the optical reference frequency (20 Mhz for the Zygo laser source). The parallel resonance of this structure provides a very high

impedance to the PIN diode equal to the value of R when the input frequency is near the resonant frequency. Since the PIN diode is a current source controlled by the optical input power, this current in effect flows through R and develops a very high voltage on the gate of the FET Q1. This gate voltage is then converted to the drain current by the g_m of the FET and then divides between the collectors of Q2 and Q3 where it appears in the form of a current source. The Q3 collector current is transformer coupled to the low impedance input of the next stage transimpedance amplifier. Q2 and Q3 also serve to keep the drain impedance low to maintain high-frequency response (cascode action) and by varying $V_{GAIN\ CONTROL}$ the gain of the first stage can be varied over a wide range to allow for different input optical power levels not saturating the transimpedance amplifier. The FET Q1 was chosen to be a DMOSFET because of its low capacitance, low noise, and high g_m. The noise sources of this stage are dominated by that of the coil loss resistor R.

DESIGN EQUATIONS

The input variables and their representative values for this amplifier are:

f_0.....the optical reference frequency.....20 Mhz
C.....the total capacitance of the input node.....5 Pf
Q.....the Q of the coil which resonates C at f_0.....80
g_m.....the transconductance of the DMOSFET.....10 ma/volt

In terms of these the key desired variables and their rough values are:

$R=Q/(2\ Pi\ f_0\ C)$.....125Kohms
Max current gain of first stage= $g_m R$.....1,250
Spectral noise current density (input referred)=sq root (4kT/R).. .36 Picoamp/root Hz

The parallel resonant nature of the amplifier front end does limit the allowed Doppler shift resulting from retroreflector motion to plus or minus one half of its bandwidth (f_0 /Q), or about plus or minus 125Khz for this example. Note that this is not the noise bandwidth as that is determined by the much narrower bandwidth of the phaselocked loop on the Zygo Measurement board. The above equations provide the guide for trading sensitivity for Doppler shift if this is necessary.

This work was performed under the auspices of the U. S. Department of Energy by Lawrence Livermore National Laboratory under contract No. W-7405-Eng-48

A MACHINE TO GENERATE AND POLISH 8.5 METER MIRRORS

Warren Davison, Cary Kittrell, Scott DeRigne
Steward Observatory
University of Arizona
Tucson, AZ

ABSTRACT

Producing large optics, calls for a balance of precision, efficiency and safety. We have one machine that serves both our generating and polishing needs. The LOG (used to be the Large Optical Generator) now has been modified to perform tasks as varied as generate and measure 8.5 meter blanks to 10 micron rms precision, grind glass with a removal rate up to 4 cubic centimeters per second, precisely move a stressed lap with a 3/4 ton drag in any pattern that is desired, and perform these tasks on a honeycomb cast blank which is so fragile that it is impossible to pick it up by its outside edge.

INTRODUCTION

The University of Arizona has undertaken the manufacture of several large mirrors for astronomical telescopes. State of the art mirror specifications are very exacting. They must not only be finished to a figure that can be measured in tens of molecules, but also have a low thermal mass and time constant to reduce mirror "seeing" turbulence created by heat from the mirror. They have short focal lengths, (focal ratios near f/1) to allow stiff optical support structures and compact enclosures, giving rise to asphericity over 1 mm, and making accurate polishing impossible using conventional techniques.

Generating the blank requires a mixture of aggressive tooling and high precision. Safety is a paramount issue since the cost of the blank is high and the damage that can be done is catastrophic. The control system includes a redundant computer for cross checking, redundant encoders on the horizontal and vertical axes, numerous hardware switches and meters to detect hazardous conditions, and several layers of software protection against excessive speeds, proximity to the glass and failure to control position.

Polishing the mirror requires positioning the stressed lap to a millimeter, while controlling vertical forces and moments. This is done by active machine position control, a passive linkage and three force actuators. The safety of the blank requires measurement of the three forces, the three moments and three distance measurements between the lap and machine plus the position of the machine axes.

LARGE OPTICAL GENERATOR

The LOG is a large custom made grinding machine with a 5 meter horizontal travel, a 1.5 meter vertical travel and a table that can swing 9 meters (Figure 1). The ways are rectangular steel with Turcite friction slide pads. The horizontal and vertical stages are driven by ball screws which can exert 4,400 lbs and 17,600 lbs respectively. Both axes have

a rotary encoder on the screw and a linear encoder attached to the stage. The rotary table has a 500 to 1 gear ratio drive which can apply 22,000 ft-lbs of torque.

For generating, the LOG has a 15 hp grinding spindle that is tilted 11 degrees out of plane. The tilt improves the cutting geometry and allows a better finish.

For polishing, an additional rotary axis is added to the carriage that is capable of 7,000 ft-lbs of torque. This axis rotates the stressed lap while the LOG moves it across the mirror surface. The stressed lap is basically a 60" diameter by 2" thick aluminum plate with 18 computer controlled mechanisms that can bend the plate as much as a 1/4" to accurately conform to the shape of the mirror.

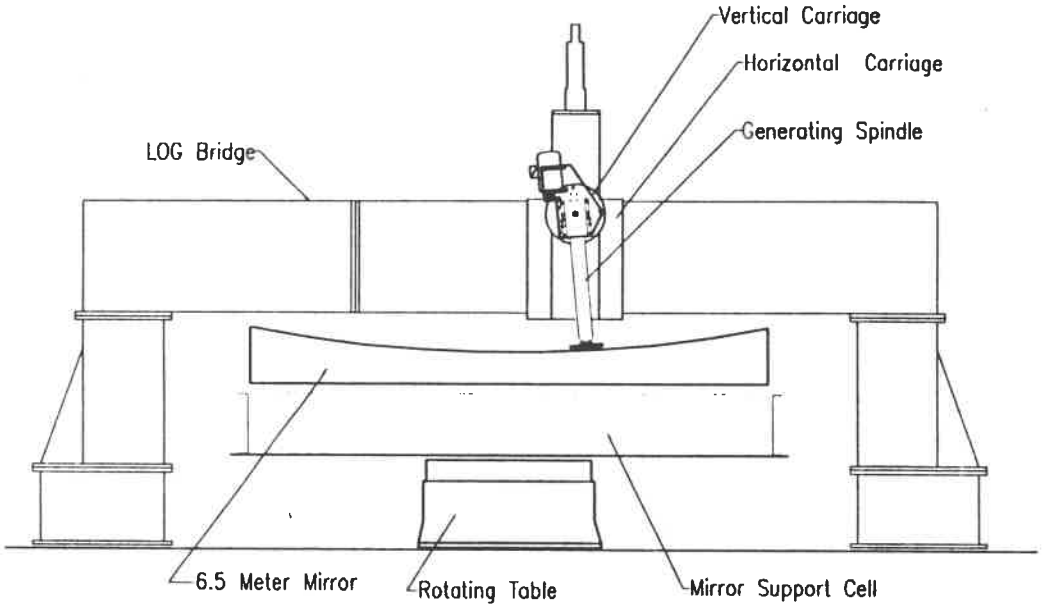

Figure 1

CONFLICTING REQUIREMENTS

Combining the functions of several machines leads to conflicting requirements and compromises. Computer control provides the versatility required in this environment, which could not be given using a turnkey system, and is more useful than fixed speed systems. The down side is that it increases the possibility for error. The full three axis machine used also provides greater versatility than with a mechanical geometry tracing machine. Adopting such a machine with high capacities sacrifices some of the inherent safety of single purpose rote mechanical machines. This does not imply that rote machines are safe, only that there is less safety in a machine with greater capabilities.

We have successfully polished three 3.5 meter mirrors, though our technique and requirements continue to evolve. Conventional means would require several machines and

extremely large buildings to house them in. It would require much longer time to produce a mirror. Time means money and also risk. The more time the mirror spends under the machine, the greater is the potential that a bolt or small screw may loosen and fall on the surface. The enormous cost of this compromise would not make this process feasible. The only logical choice is to use a compact versatile automated system and place additional effort into safety.

GENERATING

Generating is a process where a diamond grinding wheel removes glass rapidly, producing a blank of defined dimensions. Generating is an inherently dangerous process for several reasons. The glass to tool contact surface is small, so small forces produce large stresses. The machine is very rigid, so small deflections produce large forces. There is a large amount of stored power in both the moving mirror and grinding wheel. Numerically controlled machinery can move anywhere in its envelope, even right through the blank. Failures are not easily tolerated, even a small depression is a flaw in the final mirror and breaking the glass is a very real possibility. There are traditional solutions to some of these concerns but the most common approach has been to accept a low production rate with higher risk to the blank.

POLISHING

Polishing our mirrors requires us to move the stressed lap over the entire surface. The machine must provide hundreds of pounds of side forces and torques while controlling axial forces and moments. The LOG is very stiff and provides position very well but if it is connected to a lap, any position error will be translated to a huge force error. There must be a connection that can move vertically and still provide all the torque and drag forces needed. Three sets of four bar linkages let the distance between the lap float. The safety risks to the mirror are mainly from applying too much force or moving the lap off the edge of the mirror.

FOUR BAR LINKAGE

One of our polishing goals is to be able to use our knowledge of the mirror figure and our computer control of the equipment to decrease the polishing time. To do this we have to control the forces and moments that go into the lap. The ideal LOG to lap connection would transfer the drive torque, provide the drag forces at the glass interface in a direction parallel to the glass, and have the remaining normal force and two tilting moments either zero or intentionally controlled. Figure 2 shows one of the 3 (one every 120 degrees) four bar linkages that drive the lap. This linkage applies the drag force at the instantaneous rotational center and that center moves with the lap when it is tilted. This means that when the lap is tilted the driving force and the direction of the free axis are tilted also. The stressed lap is fairly stiff (a 2" thick solid aluminum plate) but could be distorted if you did not apply the drive forces correctly. The best place to apply forces is in the center plane of the plate so drag forces do not induce bending, that is why the links terminate with balls deep in the plate. The lap shown in figure 2 has an extra link in the

center, so that the effective pressure of the lap on the glass can be varied continuously. This allows you to increase the pressure while over high spots and reduce it over lows. This is a very effective tool to reduce azimuthal figure errors. There exist some situations which our linkage could not correct for, for example the lap moving part way off the mirror and varying the pressure across the lap to polish on radial figure zones smaller than the lap diameter. We are currently constructing a linkage with three actuators on the three linkages so we can vary the two tilting moments and the normal force. This should give us enough control to maintain the desired pressure and gradient and achieve even faster polishing times.

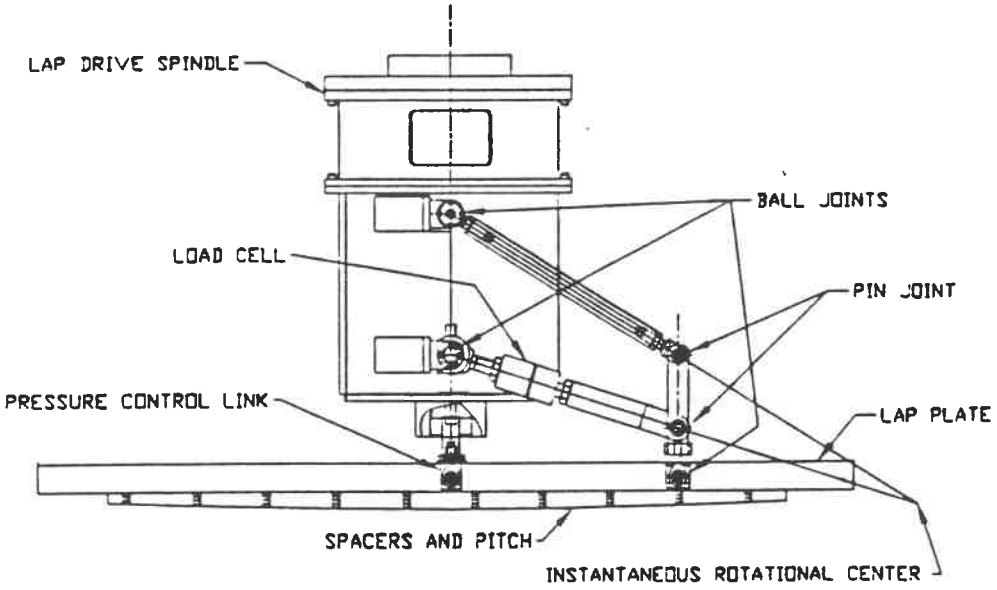

Figure 2

Four bar linkage to drive a lap with the LOG

SAFETY DEVICES

We have several schemes and devices to lower the risk to the mirror while it is on the LOG.

1. There are two computers, one to run the LOG and one to check on the first computer.
2. There are two encoders on each translational axis, a rotary one on the motor and a linear one on the slide, which must agree.
3. Both computers know where the mirror is and have checks on commanded positions, velocities, accelerations, driver boards, each other and time.
4. Different algorithms in the two computers.
5. Fail-safe brakes on all axes.
6. For generating there are additional sensors for tool motor current (high and low) monitoring, a coolant flow switch and a roller that rides on and measures the distance to the glass.

7. For polishing there are sensors for lap torque and drag, distance sensors from lap to LOG and a limit switch to keep from running off the edge of the mirror.
8. Hardware panic stop driver that lifts the spindle immediately when a problem is detected.

CALIBRATION

The LOG is a precision machine tool with both linear axes accurate to a few thousandths of an inch over their entire travel. The generating and metrology that we do on mirrors requires higher accuracies. To make the machine more accurate we chose to apply open loop corrections to the commanded positions from the computer.

The horizontal corrections come from several errors which can simply be added to give you a final position. We adopted a convention for describing them that has the first term being the axis you apply the correction to (Δx for horizontal, θx for horizontal tilts, Δz for vertical, and θz for vertical tilts), and the second term is the axis the correction came from (x for horizontal and z for vertical). This allows us to describe the error in the horizontal encoder as Δx,x (simply the correction value Δx at the x position of the encoder). The look up table would have entries at set intervals, say .25", which would be the x value, and a correction value of Δx would be added to your target value to get to the correct position. The horizontal is not perfectly straight or aligned, so as it travels horizontally it moves up and down and tilts back and forth. The up and down motion would be a vertical correction that depends on horizontal position, or Δz,x. The tilts have a second term in them which is the distance from the calibration line (where we measured the horizontal position) to where you are currently operating. The distance times the tilt is the horizontal correction. Unfortunately the distance is some constant that you measure during setup (DZ1) plus the vertical distance that vertical stage is currently at (z). The vertical straightness contributes to the horizontal error, plus the vertical tilt times any vertical distance that is different from the calibration point (DZ2). The vertical corrections are similar but since the vertical stage travels on the horizontal, the tilt arm distance is a constant. The total corrections are as follows:

$$\text{Horizontal Correction} = \Delta x,x + \theta x * (DZ1 + z) + \Delta x,z + \theta z * DZ2$$

$$\text{Vertical Correction} = \Delta z,z + \theta z * DH + \Delta z,x + \theta x * DH$$

If you are lucky some of the terms are small enough to ignore, and if you can calibrate at your use position you can probably minimize these equations. Figure 3a. shows one of the six basic calibration tables for the LOG and residual errors after the correction is made (Fig 3b.). This is my worst correction table and is caused by a combination of alignment and a large moment arm on a small tilt. The residual correction error shows that the error is mostly repeatable or the reduction in magnitude would not be as dramatic. Note that the angles are in radians and small angle approximations are used. If more accuracy is needed or tilts are large, it would be best to use a term which had a constant angle in it for the rotation term (RZ2 * sin (θz + θ) in place of (θz * DZ2), where RZ2

is now the radius from the intersection of the two calibration lines and θ is the base geometry of your particular set up.

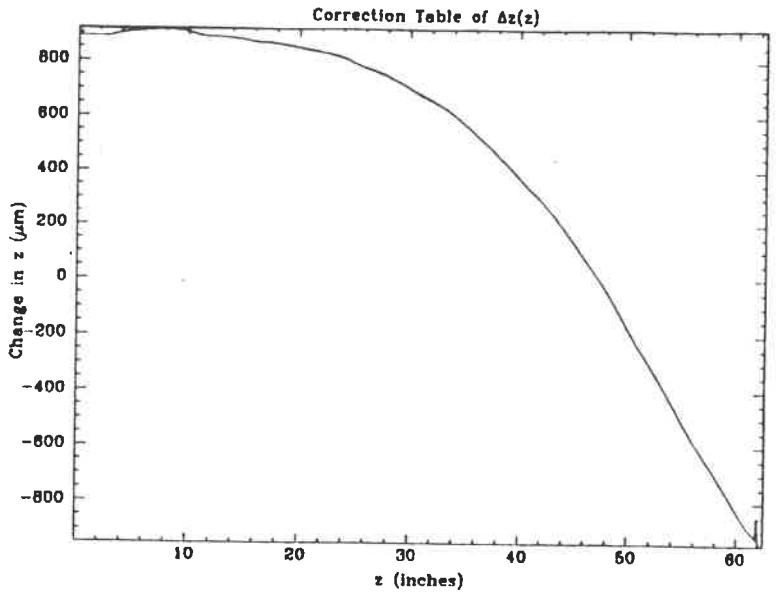

Figure 3a.

Correction table for the vertical error in the vertical direction

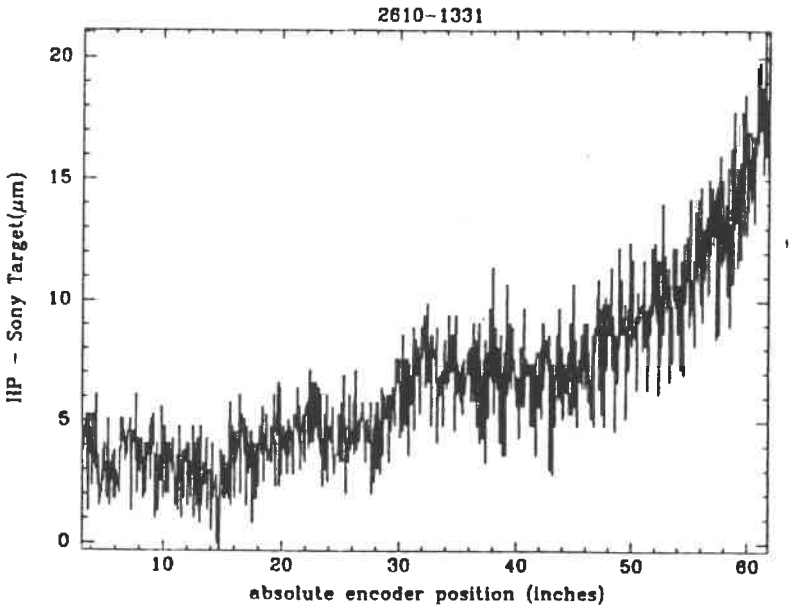

Figure 3b.

Residual error in the vertical direction after the correction table is applied

Quiet Hydraulics for Ultraprecision Actuation

Scott B. Peirce , Hy Tran, Michael Wiedemann, and Daniel B. DeBra
Department of Aeronautics and Astronautics
Stanford University, Stanford, CA

Abstract

Hydraulic actuation offers potential thermal advantages in ultraprecision applications. The working fluid can also carry away the heat generated due to inefficiencies in the actuator. Hydraulic actuation is also compatible with oil shower for temperature control. We have developed a family of laminar flow based hydraulic actuators for ultraprecision applications: a laminar flow spindle motor, a fast, short-stroke linear actuator, and hydrostatic carriage ways with built-in provision to correct for straightness and yaw error motions. The straightness and yaw error signal is also generated hydraulically with a differential oil gage sensor and a reference straightedge. Though hydraulic actuation is equally applicable to a variety of ultraprecision machines, we have used diamond turning as a means of evaluating this technology. Without temperature control, we have achieved $R_a \approx 25$ nm.

Introduction

Of the many considerations important in designing precision machine tools, two remain difficult challenges: constant and uniform temperature, and vibration. Temperature changes alter critical dimensions due to thermal expansion, and vibrations induce undesirable distortions in machinery or workpiece. The use of hydraulics is a means of attacking both these problems with a single design philosophy. With hydraulic actuation, the working fluid carries away waste heat generated by inefficiencies. There are many other design requirements for machines and hydraulic devices can be designed to perform favorably for these too. For example, pressurized hydrostatic bearings are unequalled for smoothness, stiffness, and crash survivability. Figure 1 shows the expected stiffness of an externally pressurized bearing as a function of frequency.

Commercial hydraulics are typically used where maximum power is needed in the most compact package—for instance, construction equipment, or aircraft control surfaces. Therefore, conventional hydraulic actuation systems are designed for maximum efficiency and power density. They use orifice modulated valves, which rely on turbulent (or even choked) flows. This makes them unsuitable in the quiet environment needed for high precision.

In precision engineering applications, power efficiency is not a primary consideration: smoothness is. This led to our development of laminar flow based actuators. Our philosophy has been to use laminar flow, and laminar flow modulation (no orifice or turbulent flow) for control. Furthermore, our actuators do not use positive displacement, which would lead to torque or force ripple. Finally, by proper choices of clearances and viscosity, and by combining cavity closures with externally pressurized bearings, we developed designs with no seals which would introduce stiction.

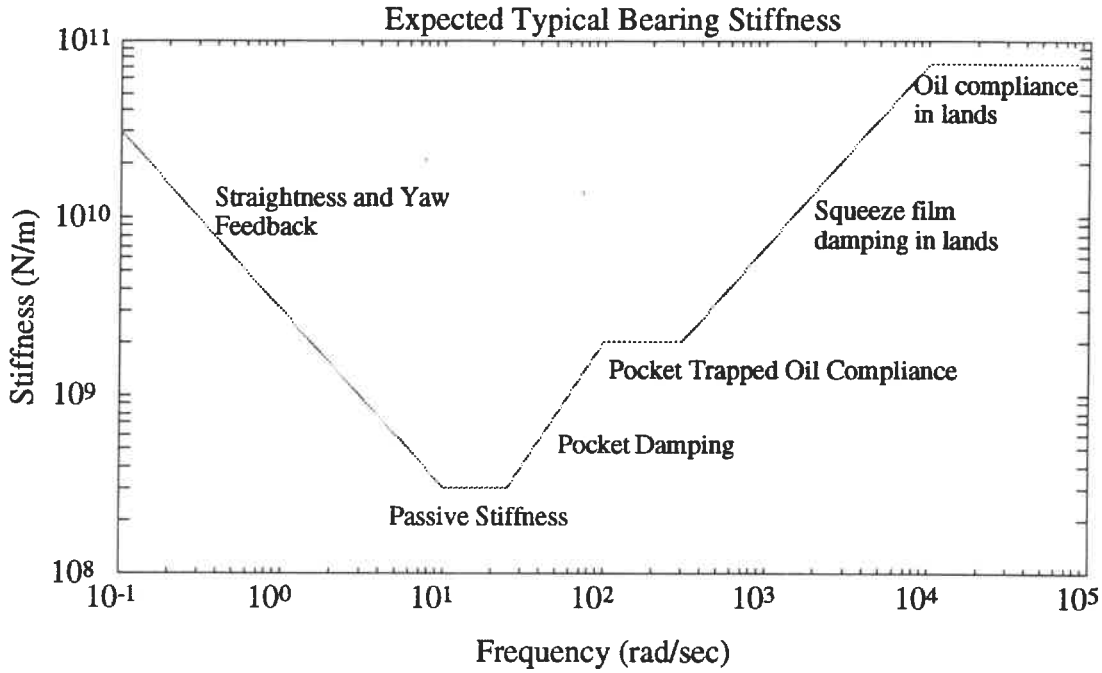

Figure 1: Bearing stiffness as a function of frequency

Case I: Laminar flow spindle motor

For precision machining, for example diamond turning, one must cut a workpiece with high degree of repeatability and achieve an optical quality surface finish. Existing electric motors and conventional hydraulic motors connected directly to the spindle produce vibration and/or thermal errors. Either may limit the repeatability of a machine which adversely affects its ability to produce parts of optical quality. A comparison of drives is given in Table 1 showing the potential advantage of a laminar flow motor over other types.

A laminar flow motor uses the viscous shear force generated in a narrow circumferencial channel (0.5 mm) to drive the spindle. Its torque output should be ripple free. Heat produced by inefficiency is carried away with the fluid. The maximum theoretical efficiency of this type of a laminar flow motor is derived as 33.3%. Therefore it is desirable to maximize operational efficiency of the motor and minimize friction loss in the motor and bearings. Leakage is unavoidable with finite clearances, but excessive leakage causes unnecessary pumping loss. We control the leakage through a combination of choice of viscosity (0.1 Pa) and clearances (order of 40 μm). A power output of 250 watts at a rotating speed of 100 rad/sec (955 RPM) was chosen as the design goal for the demonstration motor [Figure 2].

A maximum overall efficiency of 17.5% has been achieved experimentally for a demonstration laminar flow motor. The difference from the theoretical maximum is due to shear loss and leakage across the lands. The laminar flow motor is supported by hydraulic bearings with a specified stiffness of $1x10^6$ lb/in. ($1.75x10^8$ N/m) in the axial direction and one quarter of this value in the radial direction to overcome external loads. Chen [1985] achieved a repeatability of approximately 2.5 μin (64 nm) in the

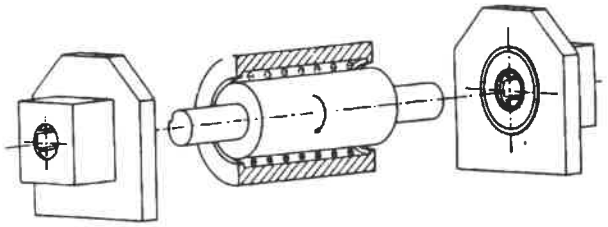

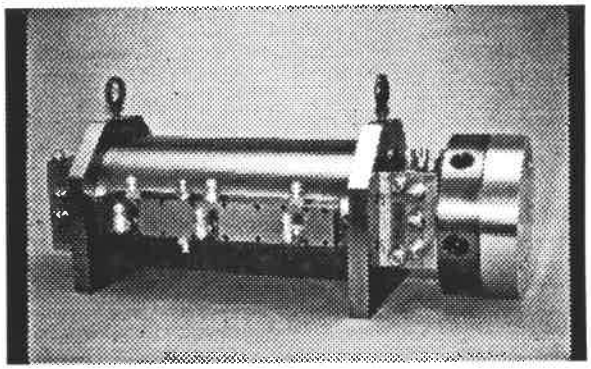

Figure 2: Laminar Flow Motor

	Efficiency	Heat in Rotor	Side Forces and Cogging Effects
DC Motor	High	Low	Highest
AC Induction	High	Medium	Medium
Brushless DC	High	Low	Highest
Eddy Current	Low	Highest	Lowest
Hydraulic Motor	High	N/A	Medium
Laminar Flow Motor	Low	N/A	Low

Table 1: Comparison of Motors

radial direction and is approximately 1.0 μin (25 nm) in the axial direction without any filtering of the hydraulic fluid. The repeatabilities in both directions are in the category of ultra precision machining.

Case II: Fast, short stroke linear actuator

To achieve optical quality in both figure and finish, the tool position must be controlled very precisely -- to about 1/10 of the wavelength of light (50 to 75 nm). There are two cases where a fast tool actuator can be useful: for non-circular cutting, or for compensating for errors in spindle motion.

Non-circular cutting involves moving a tool in synchrony with spindle revolution on a lathe. This allows fabrication of non-axisymmetric parts on a lathe. Correction for spindle error motion requires synchronizing tool position with spindle angular orientation. A small, fast actuator can be used for fast synchronous motion, while the slower, more massive carriage is used for slow feed.

The short stroke actuator that we have designed complements the other hydraulic actuators, bearings, slideways, and other equipment designed at Stanford. Since we are interested in a small span of motion, we chose to eliminate seals or bearings by designing a flexural piston: a diaphragm. To constrain actuator motion and to provide mechanical interface to the toolholder, we supported the tool with a flexure. The flexure is a parallelogram flexure, stiff in all but one degree of freedom. The stiffness of the diaphragm and captured oil is increased by the flexure. Trading stresses, stiffness, and range, an acceptable design for the diaphragm and toolpost flexure were found. With that geometry, the toolpost deflection with a 2MPa supply is calculated to be 200 μm. Toolpost deflection is a linear function of pressure, and is predicted to be approximately 0.098 nm/Pa.

Under normal conditions, the diaphragm and flexure should operate well within

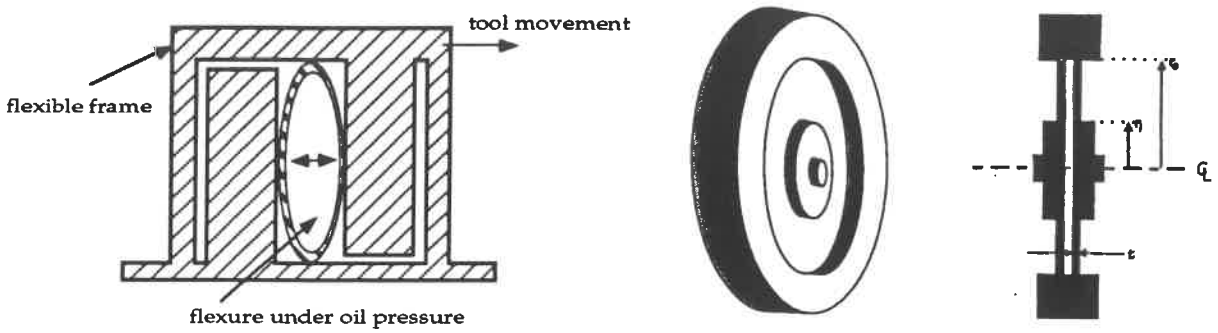

Figure 3: Toolpost Flexure and Diaphragm

their elastic range. Actual measurements of toolpost deflection versus fluid pressure show a total span of 180 μm for a 2MPa supply, and a linear displacement of 0.088 nm/Pa. [Tran 1993]

Case III: Hydrostatic Carriage way

As we have designed our slideways they have two functions: actuation and bearing. The bearing's function is to support the load, provide stiffness against disturbance forces, and to minimize friction particularly avoiding the coulomb friction and stick-slip behavior associated with sliding plain bearings. Rolling bearings also suffer from non-repeatability, especially with very small motions. While flexure based bearings are extremely repeatable, their range of motion is limited. Hydrostatic bearings are extremely smooth and there is no contact between moving parts. Hydrostatic bearings are well-damped and exhibit good stiffness, especially at high frequencies.

We have built hydraulic slideways, based on Kraakman's [1969] design. Kraakman's slideway design results in a very compact carriage supported by externally pressurized hydrostatic bearings (see Figure 4). These slideways have a total travel of approximately 130 mm and has a built-in means of correction for non-straightness and yaw motion. As shown in the cross sectional view, the design incorporates an opposed pad caliper bearing. Two pairs of pads are actuated. One pair acts at the front of the carriage and one at the rear. A lateral translation of the carriage can be achieved by actuating these together and a small rotation can be achieved by actuation in opposition. The total range of motion available is ±30 μm about the nominal centered position. This range is sufficient to deal with the expected non-straightness of the ways, which is on the order of ±5 μm. Differential flapper valves are used to control the fluid flow to the bearings. As assembled, the measured lateral stiffness was approximately 36 MN/m without feedback. [Peirce et al. 1992]

The long-stroke motion of the carriage is handled by hydraulic piston actuators. As with all of the hydraulic actuation in our system, the pistons and the slideways make use of the temperature controlled oil and are without seals. [Wiedemann 1993]

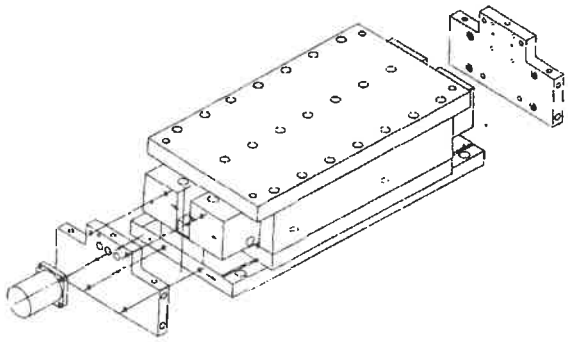

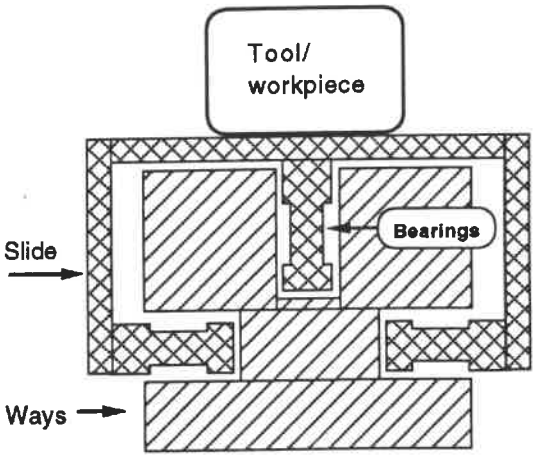

Figure 4: Kraakman Slideway Design

Case IV: Straightness and Yaw Correction

Since no slideway is perfectly straight, there must be provision for measuring error motion, and for correcting error motion. We have incorporated in the way design an integral means for correcting straightness and yaw. We are also developing and building a novel hydraulic sensor for measuring non-straightness and yaw called a "differential oil gauge" (see Figure 5). Initial evaluations of the differential oil gauge straightedge show promise. This technology has the potential of being both more robust and less expensive than using LVDT's as straightedge sensors.

A differential oil gage can be thought of as a pair of opposed externally pressurized bearings. There is an external resistance between the supply and the pocket and a variable resistance to flow between the lands and the surface of the straightedge. The resistance is a function of the gap, h, between the lands and the surface of the straightedge. By measuring the differential pressure between the two pockets over a small range of motion, one can arrive at a linearized relationship with the deviation of the head from the nominal centered position. A differential oil gauge measurement has no probe contact: There is neither lift off nor surface contamination. Furthermore, since the oil gauge measurement averages over the straightedge surface, sensitivity to errors with short correlation distance is reduced.

This sensor as described is not without its drawbacks. While the sensor uses the same technology as an externally pressurized bearing, its function and requirements are much different. The oil gage should have low stiffness and force levels in order to minimize the disturbances to the rest of the system. With the geometry of our initial design, we expect a sensitivity of 0.02 psi/μin. (5 GPa/m). However, the disturbance forces exerted by the metrology will be on the order of two times larger than the cutting forces in diamond turning.

We are taking two approaches to solve this problem. The first is to extend the Donaldson [1972] reversal methods in the presence of forces with the current design. The second approach is a redesign of the oil gage sensor to minimize the net disturbance force.

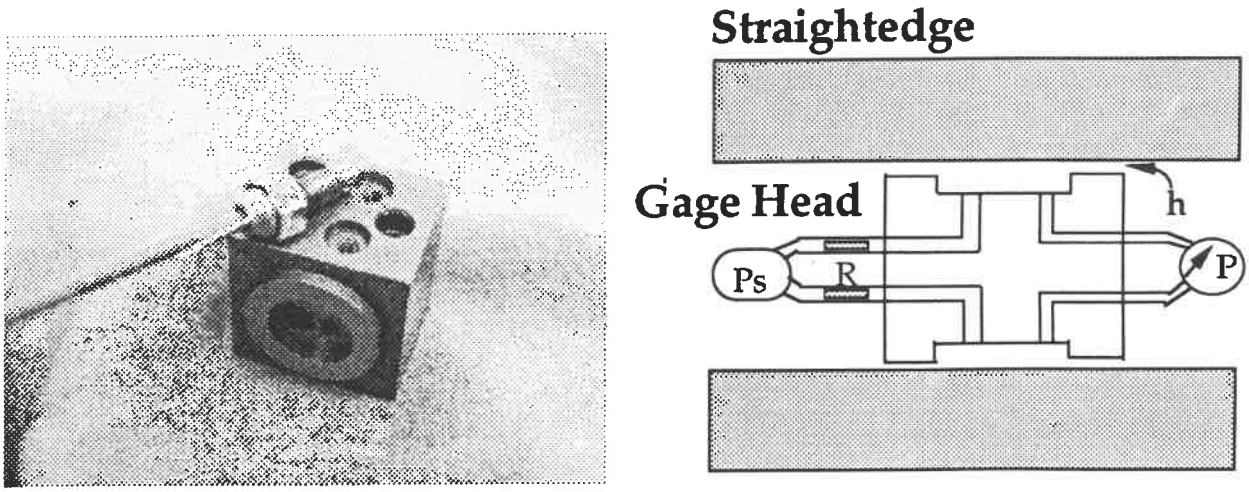

Figure 5: Oil Gage Design

Results:

We have developed a family of laminar-flow based hydraulic actuators for ultraprecision applications. Using these hydraulic components on our testbed, we machined a flat (spindle speed 1000 rpm, feed rate 1.5 μm/rev, tool radius 1mm) and an inclined flat. Spindle position, toolpost position, and cross slide position were measured, though only the toolpost actuator was under closed loop control. The surface finish of the finished parts have R_a of 25nm and R_z of 250 nm. [Tran 1993]

Acknowledgements:

Rafi Atzman for suggesting the differential oil gage; ONR, NSF for support

References:

Bryan, J., *International Status of Thermal Error Research.* Keynote Paper, Annals of the CIRP Vol. 39/2/1990.

Chen, C.J., *A Laminar Flow Motor-Driven Machine Tool Spindle..* Ph.D. Thesis, Stanford University, 1985.

DeBra, D.B., Victor, R.C., and Bryan, J., *Shower and high pressure oil temperature control.* In CIRP Annals Vol. 35/1, 1986.

Donaldson,R., *A Simple Method for Separating Spindle Error from Test Ball Roundness Error.* In CIRP Annals Vol. 21, 1972.

Kraakman,H.J.J. and deGast,J.G.C, *A Precision Lathe with hydrostatic bearings and drive..* Phillips Technical Review 30(5), 1969.

Peirce,S., Kahn,R, and Rischer D., *Design of an Oil Gage.* ME119 Class Project, Stanford University, 1992.

Tran, H.D., *Feedforward Control for Non-Circular Cutting on a Diamond Turning Lathe..* Ph.D. Thesis, Stanford University, 1993.

Wiedemann, M., *Examination of a Hydraulic Feed Drive for a Diamond Turning Machine..* Directed Study Report, Stanford University, 1993.

Open Architecture Controls for Precision Machine Tools

Bradley N. Damazo

Charles W. Yang

Robert J. Gavin

National Institute of Standards and Technology
Gaithersburg, Maryland

Dennis Smith
Delta Tau Data System
Northridge, California

Introduction

The National Institute of Standards and Technology has initiated the Enhanced Machine Controller (EMC) program to study open architecture controls for machine tools[1]. The EMC Shop Floor Controller (SFC), a testbed consisting of a vertical machining center and a PC-based controller, was established to study and validate open architecture concepts. The preliminary results of the study were transferred to an ultra precision machine.

This paper not only discusses open architecture machine tool controls but how they were applied to an ultra precision machine used for diamond turning and grinding. Also, the benefits of an open architecture machine tool controller to the machine tool industry with applications to the precision engineering community is discussed.

Background

"Open architecture machine tool controls" has become a frequently used term in industry with many meanings. We define the open architecture concept as: a controller that maintains full functionality while allowing all hardware and software components to be obtained from a number of sources. A good example of such a system is the IBM PC[2].

---

[1]Since the mid eighties, the U.S. government and industry have been pursuing open architecture controls. Ongoing programs such as the Next Generation Controller sponsored by the Air Force, the Low End Controller sponsored by the National Center for Manufacturing Sciences have produce specifications for open architecture controls. In addition, European Community is currently sponsoring a program regarding open architecture machine tool controls.

[2]Commercial equipment or materials are identified in this report in order to

When IBM disclosed the PC's architecture in the early eighties, it gave birth to a new industry of third-party hardware and software vendors who developed applications to run on the PC. Similar market dynamics may help the machine tool industry. Motion control boards are currently available which, when combined with PC hardware and software, can be made into machine tool controllers.

From a technological perspective, NIST has great interest in open architecture machine tool controls. NIST has conducted research in sensor-based machine enhancements, such as thermal and geometric error compensation, for over two decades. Closed architecture and proprietary systems have made difficult the implementation of enhancements. Open architecture will better enable NIST, as well as academia and industry, to easily integrate enhancements.

Technical Approach

The SFC utilizes off-the-shelf components such as motion control boards and hosts them on the PC platform. The motion control card performs all time-critical functions such as servo control, path-planning, and programmable logic controller. The host PC performs less time-critical functions such as the operator interface and factory integration. This division of labor eliminates the need for a real-time host operating system, allowing a generic PC to host machine control software. Further controller functionality can be obtain by adding sensor interface boards to the PC backplane. This approach may reduce OEM development and component costs.

Applying this concept, the first version of the SFC was developed with a generic PC and a PMAC motion control card from Delta Tau Data Systems. The SFC was integrated with a Monarch VMC75 vertical milling machine to establish a testbed. As a demonstration of flexibility, operator interfaces were developed that emulate three popular controllers: Fanuc 10, General Electric GE2000, and Allen Bradley 8200. This approach would allow the operators to run the machine tool with the most familiar interface. The host computer was also linked to a local area network using a generic, low-cost network card.

The second version of the SFC was developed for the Microsoft Windows 3.1 environment, in collaboration with Delta Tau Data Systems, taking advantage of Windows 3.1 infrastructure to improve user-friendliness, ease of application integration, and openness of the SFC. A video system was installed to run along with the SFC to provide on-screen,

---

adequately specify certain experimental procedures. In no case does such identification imply recommendation or endorsement by the National Institute of Standards and Technology, nor does it imply that the material or equipment identified is necessarily the best available for the purpose.

real-time image of the machine tool work volume. In addition, a CAM package was installed on the SFC host PC to provide local design capabilities, and a multi-media shop management package was installed to provide productivity enhancements. These applications can all be executed concurrently, along with the SFC. It is important to note that all these applications are off-the-shelf and installed directly onto the host PC, without customizations.

Software Architecture

Figure 1 illustrates the software architecture for the SFC. The motion control card performs all time-critical functions, while the host PC performs less time-critical, higher-level functions. All routines required to communicate with the motion control card are stored within a dynamic link library (DLL). These routines are exported to applications, for example the operator interface, to communicate commands and status with the motion control card. It is possible for multiple applications to access routines in the DLL and thus communicate with the motion control card. This DLL enables third-party applications to have access to the means of controlling the motion. Furthermore, the DLL can be developed to deal with the communication and control protocol of specific motion control cards, yet still maintain a uniform application programming interface (API). Controllers can be developed to work with any number of motion control boards.

Other applications may simply run along side the SFC, as separate tasks with no interaction, such as the video system mentioned above. Future versions of SFC will incorporate dynamic data exchange (DDE), which is a protocol for data sharing, to communicate with other Windows 3.1 applications.

Windows 3.1 Graphic User Interface (GUI)

An immediate benefit of the Windows 3.1-hosted SFC is the enhanced user-friendliness of the graphical user interface (GUI). The look and feel of the operator interface is now much more intuitive than the DOS-hosted, character-based version. The use of the mouse, command buttons, pull-down menus, dialog and combo boxes is straightforward and is consistent with other Windows 3.1 applications. The new interface is expected to reduce operator training.

Third Party Application Development

Third party applications that interact with the SFC can be readily developed using the multitude of tools available for Windows 3.1. This process is facilitated by any number of available visual-based language compilers/interpreters that significantly reduce the development time for

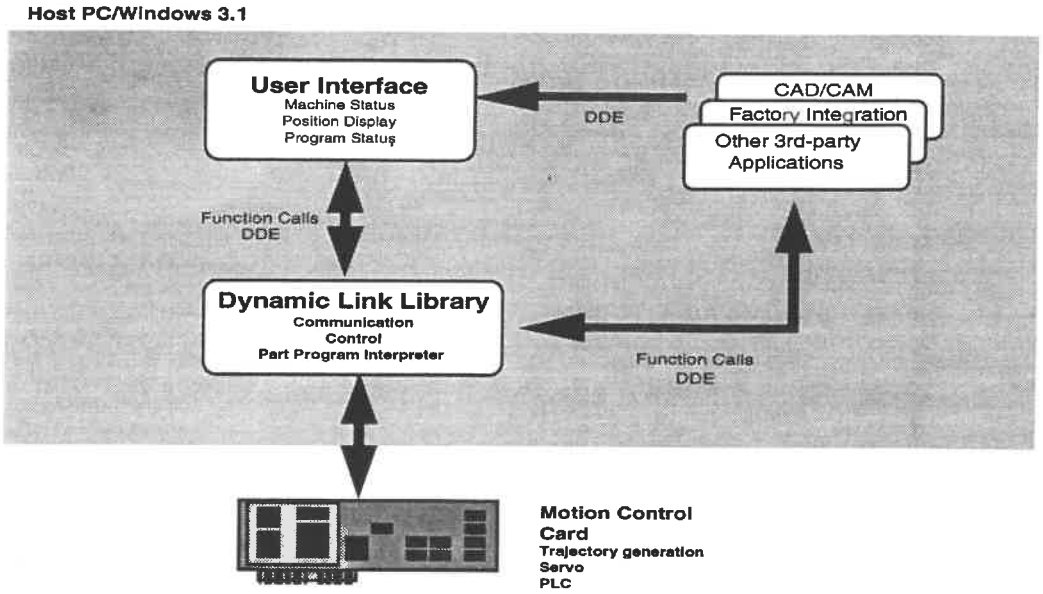

Figure 1. SFC Software Architecture

GUI applications. Work is in process to establish a common set of library routines that may be exported to other applications.

Links that facilitate data sharing among applications can be established using Dynamic Data Exchange (DDE). DDE enables "cutting and pasting" of information between applications such as spreadsheets and word processors. This very mechanism can be applied to third-party applications and the SFC. For instance, SFC may be configured to "paste" information, such as part count and elapsed time, across a network to a production monitoring program above the shop floor.

Because Windows 3.1 provides non-preemptive multi-tasking, applications can be developed as independent processes. Applications that process sensor input can run along with SFC and use DDE to send information to the SFC to alter the machining process. However, these applications may be restricted because process execution within Windows 3.1 is non-deterministic. Applications with stringent timing demands are not appropriate for this environment. For example, the real time servo update function, in the SFC, is handled by an independent processor, the PMAC. Additional real time functions can be handled by independent processor boards placed in the PC backplane (the Windows NT operating system is designed for multiprocessor computing). Even so, a broad set of sensor-based applications will be suitable for Windows 3.1. For instance, thermal-geometric error compensation should be suitable, since temperature and geometric errors within the machine tool are relatively slow to change.

Benefits to Industry

The major benefits of an open architecture machine tool controller to industry are cost savings, improved quality and productivity, and the ease with which advances in technology can be integrated into the controller. Examples of these benefits are listed below:

Cost savings by using the well understood PC platform. The machine tool industry can take advantage of the existing service and knowledge base in the PC industry for maintenance and hardware and software development. Furthermore, the machine tool industry is able to use the price competitiveness of the PC industry to save costs.

Improved quality through utilizing sensors to affect the machining process, e.g., on machine inspection. The integration of sensors and process models into a machine tool controller has been severely restricted with existing technologies, and would not be so with an open architecture.

Improved productivity by using third party software productivity tools integrated with the controller, e.g., computer aided manufacturing and multi-media shop management packages.

Integrating advances in technology onto the factory floor does not require retraining operators. The life of a machine tool controller is a fraction of the life that machine's structure. When controller obsolescence occurs, retrofitting with an open architecture controller takes advantage of recent advances in machining technology without incurring costs of additional operator training and rewriting part programs. This is accomplished by emulating the existing operator interface and part program dialects - protecting one's investment.

Application to Ultra Precision Machining

The SFC has been installed on a ultra precision machine as shown in Figure 2. This machine is a two axis T-based design that uses hydrostatic slideways. The slideways are typically straight to 0.1μm over 300 mm of travel and have typically 350 N/μm stiffness. Each slideway uses a 10 nm linear metal scale for position feedback. The slideways are mounted on a granite machine base weighing 6.25 tons. The machine is enclosed in a computer controlled thermal enclosure regulated to ±0.2°C.

This machine serves as a research testbed. Therefore, the ability to reconfigure the machine for fly cutting, single point diamond turning, hard turning and grinding is important. The open layout of the machine allows different spindles to be used and positioned for the particular machining process. With the SFC, different spindles can be easily integrated into the controller, allowing quick spindle reconfigurations.

At present, several concepts are being planned that take advantage of the open architecture control. The first is the use of a force stage for grinding wheel force touch off and process monitoring. The second is to use displacement sensors mounted behind the machine's hydrostatic spindle face plate to measure axial displacement due to spindle growth. A second set of displacement sensors measures the radial displacement because the axis of rotation of a hydrostatic spindle is a function of speed and load. These displacement measurements could be fed back through the control to servo the slideways for a constant grinding wheel force on the part.

An additional concept that could be readily implemented with an open architecture control to improve processes uses a ultrasonic sensor to detect if a grinding wheel needs to be dressed. Also, analog probes can be used for tool setting or inspection.

Conclusions

The EMC project at NIST is focused on establishing technology to develop open architecture machine tool controllers based on widely accepted, third-party commercial platforms and components. The SFC, a PC-based example of the EMC concept, is hosted on the Windows 3.1 environment. The implementation takes advantage of Window's powerful features to facilitate future integration of a variety of third-party applications, ranging from custom user interfaces, production monitoring and control, to sensor-based machining.

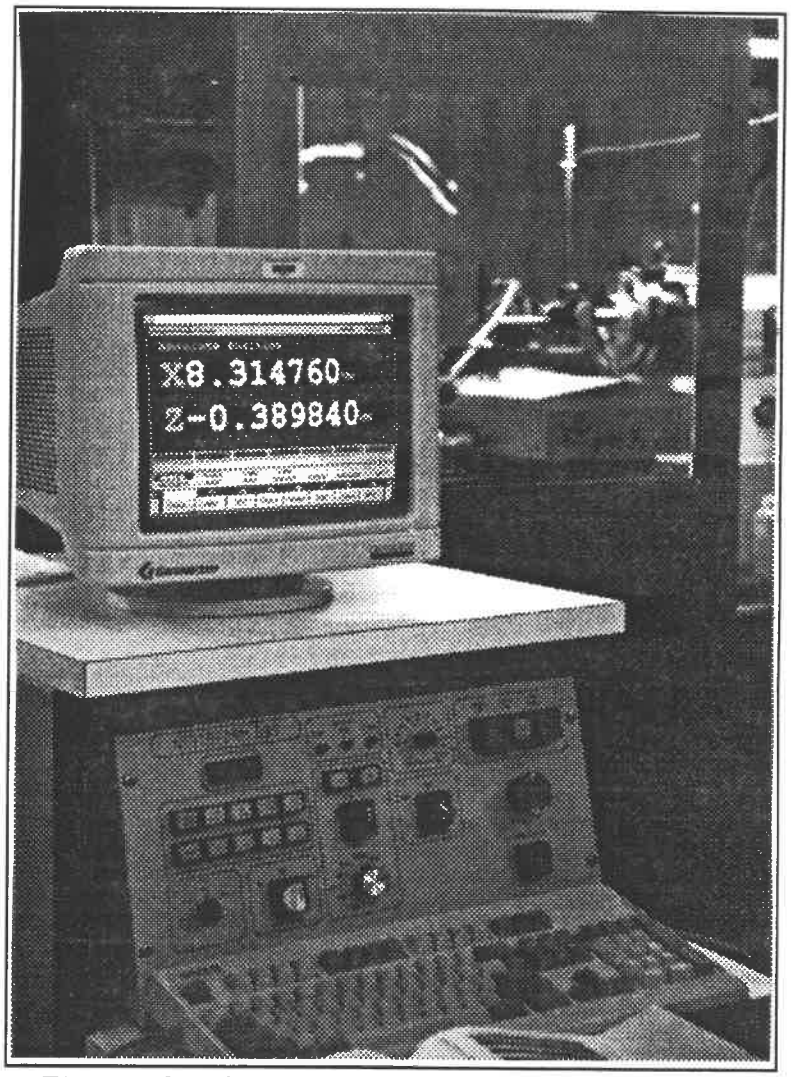

Figure 2, The EMC SFC installed on a ultra precision machine tool.

Open Architecture Controllers - a Development Platform for Machine Tool Control Applications

P. Orban *, I. Yellowley **, Y. Zhou *
* Institute for Advanced Manufacturing Technology,
National Research Council of Canada,
Ottawa, ON. Canada, K1A 0R6
E-mail: ORBAN@NRCAMT.IME.NRC.CA
** Department of Mechanical Engineering,
University of British Columbia,
Vancouver, BC. Canada, V6T 1W4

Synopsis

Open Architecture Controllers (OAC) have recently emerged as a viable alternative to commercially available NC controllers. The diverse requirements in manufacturing environments and the flexibility offered by OACs provide a control platform with great potential for various applications. Projects are under way both at NRC and UBC laboratories to attempt to realize the benefits and opportunities provided by an OAC.

This paper describes the control architecture being used, details the efforts required to integrate the OAC to different machine tools, and explores the possibilities presented by machining systems equipped with such controllers.

Introduction

NC controllers have come a long way since their original introduction in the early fifties. Controllers have gone through many stages as they progressed from the early, specially designed hardware to today's CNCs based on embedded multiple microprocessors, with most functions implemented in software. The basic features of NC controllers have not changed much, and they are still considered by users as "black boxes" where input/output and functionality are well defined, but the internal details are not accessible. This paradigm served the industry well until the 1980's, however the use of computers in manufacturing processes has proliferated since then, and demands for improved cutting process performance has increased, the limitations of a closed NC system are now quite obvious. One solution to the problem is closer cooperation between the end-user and the controller builder, the customization of the NC can then be done by the builder to the user's specification. However, cost considerations have limited the usefulness of this approach. An alternative to a custom-made commercial controller is an open architecture control (OAC) system, which is a well specified, modular, open system, the core of the system providing the basic functionalities, with enough information for qualified users and machine builders to do the required customization [Ashley-90], [Barnes-91].

Open Architecture Machine Tool Control Systems

As mentioned above, a system is considered open if its design and modules are well documented, and it can be reused, modified, and explored by anyone. That openness should refer to both hardware and software. In order to achieve the most benefits, all hardware and software modules should be available on the open market.

In order to understand what basic modules are needed for a machine tool controller, the architecture of NC controllers has to be understood first. Figure 1 shows the block diagram of a CNC. The modules represent the main functions that any CNC should have, or in other words, what should constitute the core of any open machine controller system.

The basic function of any NC is the

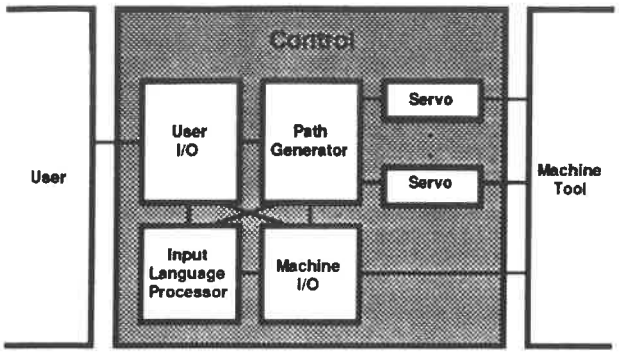

Figure 1

control of axes. The trajectory generation is done by the **Path Generator** module. Historically NCs provide linear interpolation in any direction and circular segment generation in the main planes. The output from the **Path Generator** is taken by the **Servo** modules, which control the individual axes of the machine tool. The servo amplifiers are usually not part of the controller, but in the newer controllers there is a tendency to integrate the control of high efficiency AC drives into the axis control module. Beside the axis control lines the machine tool has to be connected to the controller by a number of discrete I/O lines to receive and send miscellaneous information. This function is implemented by the **Machine I/O** module. Commands for the CNC originate from the user, either a human, or a higher level control system. The **User I/O** module provides the connection for this control, while the **Input Language Processor** module interprets the commands, translates and distributes them to the modules of the CNC. Coordination between the modules is provided by the **Control** function, which is not a separate module, rather a distributed functionality which all the modules contain.

An open architecture implementation of a CNC maps the above architecture into hardware and software modules. To date only hardware modules are available in a wide enough selection commercially, while some of the software modules still have to be custom made.

Hardware components include the bus system, processor boards, axis control boards, and various input/output boards for the machine tool and for the user. Popular bus systems used for OACs are the STD, VME, and different PC buses. The main criteria for selection is the performance, price, and availability of boards for the bus system.

The choice of software tools is limited to some extent by the hardware platform being used. Usually the dedicated hardware boards come with software (drivers) provided by the vendor. Axis control boards do have servo programs and utilities to tune and set-up the servo systems. Some vendors also provide simple path generator primitives. For the **Machine I/O** function PLC programs are available, implementing boolean functions and/or relay logic. The communication and display boards provided for the User I/O functions usually have drivers, implementing standard communication and graphics user interfaces.

To tie together the functionalities and to provide the **Control** function real-time kernels and/or appropriate operating systems are used.

The UBC OAC

A design effort was initiated at the Department of Mechanical Engineering, University of British Columbia in 1989, to study the issues related to open architecture control systems. The result of that effort is an OAC architecture [Yellowley-91], [Yellowley-94] that is successfully being used for the control of turning centres, machining centres and for robot control in several configurations.

The UBC OAC is a distributed system based on the STD/ST bus. The main components are the axis control modules, the PLC module, and the supervisory module. The architecture of the controller has been designed to minimize intertask communication. The central task of interpolation is generally the key to determining the requirements of the central processor, (particularly in those cases such as machine tools, where radius and length compensation is required). The approach taken is a two stage interpolation strategy, where the central processor is required to generate motion increments for all axes at a relatively low rate; these increments are then splined at a relatively high rate by each axis slave microcontroller leading to acceptable contouring performance with relatively low computational load at the master. This solution considerably reduces the need for high bandwidth in the communication between the central and processor and axis slaves. The first stage and second stage

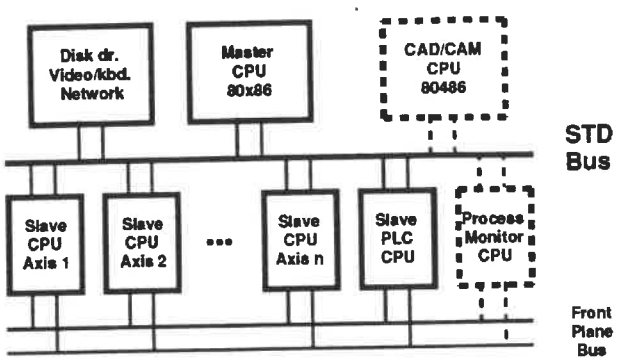

Figure 2

interpolation frequencies can be adjusted by the user hence, in reality, the system may be constrained to act as a one stage system. Most often however the first stage interpolation frequency is set between 100Hz and 250Hz, while the second stage frequency is set in the range between 1KHz and 4KHz.

The servo functions are realized on single board controllers. The boards read the positional input from the axis encoders and output the analogue signal for the servo amplifiers. The compensating lead-lag filter is implemented digitally. The boards also do the low level interpolation. The axis control module program is written in the native assembly language of the processor. The number of axes controlled can be expanded very simply, just by adding additional modules. The axes are synchronized to each other by a high-speed front-plane bus.

The PLC or machine I/O module is implemented on another single board controller. This module is also tightly coupled to the axis controllers through the front-plane bus. The processor interfaces to industry standard I/O modules to handle the discrete signals. Beyond the logic processing the module also provides for direct spindle control. The PLC program was written in the Forth language.

The rest of the CNC functions are provided by the supervisory module. That module is running on an Intel 80x86 based system, consisting of several boards on the STD bus, and behaving like a PC clone computer, running a special version of the DOS operating system. The PC implementation on the STD32 bus system allows for the insertion of multiple CPU boards to realize a multiprocessor DOS system. The BIOS of the processors are extended to share common computing resources like disks, keyboard, e.t.c. and to provide for interprocess communication through shared memory. The CNC program resides on a single DOS processor and was written in the Forth language. The Forth language was chosen as it is a "high level" language, provides fast execution, and good access to low level hardware operations. The version of Forth used for the CNC implementation also has simple multitasking services on a DOS processor.

Applications of the OAC

The UBC OAC has been applied successfully to control a number of machine tool configurations.

The current version of the OAC is being used to aid research in three applications at UBC, in each cases the front plane communication ability is used to perform process identification, modification and optimization.

The majority of the early research at UBC was carried out using a 3 axis CNC lathe. The current control on this machine uses the STD32 bus, has two master processors, and includes a Motorola 56001 DSP which is accessible over the STD32 bus and front plane communication system. The DSP is used for process control; in particular it senses 3 force components at speeds ranging from 1 to 10KHz, this data is then used to identify cutting conditions, examine constraints and drive the state lines accordingly thus varying feed. The system has been demonstrated to perform well even during rather sharp transients [Ardenaki-92]. Most recent work on this system has focused on the integration of CAD/CAM and CAPP technologies within the unit. The basic system used within the unit is based upon AutoCad and NCPolaris, both of which run on a 486 CPU while the machine control activities are accommodated by a V53 based master.

A more recent application has been the building of a quasi-commercial unit with funding from the Science Council of British Columbia. This unit controls a 3-axis milling machine with an operator interface which is comparable in complexity to industrial units,

thus allowing significant challenge and testing of the PLC functions. The machine is designed with low friction ways and high bandwidth servo systems to allow the use of the servo system itself for process monitoring (milling and holemaking processes).

The Manufacturing Engineering Laboratory at UBC has also conducted a recent research exercise which demonstrates the use of control architecture in the minimization of path error in high speed profiling [Seethaler-93]. This work has been conducted using a 5-axis robot system as a test bed. Efforts will continue to allow the fully integrated control of this system.

At the National Research Council the UBC OAC is used to control a machining centre in a flexible manufacturing cell. The manufacturing cell was originally designed and implemented to explore various issues in unattended, flexible, high precision manufacturing [Johnston-87]. The controller of the machine tool was an obsolete GE 1050 CNC. In order to control the operation of the CNC from a higher level cell control computer a special coupler needed to be developed to allow for the unattended operation of the cell [Orban-86]. One of the reasons to move to the new open architecture configuration was to overcome the limitations imposed by the closed nature of the GE 1050 CNC. Adaptation of the UBC OAC to the machining centre was quite simple: only the number of axis control modules needed to be expanded and the PLC program modified to the machine tool. Though only the controller was replaced on the machine tool, the longest effort was required by the wiring of the controller.

At NRC we plan to implement an advanced surface machining capability in the OAC [Orban-92], and intend to realize real-time collision detection for the NC programs [Greenspan-93].

Advantages of OACs

Open architecture controllers offer a number of benefits to the users and developers of the technology. The solution provides flexibility, as customization, expansion can be accomplished with ease. Building applications, accommodating special needs should require little effort. New product development cycle times should decrease as specification, system design and implementation becomes simpler. The technology in controllers should improve more rapidly, as there is less effort required to apply general computer technology to controllers.

OACs are particularly well suited to niche applications. Manufacturing processes, which are aided only by computerized positioning tables and very simple controls at the present time, are the most likely initial candidates for OAC technology. Processes like laser machining, flame, plasma and waterjet cutting, electron beam welding, e.t.c. come to mind.

Technologies implemented with the aid of OACs should provide for better integration. This should apply both at the process level, like handling of real-time sensors for adaptive control, and at the production level, sharing information with higher level control for integrated manufacturing. Information can be extracted, and provided for at the most appropriate level.

Using open architecture controllers should result in a cost effective solution. This applies both to the component costs, and to the development costs as well. Having a choice of suppliers using non proprietary technologies, as opposed to employing single source (as the case with using OEM CNCs) should provide the users with considerably increased flexibility. It is likely that in the future the market for controllers will be considerably different to the situation which exists today.

Conclusion

Open architecture numerical controllers are an emerging technology in the manufacturing field. They provide advanced solutions for a wide variety of control problems where previously only the high cost, non-optimal, custom engineered alternative existed.

The application of the UBC OAC proved that an open system with a well documented, extensible set of core functionalities, can provide a cost effective solution with very little effort required, and could serve as a test bed for new ideas. Open architecture platforms will give the designers and builders of specialty hardware, software sensors and auxiliary systems a low risk R&D capability and implementation platform.

References

Ardenaki-92 R. Ardenaki, "The Integration of Process Control and Optimization within a Multi-Processor Based Motion Control System." M.A.Sc. Thesis, University of British Columbia, 1992.

Ashley-90 S. Ashley, "A Mosaic for Machine Tools." Mechanical Engineering, September, 1990, pp. 38-43.

Barnes-91 J. Barnes, "Breaking into the Black Box." Canadian Machinery and Metalworking, February, 1991, pp. 23-26.

Greenspan-93 M. Greenspan, D. Johnston, "Collision Avoidance - A Component for Automated Manufacturing", Proceedings of the MAPLE-93 Symposium on Manufacturing Application Languages, Ottawa, Oct. 4-5, 1993, pp. 127-133.

Johnston-87 D. Johnston, "Small Batch Precision Manufacturing Using a Prototype Automated Cell", Second International Conference on Computer-Aided Production Engineering, Edinburgh, April 1987, pp. 223-228.

Orban-86 P. Orban, "Talking to Machine Tools - DNC Coupler Design", Proceedings of the Eighth Symposium on Engineering Applications of Mechanics, University of Sherbrooke, Sherbrooke, Quebec, June 8-10, 1986. pp. 130-135.

Orban-92 P. Orban, "Advanced Path Generator for Sculptured Surface Machining", Proceedings of the IFAC Workshop on Motion Control for Intelligent Automation, Peruga, Italy, October 27-29, 1992. NRC 33579.

Seethaler-93 R.J. Seethaler, "A New Contouring Algorithm for the UBC Controller." M.A.Sc. Thesis, University of British Columbia, 1993.

Yellowley-91 I. Yellowley, P.R. Pottier, "The Development of an Integrated Open Architecture Machine Controller", in the Proceedings of the First Atlantic Congress and Exhibition on Advanced Manufacturing and Engineering, 1991, pp. 75-85.

Yellowley-94 I. Yellowley, P.R. Pottier, "The Integration of Process and Geometry within an Open Architecture Machine Tool Controller", Int. J. Mach. Tools Manufact., Vol. 34, No. 2, 1994, pp. 277-293.

$$E = R - R' = R\,[1 - \cos(\theta/2)] \tag{3}$$

Since the arc distance for a segment, R times θ, is also the vector velocity V multiplied by the segment time T_a, and using the Taylor series approximation $\cos x = 1 - x^2/2! + x^4/4! + \ldots$, we can approximate the error as

$$E = R\,[1 - \cos(VT_a/2R)] \cong V^2\,T_a^2 / 8\,R \cong R\,\theta^2 / 8 \tag{4}$$

However, this method requests step changes in velocity at block boundaries, which are not physically realizable, so substantial servo lag is required, which produces significant errors of its own. For a system with servo lag due to uncompensated mechanical time constant T_m, this error can be approximated as

$$E \cong V^2\,T_m^2 / 2\,R \tag{5}$$

With second-order position update polynomials, it is possible to introduce acceleration control, which largely eliminates the need to maintain servo lag (modern servo techniques make it *possible* to eliminate this lag, but the interpolation techniques must *permit* it). Now the velocity impulse reconstruction appears as a triangle, not a rectangle; the velocity rectangle of the first-order technique is convolved with a unit acceleration rectangle, resulting in the triangle. Because the axis velocites are no longer constant in the general case, the path segments are no longer straight. Instead of chords, we get curves joining the midpoints of the chords that are approximately parallel to the ideal curve. Now the error as the reconstructed curve passes the sample points with approximately the same error as at the midpoints shown in Equation 4.

This technique requests step changes in acceleration, and hence, step changes in motor current, which are not possible due to motor inductance. With third-order interpolation, acceleration can be kept continuous as well. The velocity impulse reconstruction now looks roughly bell-shaped, the result of convolving the triangular response with a unit rectangular "jerk" (da/dt) response, and a cubic spline is produced. This spline passes through "via points" VP_n on each axis

$$VP_n = (P_{n-1} + 4\,P_n + P_{n+1}) / 6 \tag{6}$$

On a curve of local radius R and subtended angle θ, the effective radius is

$$R' = [R\cos(-\theta) + 4\,R + R\cos(\theta)] / 6 = R\,(2 + \cos\theta) / 3 \tag{7}$$

producing an error of

$$E = R\,(1 - \cos\theta) / 3 \cong V^2\,T_a^2 / 6\,R \cong R\,\theta^2 / 6 \tag{8}$$

The error at the midpoints is the same to second order approximation. That this error is slightly larger than the second-order reconstruction is the "cost" of the added smoothness. The process of increasing the polynomial order and creating "smoother" impulse reconstructions by more convolutions can be continued indefinitely; in the limiting case a Gaussian impulse reconstruction is generated, and the error produced is

$$E = V^2 T_a^2 / 2\,R \cong R\,\theta^2 / 2 \tag{9}$$

CORRECTED POLYNOMIAL TECHNIQUES

All of the above techniques produce predictable errors to the inside of the curve. Since they are predictable, good pre-compensation algorithms are possible. This paper presents simple techniques that are very effective at reducing error by modifying the axis sample points P_n for each axis that are on the ideal curve to points P'_n that are outside this curve.

For the first-order chordal approximation the compensation that cuts the maximum interpolation error in half by producing equal inside and outside errors is

$$P'_n = (-P_{n-1} + 18\,P_n - P_{n+1}) / 16 \tag{10}$$

Different precompensation equations can be used if it is also desired to compensate for the servo lag error shown in Equation 5; the exact equation will depend on the ratio between T_a and T_m.

In the controlled-acceleration interpolation algorithm, the interpolation error can be dramatically reduced, eliminating the second-order error term, by the precompensation

$$P'_n = (-P_{n-1} + 10\,P_n - P_{n+1}) / 8 \tag{11}$$

The maximum resulting error is

$$E \cong V^4\,T_a^4 / 64\,R^3 \cong R\,\theta^4 / 64 \tag{12}$$

For the cubic-spline reconstruction, the precompensation that eliminates the second-order error term is

$$P'_n = (-P_{n-1} + 8\,P_n - P_{n+1}) / 6 \tag{13}$$

The maximum resulting error in this case is

$$E \cong V^4\,T_a^4 / 36\,R^3 \cong R\,\theta^4 / 36 \tag{14}$$

A DIFFERENT APPROACH

A relatively new approach that is gaining in popularity samples not only axis positions at each block boundary, but axis velocities as well. The reconstruction algorithm takes the beginning and ending positions and velocities, and the block time, and computes the unique cubic position equation coefficients for the segment that meet these constraints (the ending position and velocity are used to compute the beginning acceleration and constant jerk for the segment).

In this approach, the commanded trajectory passes exactly through the sampled points with continuous velocity, although not necessarily with continuous acceleration. The worst error is at the segment midpoints; this error can be approximated as

$$E \cong V^4\,T_a^4 / 384\,R^3 \cong R\,\theta^4 / 384 \tag{15}$$

This error is almost an order of magnitude smaller than the errors in any of the other techniques, but note that because it requests step changes in acceleration, and hence motor currents, the resulting errors in actual position may be larger than the pre-compensated cubic spline.

SUMMARY

The following table summarizes the errors for each of the techniques shown above. The formulas for via point errors and variations in errors between via points and segment midpoints are given, as are the worst case errors for sampling a subtended angle of 10^{o} on the curve.

Method	Via Point Error	Error Variation	10^{o} Segment Error
1st Order (Chordal)	0	$V^2 T_a^2 / 8 R$	$3.8 \times 10^{-3} R$
Corrected 1st Order	$-V^2 T_a^2 / 16 R$	$V^2 T_a^2 / 8 R$	$1.9 \times 10^{-3} R$
2nd Order	$V^2 T_a^2 / 8 R$	$V^4 T_a^4 / 144 R^3$	$3.8 \times 10^{-3} R$
Corrected 2nd Order	$V^4 T_a^4 / 64 R^3$	$V^4 T_a^4 / 144 R^3$	$1.4 \times 10^{-5} R$
3rd Order	$V^2 T_a^2 / 6 R$	$V^4 T_a^4 / 384 R^3$	$5.1 \times 10^{-3} R$
Corrected 3rd Order	$V^4 T_a^4 / 36 R^3$	$V^4 T_a^4 / 384 R^3$	$2.6 \times 10^{-5} R$
Position-Velocity	0	$V^4 T_a^4 / 384 R^3$	$2.4 \times 10^{-6} R$

CONCLUSIONS

Interpolation errors are a potentially important component of the error budget for a precision machine. The interpolation method and the point spacing must be considered carefully in view of the computational capabilities of the machine and the precision requirements. Modern techniques utilizing higher-order interpolation equations and pre-compensation methods permit intelligent trade-offs between required block rates and interpolation complexity. These techniques render the traditional method of evaluating the chordal error obsolete. The flexibility they bring allow much higher performance for a given computational capability, without sacrificing precision.

Contouring Interpolation Methods

Steps
(0th Order Update)

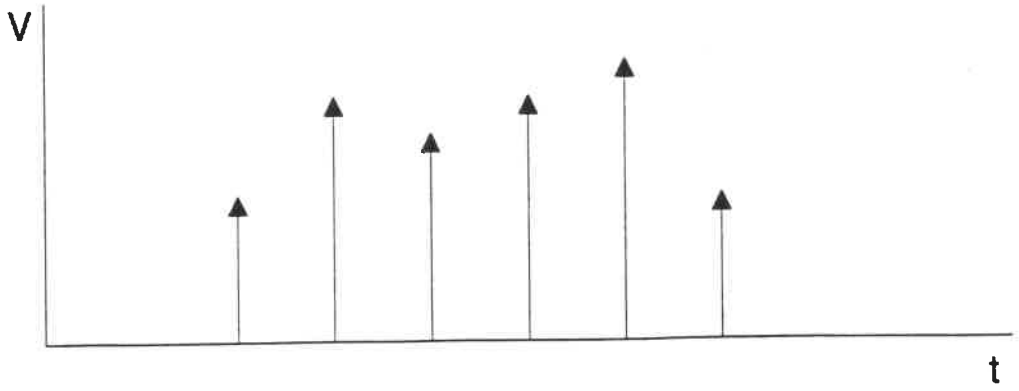

Constant Velocity
(1st Order Update)

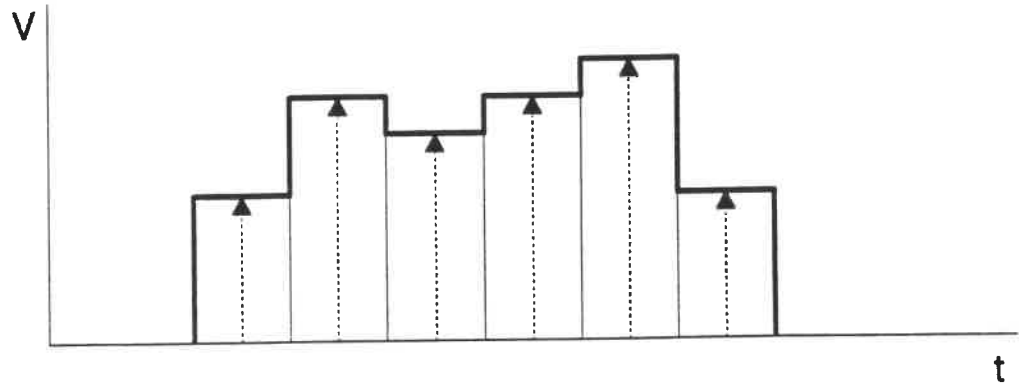

Constant Accel
(2nd Order Update)

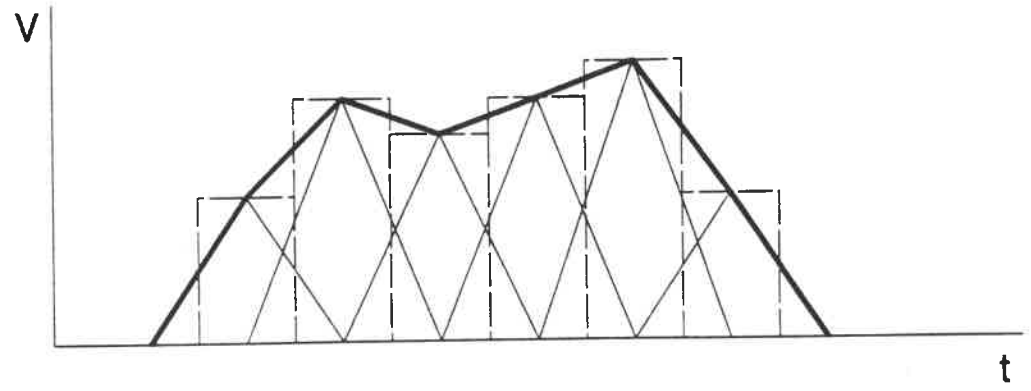

3-Point Spline
(3rd Order Update)

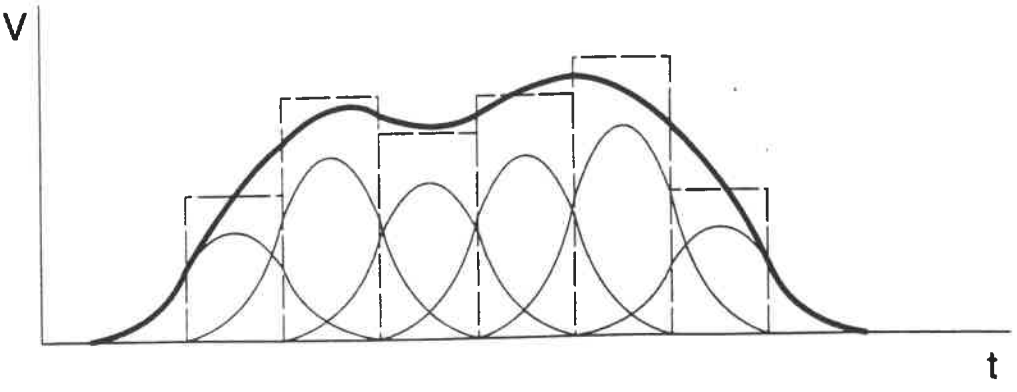

MASTER-SLAVE POSITIONING

Geert Wyntjes and David Mansur
OPTRA, Inc.
461 Boston Street
Topsfield, MA 01983

ABSTRACT

Many precision positioning systems operate in a scan-stop mode. Relatively high scan velocities between points, in order to maintain stepper throughput or productivity are desired, with precise positioning against outside disturbances at the stop position. Precise trajectory control is often not required as long as peak velocities do not exceed the Nyquist limit of the positioning transducer, a precision scale or laser interferometer. A two-tier or compound servo positioning system consisting of a high bandwidth, limited stroke actuator in the form of Piezo electric or magnetorestrictive transducer and a low bandwidth, long stroke positioner, perhaps a DC motor with a ballscrew or traction drive in a master-slave arrangement is then attractive. The input to the motor drive is derived from the error voltage that exists for the Piezo drive control loop. We will describe some designs, linear as well as X-Y that embody that approach and discuss some of the implications in terms of settling times, induced vibrations and heat generation.

INTRODUCTION

The availability of position transducers such as 2-frequency laser interferometer based systems and precision scale readers with resolutions at the nanometer level and electrical bandwidths and sampling or update rates well in excess of the tens of KHz range and with a large dynamic range (> 30 cm) makes it possible to close the loop around a positioning system, actuator and load with a fast response without its stability being affected by delays of the transducer. An attractive approach is then to design a two-tier servo positioning system where, a fast -the master- actuator provides positioning over a limited range, up to 10 micron or maybe 100 micron and a second positioning system, -the slave- for example consisting of a DC motor drive provides positioning over the full range of travel required. Its function is to maintain or keep positioning errors within the dynamic range of the fast transducer or if precise trajectory control is not required to keep the velocity within the Nyquist limit of the transducers so one

does not skip a fringe. Such an approach provides for a positioning system with a high bandwidth and therefore stiffness, attenuating outside disturbances. The positioning requirements for the coarse positioning, bandwidth or response time are greatly reduced and the effects of the hysteresis, stiction as well as the negative response observed between applied voltage and force by some researchers in Japan[1] should have little effect on the positioning precision.

Examples where such a master slave arrangement might be useful are:

Precision stepper control

Most steppers step from die to die without any concern about the velocity profile as long as it minimizes positioning time. A stable position at the print position is then important to minimize overlay errors.

Large travel, scanning Michelson interferometry spectrometers

There are situations where a step-scan for the interferometer is optimum. Examples include photo acoustic spectroscopy and time resolved spectroscopy. To optimize observation time it is important that one steps quickly from one interferogram point to the next. A two-tier drive is ideal for this. It provides for rapid repositioning with the time at each rest position used to bring the main mirror drive, e.g. an air bearing back into position.

Precision tool control

Rapid positioning could be provided by a tool mounted on a Piezo element and coarse positioning by the main feed drive.

Scanning Microscopy

It might make sense to have a large X,Y positioning table track the limited positioning capability of the Piezo-electric scanners typically used in these systems.

Precision length control for a laser tube, used in 2-frequency HeNe laser

While not directly related to positioning, but nevertheless germane, is the approach OPTRA uses to stabilize the beat frequency of its 2-frequency HeNe

---

[1] S. Futami, Nanometer Position Control and Nanometer Positioning Micro-Dynamics. Proc. of Nanotechnology Symposium, Aug 22, 1990.

lasers. It uses very fast magnetic field control for the first tier and for the second tier, temperature in the form of a heater to control tube length.

IMPLEMENTATION

An example of a two tier positioning system that could be used for a stepper is shown in Fig. 1. It shows a digital controller getting its inputs from some DSP based processor that generates positioning inputs in a format to optimize stepper through put. The error voltage that exists for the Piezo drive is constantly being minimized by controlling the coarse motor drive.

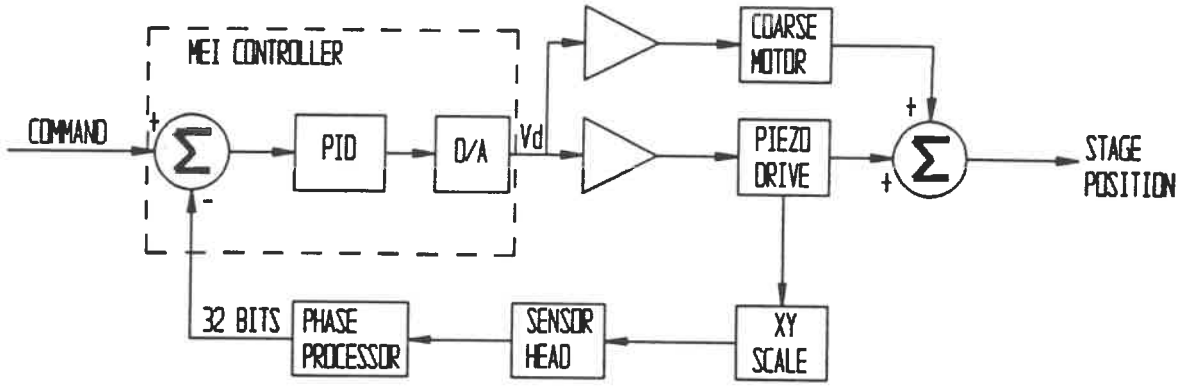

Figure 1. Two tier positioning loop, Piezo and DC motor. Error voltage V_d nulls the motor position.

Namometric Motion Control of a Traction Drive

Paul I. Ro, Assistant Professor
Ganesh Rao, Graduate Student
Quan Ma, Graduate Student

Precision Engineering Center
North Carolina State University
Raleigh, NC 27695-7918

ABSTRACT

Tracking performance, disturbance rejection, and robustness to parameter uncertainties of traction drives have been improved using two controllers. State feedback with a prediction observer was designed and implemented for good tracking of command input. This controller showed significant improvement over the conventional PID. Disturbance rejection has improved by both the state feedback and H-∞ schemes, individually. Robustness to output mass variation has improved significantly through a mixed sensitivity based H-∞ optimal control scheme. However, the H-∞ scheme was inherently more sensitive to sensor noise than PID.

1. INTRODUCTION

The increasingly stringent requirements of modern high precision machining are placing greater and greater demands on slide systems. Higher resolutions, larger bandwidths and better command tracking allow the production of more complicated parts with fewer errors. This requires a good understanding of slide dynamics and a well designed control system.

Traction or capstan drives are one of several systems used in precision machine tools. They are being investigated because they possess several desirable characteristics compared to the more popular ball screws. They exhibit very low friction and no backlash. Due to their low mechanical advantage and direct drive nature, however, they are more susceptible to noise and disturbances. Youden has published a comparison of the contouring performance of traction drives and lead screws [1].

This research focuses on understanding the characteristics of the traction drive and developing an accurate model of its behavior. With this knowledge, an effective state feedback/PID control scheme has been devised that improves upon the tracking performance and disturbance rejection obtained using PID control.

When using a conventional controller such as PID, a workpiece mass change will require a re-tuning of the controller gains to maintain the desired robustness. The advantage of an H_∞ controller is that it is insensitive to model perturbation and can reject uncertain noise or disturbance [3]. The aim of this work is to develop an H_∞ control system which provides robustness characteristics.

2. EXPERIMENTAL APPARATUS

The system consists of an Inland QT-3802 DC motor with a capstan roller attached to the shaft. A drive bar is preloaded onto the roller with 1780 Newtons of force. Both the bar and the roller are made of stainless steel. Aerostatic journal bearings support the roller and another air bearing maintains the preload on top of the bar. A Dover corp. linear air bearing slide is attached to the drive bar through a reed coupling. The calculated stiffness of the reed (K_r) is 767 MN/m in the drive direction. The position of the slide is measured with an ADE Microsense capacitance gage. A 25 MHz 486 PC with a Data Translation DT-2823 I/O board is used to control the traction drive and measure the slide position. To drive the motor, the output of the board is passed through a Kepco amplifier. A diagram of the assembly is given in Figure 1.

The system parameters are given in Table 1. The slide and motor parameters (slide mass, motor damping, resistance, inductance, torque constant and back emf constant) were obtained from the manufacturer's specifications. Using the traction drive assembly drawings, the mass of the bar, roller radius and roller inertia were calculated. The preload force is calculated from the bearing pressure (80 psi) and the area of the bar under the air bearing.

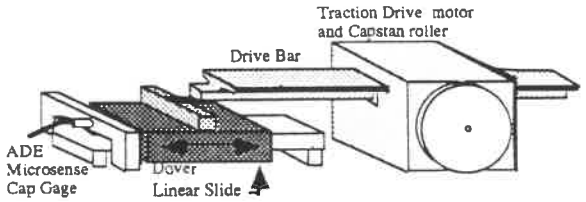

Figure 1: Diagram of the traction drive assembly

The reflected linear inertia of the rotary components of the drive is obtained by dividing J_m by the square of the

radius of the roller. This gives 10.8 kg for the traction drive. The same value calculated for a ball screw system with a pitch of $8.085 \cdot 10^{-4}$ m/rad gives 307.5 kg. This shows that the traction drive requires less energy to move than the ball-screw and that a change in the driven mass will have more effect on the traction drive.

M_s	Mass of slide	5.693 kg
M_b	Mass of drive bar	6.96 kg
J_m	Inertia of roller,shaft,motor and tach	$10.91 \cdot 10^{-3}$ kg m^2
r	Roller radius	$31.75 \cdot 10^{-3}$ m
B_m	Motor damping	0.168 N-m-sec/rad
K_T	Torque constant	0.8379 N-m/amp
K_b	Back emf constant	0.838 V-sec/rad
R_m	Motor resistance	4.36 Ω
L_m	Motor inductance	3.6 mH
F	Preload force	1780 N

Table 1: Traction drive parameter values

3. MODELING

To accurately model the system, a state-space servo model was developed. A diagram of the model is given in Figure 2. Here, v_a is the input voltage, v_b is the back emf, K_T is the motor torque constant and R_m and L_m are the motor resistance and inductance respectively. J_m is the inertia of the roller, tach and motor, M is the mass of the bar and slide, B is the viscous damping of the system, K_m is the stiffness of the torsional spring and K is the interface stiffness. The winding current is i_a, the angular displacement of the roller is θ and the linear displacement of the slide is x. The internal stiffness K_m can be attributed to the motor brushes which act like springs until the input torque overcomes the static friction and forces the roller to rotate. In order to obtain a linear model, however, the static friction has been ignored.

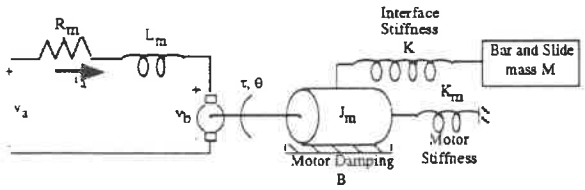

Figure 2: Servo model of the traction drive

A model of the system is developed in state space form in continuous time as follows:

$$\dot{X} = Ag\,X + Bg\,u \quad (1)$$
$$y = Cg\,X + Dg\,u, \quad (2)$$

where

$$Ag = \begin{bmatrix} -Rm/Lm & 0 & 0 & 0 & 0 \\ 0 & 0 & 1 & 0 & 0 \\ Kt/Jm & (-K*r*r-Km)/Jm & -B/Jm & K*r/Jm & 0 \\ 0 & 0 & 0 & 0 & 1 \\ 0 & K*r/M & 0 & -K/M & 0 \end{bmatrix}$$

Bg = [1/Lm 0 0 0 0], Cg = [0 0 0 1e6 0], Dg = [0]
The transfer function of the system is given by $G_p(s) = C_g(SI - A_g)^{-1}B_g + D_g$. These equations are used to create a state-space model of the system. The input is the voltage applied to the armature (v_a) and the output is the position of the slide (x). The variables K, K_m, and B are given in Table 2.

B	System damping	3.168 N-m/rad/sec
K_m	Torsional stiffness	1490 N/rad
K	Interface stiffness	$373.9 \cdot 10^6$ N/m

Table 2: Values used in the system model

4. PID CONTROL

To compare the PID scheme to the state feedback/PID scheme both controllers were designed to operate at a sample frequency of 3000 Hz. This is the same frequency at which the state feedback/PID controller operates. The controller was designed in the discrete domain using a discretized version of the state space servo model of the system. The discrete model was obtained by using the zero-order hold approximation.

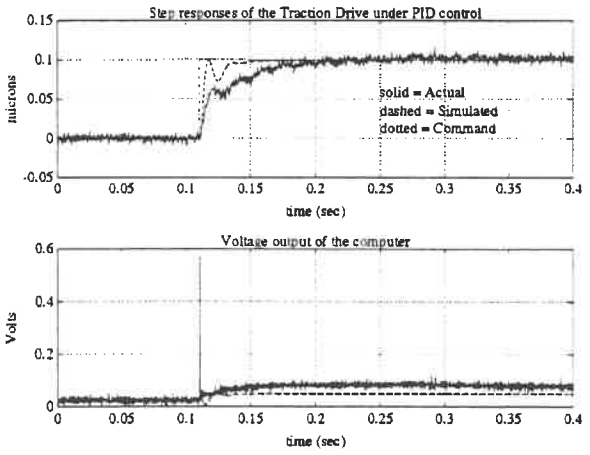

Figure 3: Simulated and actual step responses under PID control

The design procedure has a phase margin goal of 50 degrees [4]. The gain margin was kept above 20 dB to insure robustness to parameter changes. This was done by adjusting K_I and K_D. A plot of the step response under PID control is given in Figure 3. The actual

system has a slightly slower step response than that predicted by the model. This may be due to variations in the system damping. The system settles to the commanded value of 0.1 μm in 0.1 seconds with no overshoot.

5. State Feedback/PID Control

To increase the speed of the response, a state feedback control system is used. The roots of the closed loop system are chosen so that the system has a faster response and is not forced into saturation for small step commands. Once pole locations are selected, Ackermann's formula can be used to calculate the feedback gain matrix K.

As the traction drive system has only one output, the other states have to be reconstructed. This is done with a prediction observer. The poles of the observer are chosen to be 2 times faster than the poles of the closed loop system. This ensures that the observer settles faster than the system. The observer matrix G can then be calculated using Ackermann's formula [5]. The states and the output are given by.

$$q(k+1) = (A - G \cdot C)q(k) + G \cdot y(k) + B \cdot u(k) \quad (3)$$

$$u_{sf}(k) = -K \cdot q(k) \quad (4)$$

In these equations, $q(k)$ is the vector of estimated states, A, B and C are the system state space matrices, $y(k)$ is the system output and $u_{sf}(k)$ is the system input or state feedback controller output. Equations (3) and (4) form a regulator control system for the traction drive.

As the open loop system has no free integrators, the regulator exhibits steady-state errors to step commands. An integrator can be added to the forward loop but this will slow the system down. Alternatively, an outer PID control loop can be used to track step commands without seriously affecting performance. The PID is designed on the closed loop system formed by the state feedback controller using the PID design method described above. The controller output is then the sum of the PID and state feedback outputs. A block diagram of the closed loop system is given in Figure 4. A plot of the simulated and actual step responses is given in Figure 5. The responses match closely. The output settles to the commanded value of 0.1 μm in 0.025 seconds with very little overshoot.

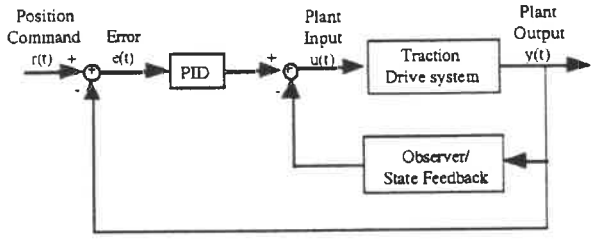

Figure 4: Block diagram of the closed loop system under State feedback/PID control

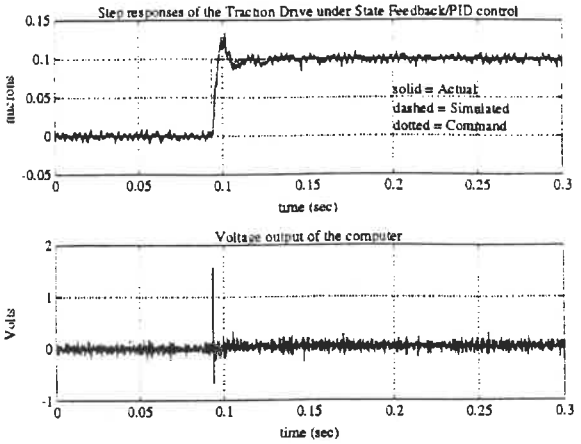

Figure 5: Simulated and actual step responses under state feedback/PID control

The performance and characteristics of both the PID and state feedback/PID control schemes can be compared. Table 3 shows the properties of the closed loop system under both control schemes. For comparable gain and phase margins, the state feedback/PID control scheme has a faster settling time and a larger bandwidth.

Scheme	Gain Margin	Phase Margin	Settling Time	Band-width
PID	20.6 dB	47.6	0.1 sec	25 Hz
State Feedback/PID	21.4 dB	49.8	0.025 sec	70 Hz

Table 3: Comparison of control schemes.

The step response times show that the state feedback/PID controller is about 4 times faster than the PID controller. It settles in 25 ms whereas the PID controller takes 100 ms. In actual machining, however, step commands are rarely used. Ramp (velocity) or sinusoidal signals are much more common. To test the ability of these controllers to follow sinusoidal signals a test similar to the Low Amplitude Sine Tracking test developed at Rank Pneumo was used [6]. Unfortunately, the limited range of the capacitance gages restricted the velocity of the slide. Instead of a low frequency high amplitude signal, a 2 Hz sine wave with a two micron amplitude was used. This is a more stringent test of controller performance than a low frequency low amplitude signal and the following errors are more noticeable. A plot of the tracking errors under both schemes is given in Figure 6. This figure shows that the error is within 0.05 microns under state feedback/PID control and is nearly 0.25 microns under PID control. To test the ability of the controllers to reject disturbances, another test was conducted during which the slide was disturbed with a steel ball 19 mm in diameter rolled from a fixed height while the controllers held position. The response to this

disturbance under both control schemes is given in Figure 7. The state feedback/PID scheme limits the amplitude of the disturbance and brings the system back in less than one third the time.

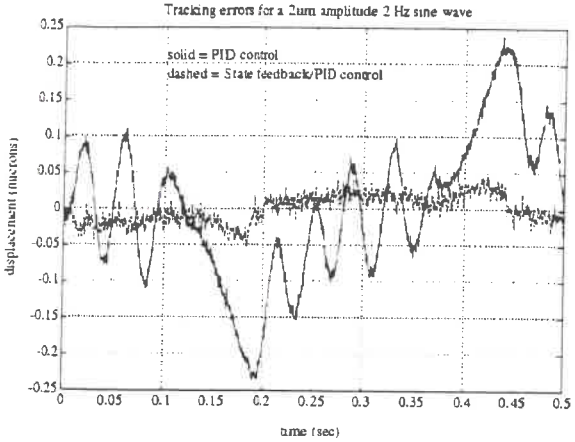
Tracking errors for a 2um amplitude 2 Hz sine wave
solid = PID control
dashed = State feedback/PID control
displacement (microns)
time (sec)

Figure 6: Comparison of 2 Hz sine tracking errors

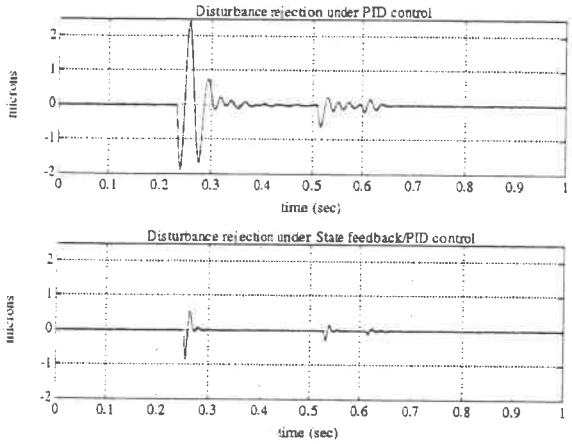

Figure 7: Comparison of disturbance rejection

6. H-∞ Optimal Control

The schematic of the H-∞ control system is shown in Figure 8. In this figure, the controller, plant and disturbance are denoted by $C_o=C_{on}/C_{od}$, $G_p=B/A$ and $d=C/A$. Where

$$A = 1 - 0.6926z^{-1} + 0.5933z^{-2}$$
$$B = 0.7039 + 1.7061z^{-1} + 1.2788z^{-2}$$
$$C = 1$$

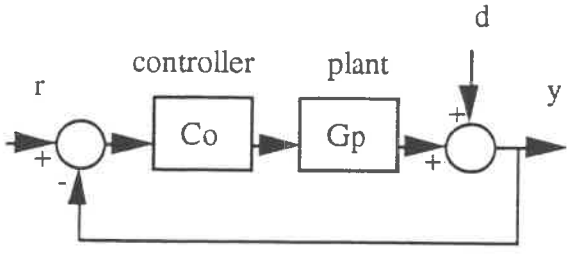

Figure 8: Schematic of the system

In the past decade, H_∞ control theory has received considerable attention. A number of techniques have been presented for solving the H_∞ control problems, but many of them are too complicated and difficult to implement. Polynomial solutions of the H_∞ control problem developed in discrete time by Grimble appear to be both simple and numerically reliable [7]. The highlight of the algorithm is as follows. Let

$$S = (1 + C_oG_p)^{-1} \quad \text{(sensitivity)}$$
$$M = C_o(1 + C_oG_p)^{-1} \quad \text{(control sensitivity)}$$

The disturbance power spectrum is written as Φ_{dd}. The power spectra of controller input and control signal are $\Phi_{ee} = S\Phi_{dd}S^*$ and $\Phi_{uu} = M\Phi_{dd}M^*$, respectively. Here S^* and M^* denotes the adjoint of S and M. The following cost function is to be minimized

$$J_\infty = \| X(z^{-1}) \|_\infty \quad (5)$$

where

$$X(z^{-1}) = \Phi_{ee} + \Phi_{uu} \quad (6)$$

Following the algorithm given by [7], we end up with the following H_∞ controller:

$$C_{on} = 0.8303 - 0.7067z^{-1} + 0.3343z^{-2}$$
$$C_{od} = 1 - 0.2794z^{-1} - 0.7206z^{-2}$$

An H_∞ controller and a PID controller have been implemented and some experiments were performed. As the mass change is a major concern in the model perturbation, the responses of the two control systems are compared on this basis. Two kinds of controllers, PID and H_∞, were initially designed for the same nominal mass, M. The mass is then changed to 2M to compare the changes of system characteristics. The command inputs were 0.1 μm step. The experimental results using the H_∞ controller and the PID controller are shown in Figure 9 and Figure 10. For 0.1μm step responses shown in Figure 9, the actual settling time of the H_∞ control system for nominal mass M is about 0.07s. Although the mass changed from M to 2M, the settling time remained at 0.07s which means that the system is insensitive to mass change. For 0.1 μm step responses shown in Figure 10, the actual settling time of the PID control system for nominal mass M is about 0.08s; when the mass was changed to 2M, the settling time became 0.2s.

7. Conclusions

The traction drive is a system with static friction and variable stiffnesses and damping. In spite of these nonlinearities, a fifth order linear model provides a good representation of the actual system. This model is used to design digital controllers for the traction drive.

Two types of controllers are designed, implemented and tested. The first is a PID controller. The second is a state feedback controller with an outer PID loop to eliminate steady-state errors to step commands. From experiments, it is apparent that the state feedback/PID control scheme is better at tracking command signals than the PID controlled system. The state feedback/PID system is also better at rejecting disturbances. The larger bandwidth shows that the system is quicker and able to respond to faster command signals. The system also has high gain and phase margins which makes it robust to changes in certain system parameters.

Finally, experimental results show that the robustness of the H_∞ control system is much better than that of the PID system with respect to mass change. Future tasks are to improve the noise rejection characteristic of the H_∞ control system.

8. REFERENCES

[1] Youden, D. "Capstans or Lead Screws? Comparing the Performance of Diamond Turning Machines Under Operating Conditions,". in Seventh Annual Meeting of the American Society for Precision Engineering. 1992. Grenelefe, Florida:

[2] Phillips, C.L. and R.D. Harbor, *Basic Feedback Control Systems*. Alternate 2nd ed. 1991, Englewood Cliffs: Prentice-Hall.

[3] Francis, B.A., "A Course in H_∞ Control Theory", New York: Springer-Verlag, 1987.

[4] Phillips, C.L. and H.T. Nagle, *Digital Control System Analysis and Design*. 2nd ed. 1990, Englewood Cliffs, NJ: Prentice Hall.

[5] Brogan, W.L., *Modern Control Theory*. 1991, Englewood Cliffs, NJ: Prentice-Hall.

[6] Gerchman, M.C. and D.H. Youden, "An Evaluation of Ultra-precise Machine Tool Contouring Performance: The Low Amplitude Sine Tracking (LAST) Test," in Progress in Precision Engineering. 1991. Braunschweig, Germany: Springer-Verlag.

[7] Fragopoulos, D., Grimble, M.J., Shaked, U., " H_∞ Controller Design for the SISO Case Using a Weiner Approach", IEEE Transactions on Automatic Control, Vol. AC-36, No.10, pp.1204-1208, Oct.1991.

[8] Brown, G.D., Grimble, M.J. and Biss, D., " A simple, efficient H_∞ Controller algorithm", Proceedings of the 26th Conference on Decision Control, LA, 1987.

[9] Grimble, M.J., " Optimal H_∞ Robustness and the relationship to LQG design problems ", *International Journal of Control*, vol. 43, No. 2, pp.351-372, 1986.

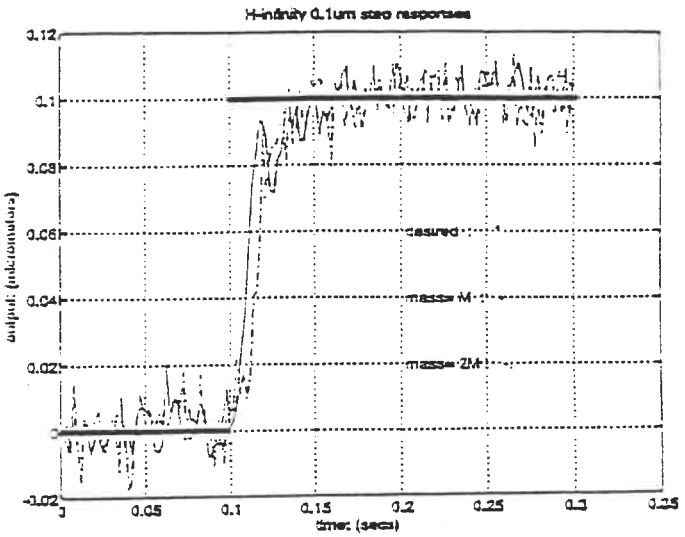

Figure 9: H-∞ 0.1μm Step Response

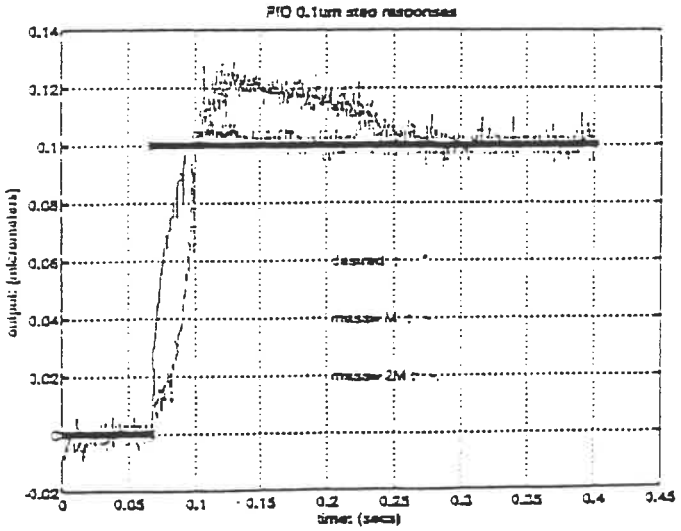

Figure 10: PID 0.1 μm Step Response

DEVELOPMENT OF DESIGN RULES FOR FRICTION WHEEL DRIVES.

Nick Rosielle,
Eindhoven University of Technology,
Faculty of Mechanical Engineering,
Section Precision Engineering.

Friction wheel drives used in high precision machines and instruments have many fine properties, such as high stiffness, linearity, low friction and little virtual backlash. They are also compact and show minimum heat dissipation.
With a considerable number of assumtions, their accuracy in motion transfer can be calculated[1]. Motion loss in the order of 1 to 10 ppm of travelled distance[2] can be expected but is dependent on factors such as preload and traction[3], wheel alignment[4], wheel geometry[5], surface characteristics[6], and material properties[7].

At the Precision Engineering group[8] of the Eindhoven University of Technology an investigation in this area[9] includes an experimental verification. For this purpose a measurement set-up was recently built of which the mechanical part[10] contains many features that can be described as state of the art design principles[11].

On the mechanical side there are two high accuracy wheels[12] in contact. The contact force in normal direction is adjustable[13], the traction force is measured continuously[14] during dynamic testing[15]. One wheel's rotation is adjustable in spin[16] and tracking angle[17] by piezo actuators acting through manipulators[18] on a hysteresis free spherical bearing[19]. That bearing consists of "folded leafsprings"[20] cut from a block by wire spark erosion.
The other wheel is supported on an elastic straight guide[21] which was also cut from a single piece of material. The small elastic force required to move this wheel axially is compensated using negative stiffness[22].

Measurements are made with commercial instruments[23] with on the fly data gathering (pc-board). Various servo drive concepts can be tested as motortype and control systems influence is expected to be noticeable from literature[24].

Future use of the apparatus focusses among other subjects on wheel development, materials testing and dynamic runout compensation.

Notes.

1 See K.L. Johnson Contact Mechanics, ISBN 0521 347963, based on work by Kalker, Delft (Netherlands)
2 See Fig. 7, vertical axis shows creeprate multiplied by 10^5.
3 See Fig. 7, preload on the horizontal axis [N], traction from 20 to 2 [Nmm].
4 See Fig. 9, zero angle is for zero axial force, yielding minimum creep.
5 See Fig. 1, the waviness on the slope is caused by excentricity and out of roundness.Fig. 1 to 4 show reproducebility of these geometrical effects.

Notes continued.

6 Surface roughness influence is not noticeable when smooth i.e. height less than 5% of wheel contact compression in normal direction. See G.T. Nielsen in WEAR,170(1993)71-77 on surface layers

7 Youngs modulus and Poison modulus and to a negligible extend kinetic friction coefficient.

8 Prof.Dr.Ir.Schellekens heads this group.

9 Doctors thesis N.Rosielle due october 1994.

10 See slides at the meeting.

11 Statically determined instrument design using monolytic elastic elements for minimum hysteresis.

12 Diametre 100 mm, $<0.2\ \mu$m peak valley out of roundness, cylindrical wheel on elastic straight guide of fig 14, spherical wheel on elastic spherical bearing fig. 10,11

13 See table 1, a low stiffness spring is used.

14 a piezoelectric force transducer is used.

15 velocity profiles can be set via a second PC which communicates with the servo system.

16 See fig. 16.

17 See fig. 15.

18 See fig. 12,13.

19 See fig. 10,11, slides at the meeting.

20 See fig. 11, slides.

21 See fig. 14.

22 See fig. 17.

23 Each wheel's rotation is measured with a Heidenhain ROD 800c 36000 marks/rev. encoders, fourfold evaluation, 25 fold interpolation, connected to a IK120 card in a 486PC 50 Mhz,8MB 200Mb HD.
Axial displacement is measured with an inductive probe.

24 Thesis Torsten Bispink Aachen, ISBN 3-86111-275-2

quantity to be measured	symb.	units	range	resolution
creep rate	ξ_x	-	$\pm(10^{-6}\text{ -}10^{-3})$	10^{-6}
traction force	Q_x	N	$\pm(10^{-2}\text{ - }10^{1})$	10^{-2} N
axial displacement	y	m	$\pm(0\text{ - }2.10^{-4})$	10^{-6} m
angular velocity	ω	rad/s	$\pm(0\text{ - }10^{2})$	10^{-1} rad/s

Adjustable parameters	symb.	units	range	resolution
normal force	P	N	5.10^{2}	<1 N
tracking angle	θ	rad	$\pm4.10^{-4}$	5.10^{-6} rad
spin angle	φ	rad	$\pm4.10^{-2}$	5.10^{-6} rad

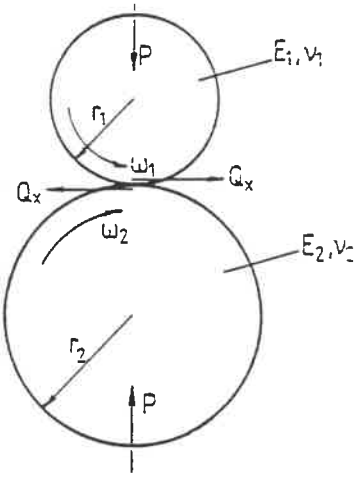

Table 1

Motion loss vs travelled distance

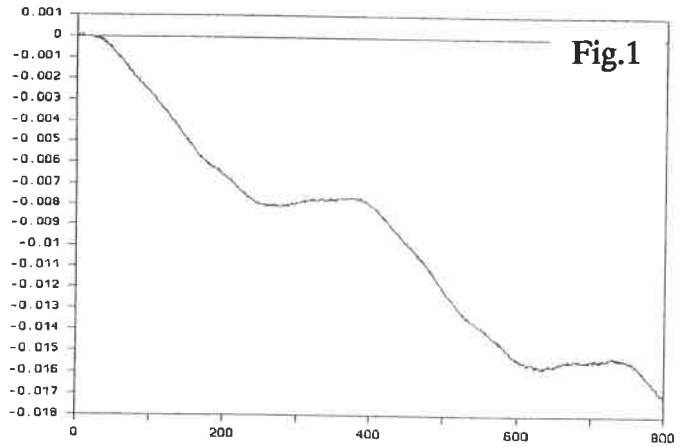

Fig.1

Two revolutions of fig. 1
second rev. offset

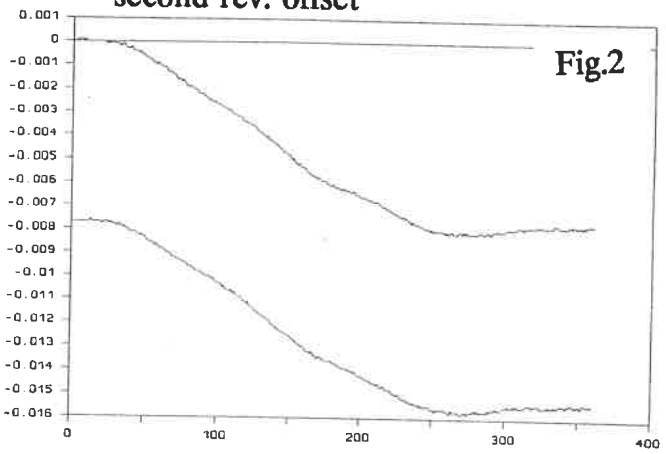

Fig.2

Difference of two graphs of fig. 3

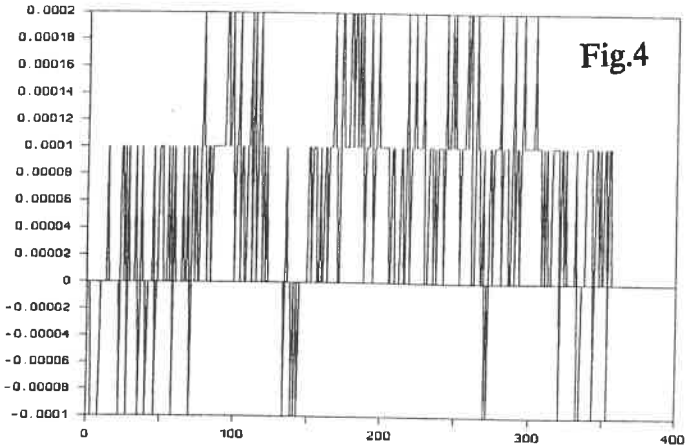

Fig.4

Fig.2's data superimposed

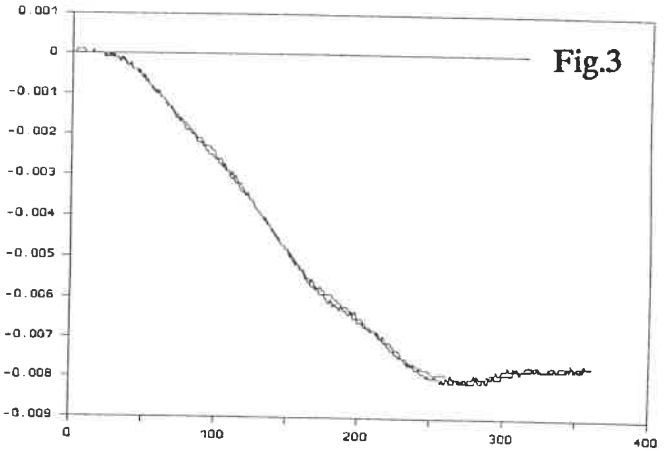

Fig.3

Differnce divided by travelled distance vs travelled distance

Fig.5

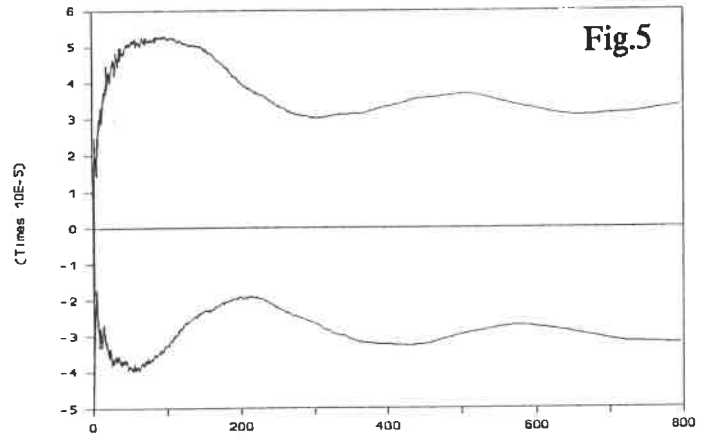

Four levels of normalforce yield four creeprates (one rev. shown)

Fig.6

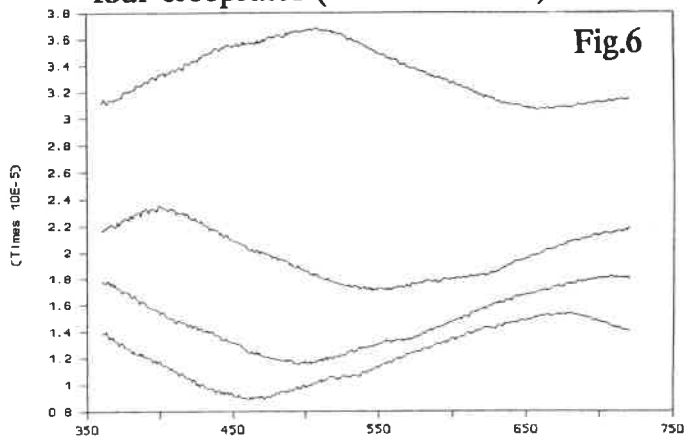

Calculated creepratio of machine as a function of Normalforce

Fig.7

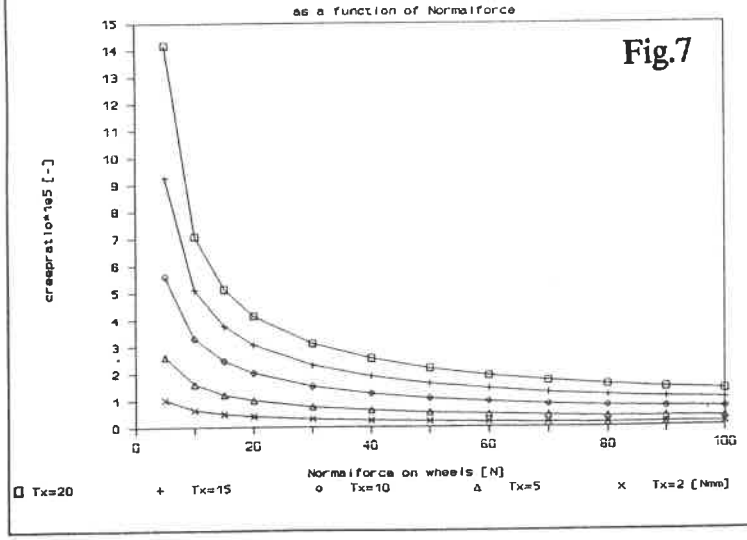

Measured graph shows lower creep rate than top graph calculated at same torque.

Fig.8

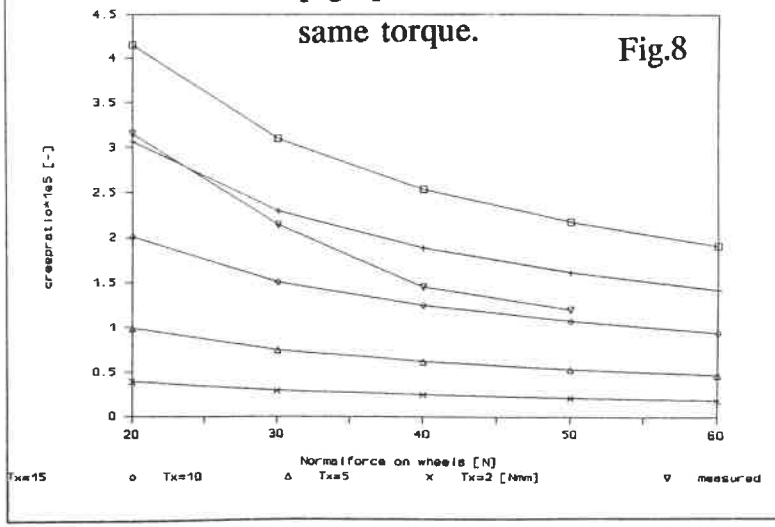

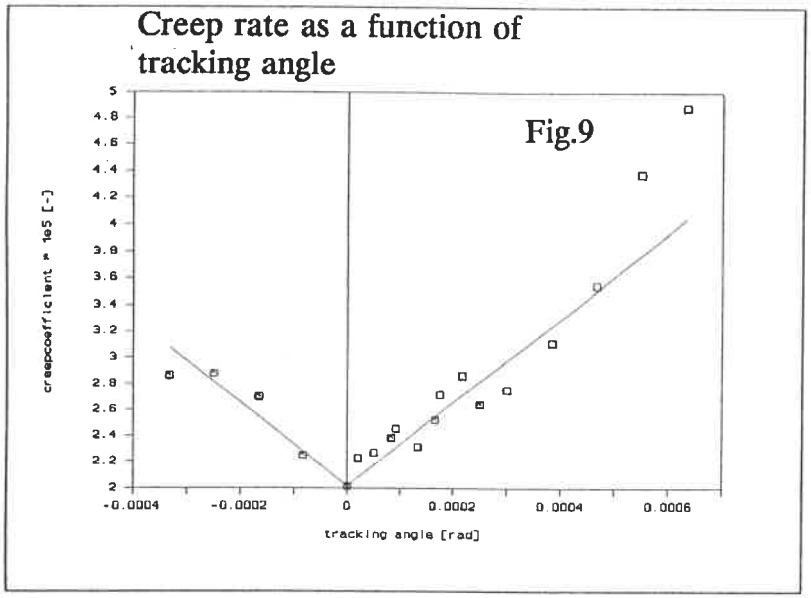

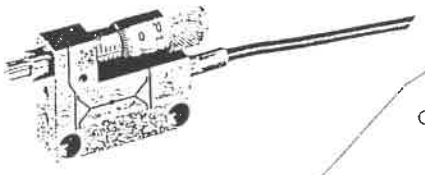

Fig.13
Piezoactuator

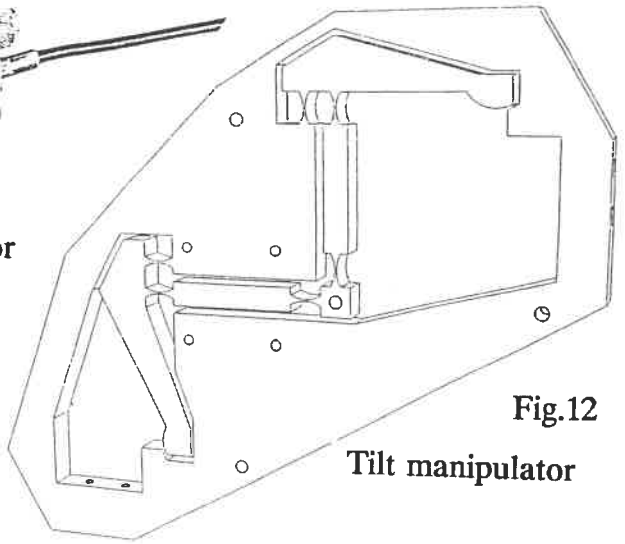

Fig.12
Tilt manipulator

Spherical Bearing

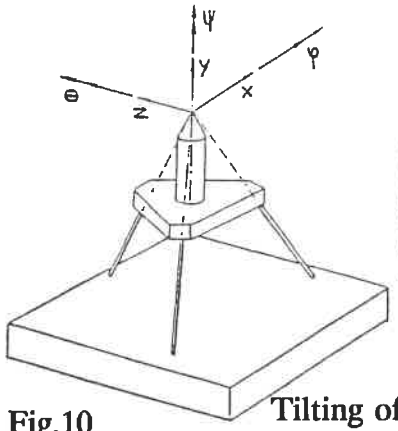

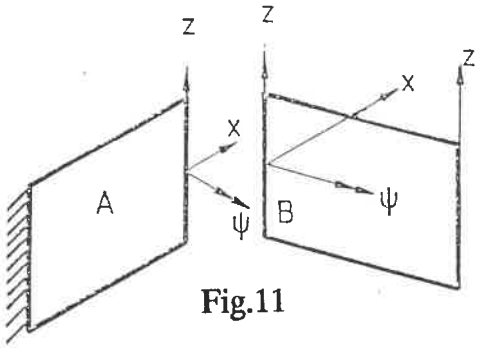

Fig.11

Fig.10

Tilting of one axis is done by supporting it on an elastic spherical bearing (Fig. 10) which allows 3 rotations about the origin of xyz. Folded leafsprings can replace the three rods. They are axially stiff (Fig. 11).

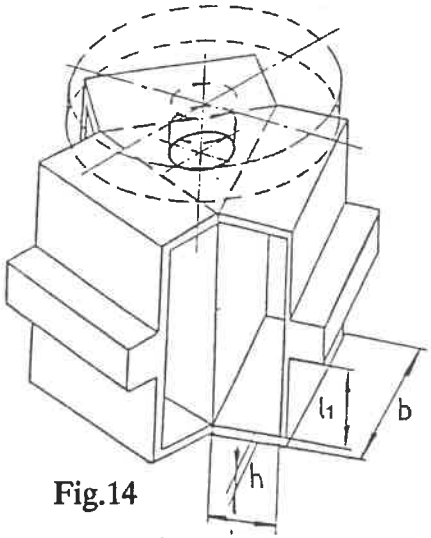

Fig.14

Axial straight guide,
six folded leafsprings.

Tracking angle

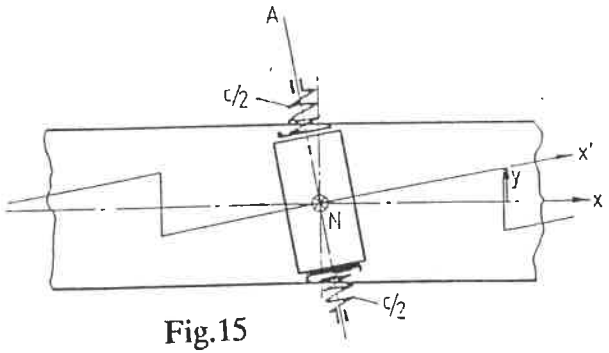

Fig.15

Spin angle

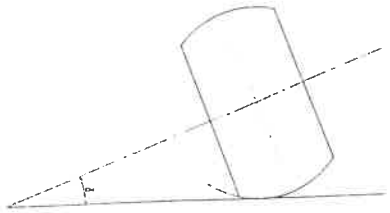

Fig.16

One wheels axis is adjustable through tracking and spin angle by an elastic manipulator (Fig. 12) and two piezomike actuators. (Fig. 13) The rotation point of the spherical bearing (fig. 10) is at the contact of the two wheels. The tilted axis carries a spherical shape wheel whereas the other wheel is cylindrical. The folded leafsprings of Fig.10/11, Fig. 14 and Fig. 18 were all cut in monobloc style by wire spark erosion to prevent the usual hysteresis of leafspring clamping.

Spin and tracking force (both axial) differ: spin force is not changing sign when rolling direction is reversed. Hence symmetrical test setup for reversals.

Negative stiffness from buckled leafspring.

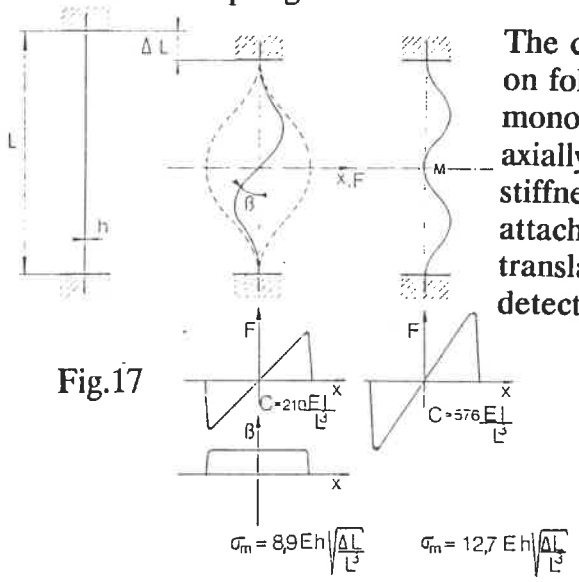

Fig.17

The cylindrical wheel is supported on folded leafsprings cut from a monobloc so it can freely translate axially. Fig. 14. A negative stiffness mechanism (fig. 17) is attached to provide zero force translation to allow axial force detection.

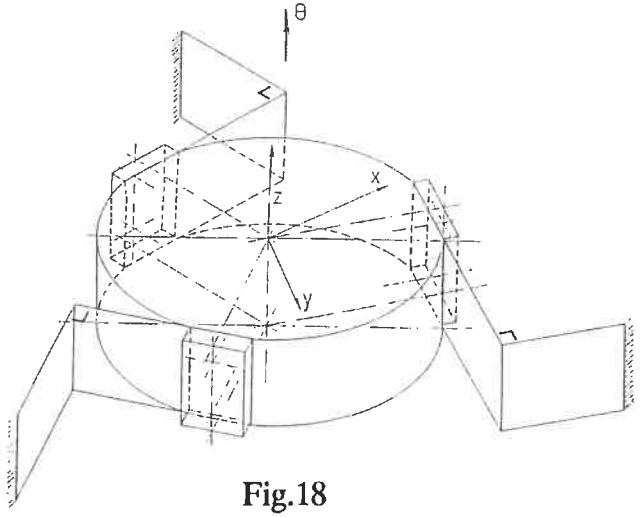

Fig.18

Again folded leafsprings were used to provide two translations for traction measurement and contact compression.

Experimental Analysis of Grinding Wheel Head Feed Mechanism on Plain Bearing Guideways with Force-operated Linear Actuator

A. Kanai, M. Miyashita, Y. Kishimoto
Ashikaga Institute of Technology, 236 Omae, Ashikaga, Tochigi 326, Japan

1. Introduction

One of the today's arts of design principles of feed mechanism in ultraprecision machine tools is to reduce a feed load such as plain bearing frictional load as far as possible. Therefore, aero-or hydro-static bearing guideways are generally applied. In a feed mechanism of hydrostatically supported slide, there exists inevitably a cut-off frequency of servo system, and the stiffness in feed direction is much reduced in the frequency range over the cut-off frequency. Therefore, under grinding load involving higher frequency components relatively to cutting load, today's ultraprecision machine tools can not be expected sufficiently high stiffness to grinding load.

In a discussion on application of slide feed system on plain bearing guideways, the following defects :

(1) reduction of feed resolution due to stick-slip phenomena and others caused by frictional load, and

(2) deformation of a slide and guideway construction accompanied by frictional load and reaction

are mentioned and also the following expectation :

(3) increase of damping effect by introduction of frictional load of the slide system

is told. Further, for an introduction of plain bearing guideways to ultraprecision machine tools,

(4) database of friction characteristics of plain bearing guideways in a displacement range less than several 100 nm

is required.

The authors have proposed the ultraprecision and high stiffness positioning servo mechanism for feeding a slide on plain bearing guideways with the force-operated linear actuator and have realized the stick-slip free servo mechanism with a feed resolution less than 10 nm. Using this test rig, the frictional characteristics of the 150 kg slide has been studied in a fine displacement range less than 100 nm[1][2][3].

The present paper reports the following experimental test results on the static and dynamic stiffness of the grinding wheel head feed mechanism on plain bearing guideways against external loads, which is related with (3) and (4). Structural deformation relative to (2) will be reported separately.

The conclusion is summarized as follows :

(1) static stiffness : load share ratio of the plain bearing guideways to the applied load is about two third, and one of the slide feed actuator is about one third. Then , the effective static stiffness of the actuator increases to about three times.

(2) dynamic stiffness : more than 90% of the external load is resisted by the friction. It means that a damping effect of the frictional load of plain bearing guideways is extraordinary high.

2. Centerless grinding machine used for experiments

Fig.1 shows a construction of the centerless grinding machine used for experiments, which is specified by the following structure :

wheel support mechanism : hydrostatically supported on stationary spindle[4]
guideways : plain bearings with specified contact pressure using pressurized pads
feed mechanism : servo system with force-operated hydraulic actuator[5]
mass of grinding wheel head involving grinding wheel assembly : 100 kg

Fig.2 is a sectional construction of the slide and guideways. Fig.3 is a configuration of displacement sensors for the slide movement, where

sensors A, B and C : sensors for measuring a displacement of the front of grinding wheel head relative to the regulating wheel head,

sensor D : sensor for measuring a displacement of the rear of grinding wheel head relative to the bracket, to which the feed actuator is mounted

sensitivity of the sensors : 400 mV/μm

3. Feed characteristics of grinding wheel head on plain bearing guideways

Fig.4 shows a feed characteristics of the grinding wheel head with the feedback sensor D for 5 nm/step feed command. Fig.5 shows a similar characteristics with the feedback sensor B at the front of the head. Both figures show the response of 5 nm/step resolution at the feedback sensor, but some structural deformation and motion error are included. Yawing observed from the difference between readings of the sensors A, B and C is caused by asymmetric loads of vertical guideway bearings at the driving point. And the difference between readings of the sensors at the rear and front of the grinding wheel head is predominantly caused by the elastic deformation of the bracket.

4. Static stiffness of grinding wheel head feed mechanism

4.1. Frictional load characteristics of grinding wheel head on plain bearing guideways

Fig.6 shows a typical test result of frictional load characteristics of the grinding wheel head on plain bearing guideways, where

travel range : 4 μm

feed rate : 0.8 μm/sec

stationary frictional load : approx. 190 N

4.2. Static stiffness of grinding wheel head feed mechanism

Fig.7 is a layout of the stiffness measuring system. Hydraulic shaker is mounted on the bed instead of the regulating wheel head and applies load to the grinding wheel head. In Fig.8, F_{ex} is an exciting force of the shaker and X_{wh} is a relative displacement of the head front to the bed measured with sensor A.

F_{ex} = 130 N ± 98 N, where the bias = 130 N and the periodical load = ±98 N. Static stiffness of the head feed mechanism at the front is 0.84 N/nm.

4.3. Static stiffness of the grinding wheel support mechanism relative to wheel head

Fig.9 is a layout of the stiffness measuring system. The shaker applies load to aluminum wheel instead of grinding wheel. In Fig.10, X_{gw} is a relative displacement of the wheel front to the grinding wheel head measured with the sensor A.

F_{ex} = 125 N ± 99 N is applied. Static stiffness of the grinding wheel support mechanism relative to the head is 0.27 N/nm.

4.4. Static transfer characteristics of external load in feed direction to feed actuator through plain bearing guideways

In Fig.11, F_{dr} is a driving force to keep the head against the exciting force. F_{ex} = 125 N ±99 N is applied. From the Fig.11, F_{dr}/F_{ex} is about 0.38. It means that a load share ratio against the exciting force between the bearing friction and the driving force is 62% to 38% approximately.

5. Dynamic stiffness of the grinding head feed mechanism

5.1. Layout of stiffness measuring system and test condition

Configuration of the sensors and the shaker is similar to Fig.7. Exciting force in the frequency range measured is kept constant within ±3 dB, and exciting force F_{ex} = 100 N ± 50 N and 300 N ± 50 N are applied, where stationary frictional load of the guideways is 190 N, the bias of exciting force is 100 N or 300 N and amplitude of sinusoidal exciting force is 50 N. Measured frequency range is 5 to 500 Hz or 0.5 to 50 Hz.

5.2. Dynamic stiffness of the grinding wheel head feed mechanism

Fig.12 (a), (b) and (c) is a typical example of the test results under F_{ex} = 100 N ± 50 N. Table 1 and 2 are summary. The stiffness F_{ex}/X_{wh} is 1.1 N/nm at 0.5 Hz, 0.63 N/nm at 10 Hz and increases in the frequency range over 100 Hz rapidly.

5.3. Dynamic transfer characteristics of external load in feed direction to feed actuator through plain bearing guideways

In Fig. 12(c) load share ratio F_{dr}/F_{ex} is 0.32 at 0.5 Hz and decreases to less than 0.1 in the frequency range over 10 Hz. That is, a damping effect of the plain bearing guideways is predominantly shown here.

6. Dynamic stiffness of grinding wheel support mechanism relative to wheel head

Layout of the stiffness measuring system is similar to Fig.9. Fig.13(a), and (b) is an example of the test results under F_{ex} = 100 N ± 50 N. Table 3 is compliance of the grinding wheel support mechanism relative to the head front and at the feedback point relative to the bracket. The stiffness F_{ex}/X_{gw} is 0.26 N/nm at 5 Hz and 1.5 N/nm at 100 Hz.

7. Summary

(1) 38% of the external load is shared by the friction of plain bearing guideways statically. More than 90% of the external load is shared by the friction in the frequency range over 10 Hz. It means that a damping effect of the friction of plain bearing guideways is extraordinary high.

(2) Static and dynamic stiffness of the grinding wheel support system involving the head feed mechanism at the wheel front is dominated by the wheel support mechanism.

References

(1)A. Kanai, M. Miyashita and J.Yoshioka, Proceedings of the 6th Annual Meeting of ASPE, 80(1991)

(2)A. Kanai, M. Miyashita and H. Nishihara, Proceeding of the 7th Annual Meeting of ASPE, 126(1992)

(3)A. Kanai, M. Miyashita and S. Uchida, Proceedings of the 8th Annual Meeting of ASPE, 54(1993)

(4)J. Yoshioka, M. Miyashita, A. Kanai, M. Daito, and F. Inaba, Proceedings of the 4th Annual Meeting of ASPE, 126(1989)

(5)A. Kanai, H. Sano, J. Yoshioka and M. Miyashita, Nanotechnology No.2, 43(1991)

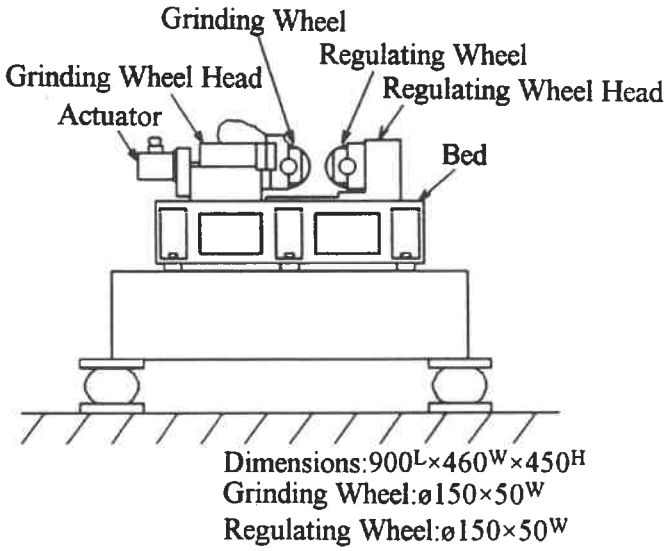

Fig. 1 Centerless grinding machine for experiments

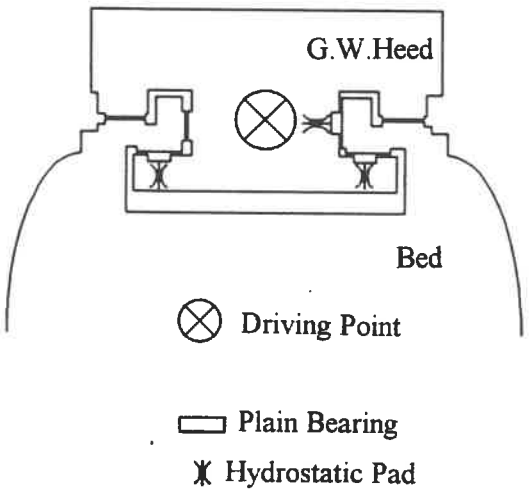

Fig. 2 Construction of slide and guideways

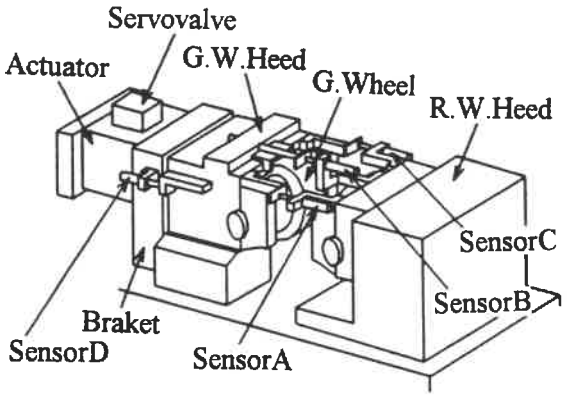

Fig. 3 Configuration of displacement sensors

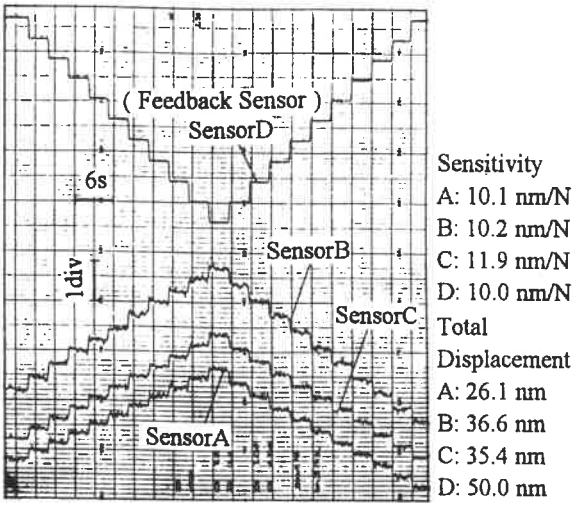

Fig. 4 Feed characteristics of grinding wheel head
(5 nm/step feed, feedback sensor : D)

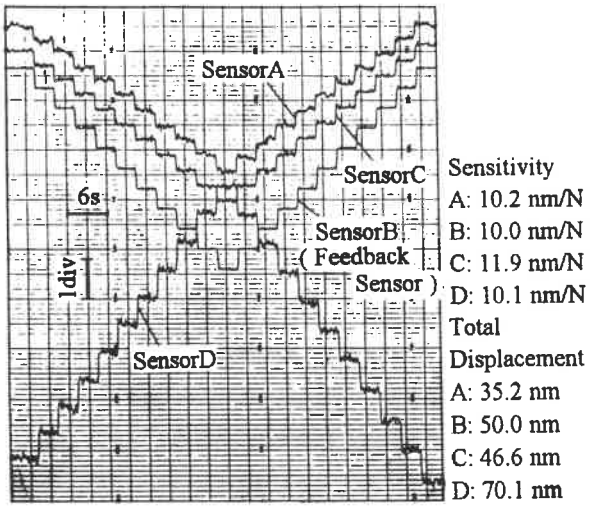

Fig. 5 Feed characteristics of grinding wheel head
(5 nm/step feed, feedback sensor : B)

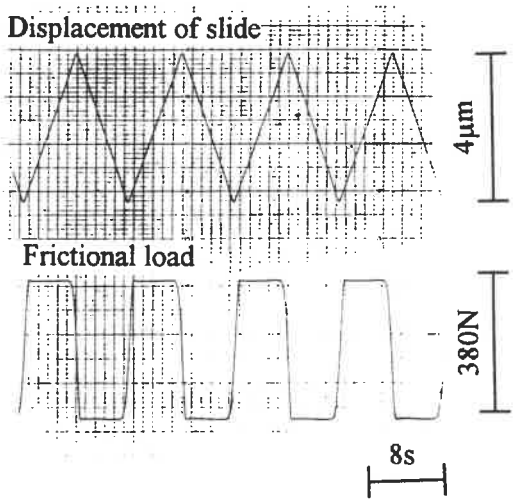

Fig. 6 Frictional load characteristics

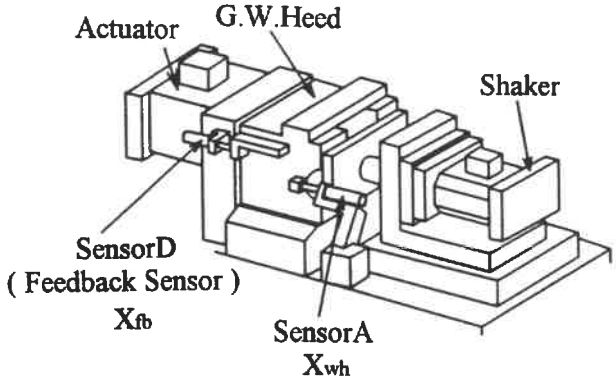

Fig. 7 Stiffness measuring setup
for grinding wheel head feed mechanism

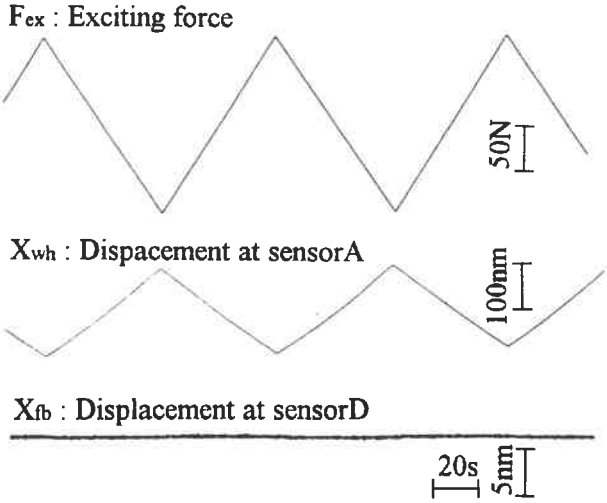

Fig. 8 Static compliance of X_{wh}/X_{ex}

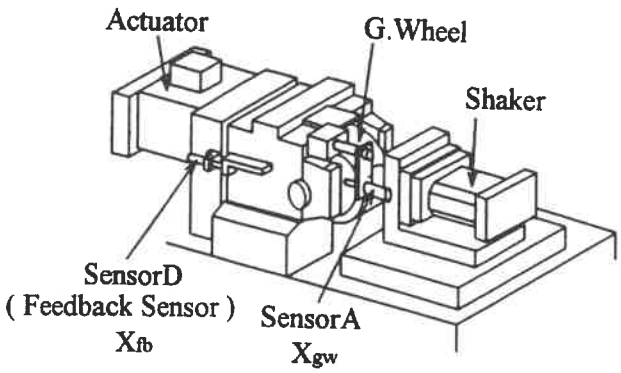

Fig. 9 Stiffness measuring setup
for grinding wheel support mechanism

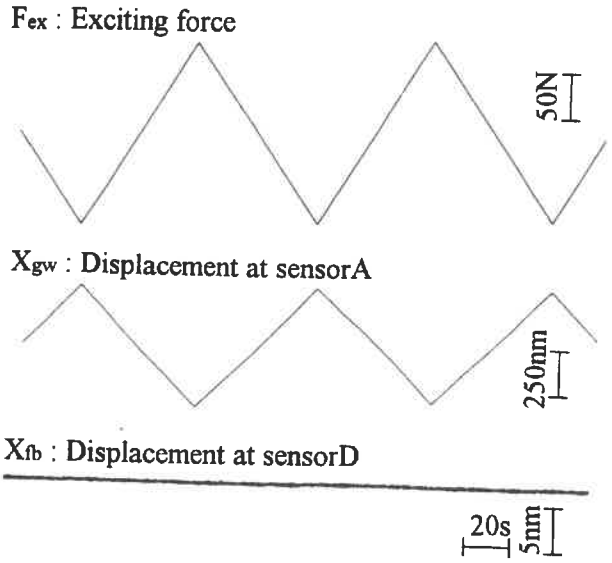

Fig. 10 Static compliance of X_{gw}/F_{ex}

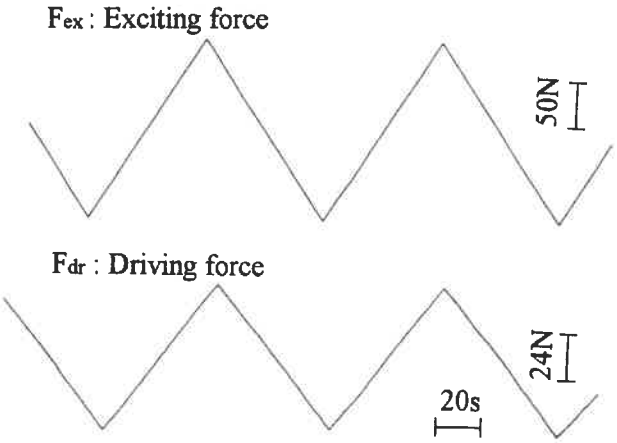

Fig. 11 Static trnsfer characteristics
of external load of F_{dr}/F_{ex}

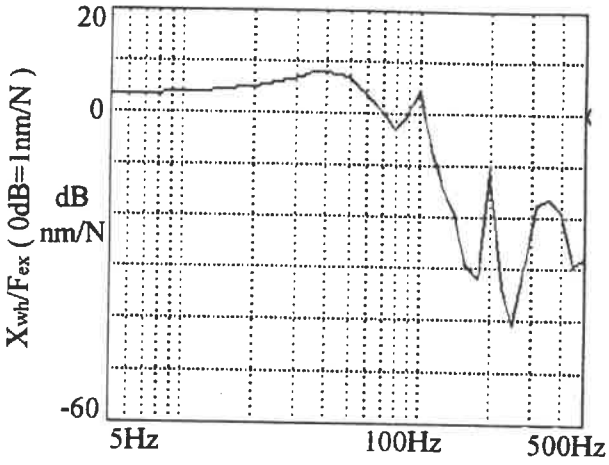

Fig. 12 (a) Dynamic characteristics of X_{wh}/F_{ex}

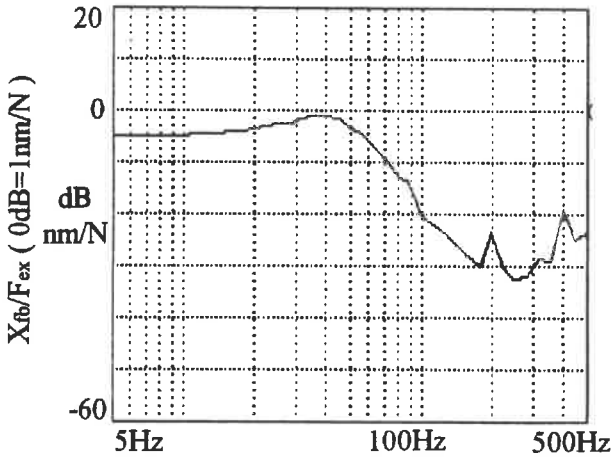

Fig. 12 (b) Dynamic characteristics of X_{fb}/F_{ex}

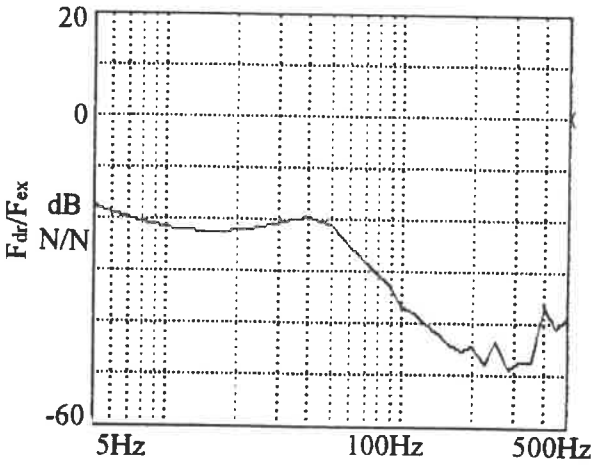

Fig. 12 (c) Dynamic characteristics of F_{dr}/F_{ex}

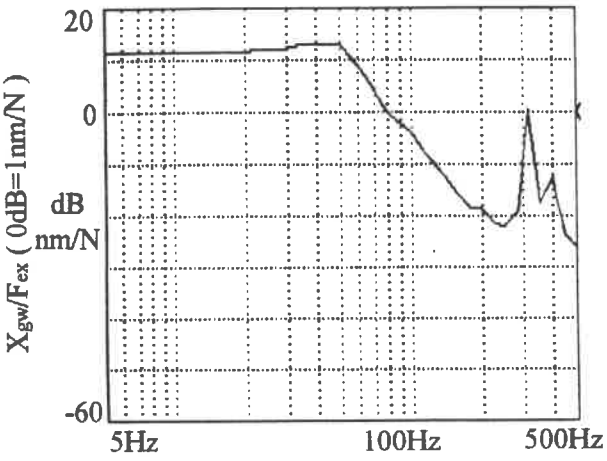

Fig. 13 (a) Dynamic characteristics of X_{gw}/F_{ex}

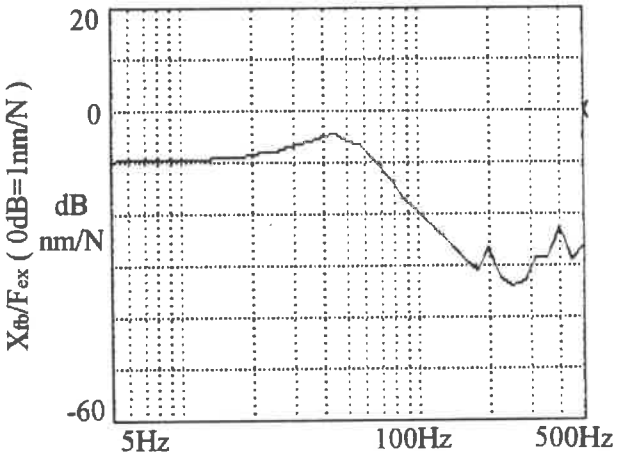

Fig. 13 (b) Dynamic characteristics of X_{fb}/F_{ex}

Table 1 Dynamic compliance of X_{wh}/F_{ex} and X_{fb}/F_{ex}

items	X_{wh}/F_{ex}		X_{fb}/F_{ex}	
bias	100 N	300 N	100 N	300 N
Hz	nm/N	dB	dB	dB
0.50	0.93			
1.00	1.21			
5.00	1.48	+ 0	- 9	- 9
10.00	1.60	+ 0	- 9	- 9
50.00	2.24	+ 3	- 11	- 6
71.25	1.01	+ 4	- 10	- 5
78.75	0.72	+ 5	- 10	- 4
100.0	1.71	+ 3	- 25	- 22
315.0	0.13	- 9	- 11	- 13
500.0	0.04	+ 3	+ 4	+ 6

Values in dB are relative one to X_{wh}/F_{ex} for bias of 100 N.

Table 2 Dynamic transfer characteristics of external load of F_{dr}/F_{ex}

items	F_{dr}/F_{ex}	
bias	100 N	300 N
Hz	N/N	dB
0.50	0.32	
1.00	0.34	
5.00	0.13	- 0.1
10.00	0.09	- 0.2
50.00	0.09	+ 4
71.25	0.04	+ 5
78.75	0.03	+ 5
100.0	0.01	+ 4
315.0	0.004	0
500.0	0.01	+ 1

Values in dB are relative one to F_{dr}/F_{ex} for bias of 100 N.

Table 3 Dynamic compliance of X_{gw}/F_{ex} and X_{fb}/F_{ex}

items	X_{gw}/F_{ex}		X_{fb}/F_{ex}	
bias	100 N	300 N	100 N	300 N
Hz	nm/N	dB	dB	dB
5.00	3.82	- 0	-21	-21
10.00	3.75	- 0	-21	-21
50.00	4.40	+ 0	-19	-17
71.25	1.51	+ 6	-15	- 7
78.75	0.98	+ 5	-14	- 6
100.0	0.65	+ 6	-16	- 7
315.0	1.04	- 6	-29	-39
500.0	0.05	+ 1	- 0	+ 8

Values in dB are relative one to X_{gw}/F_{ex} for bias of 100 N.

Damping Characteristics of Air-lubricated Slideways for Ultra Precision Machine Tools

Shigeo Kato
Nippon Institute of Technology
Miyashiro, Saitama 345, Japan

1. Introduction

Damping characteristics of air-lubricated slideways have been considered to be poor, because the viscosity of air is as small as 10^{-3} compared with the viscosity of spindle oil. Indeed, in the case of damping characteristics only by the viscosity of air, the damping ratio may be in the order of 10^{-3}. Undoubtedly, this small damping ratio is inappropriate for the slideways of the machine tools. Fortunately, it has been found that the air bearings, which are provided with restrictors, can generate a fairly large damping force which is not produced by the viscosity of the air.

This phenomenon may be explained as follows. When the spindle of the air bearing vibrates, the air, which exists in the clearance of the bearing, flows backward by the squeeze effect. This counter current of the air generates the damping force at the restrictors. Therefore, this damping force depends on the density of the air and the air flow rate through the restrictors, not on the viscosity.

This study analyzes the damping force due to the squeeze effect in the case of air-lubricated slideways. The results are applied on a slideway of an ultra precision machine tool, of which the mass of its table is 1500 kg and static stiffness is 0.795 kN/μm. A damping ratio equivalent to 0.085 has been determined to be the typical value of the damping force.

2. Stiffness of the air-lubricated slideway

A cross-section of the air-lubricated slideway is shown in Fig. 1. Clearance between the slider and the guide is H. Width and length of the slider are B and L, respectively. The slider has some orifice restrictors and recesses. Pitch of the recesses is Lr. Diameter of the orifices is d. Diameter and depth of the recesses are D and Hr, respectively. Air pressure, Ps is supplied to the slider.

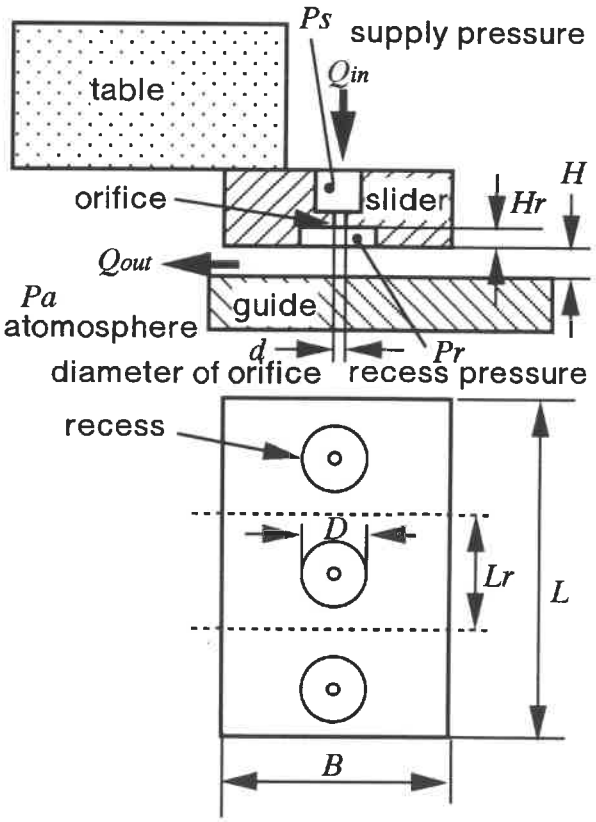

Fig. 1 Air-lubricated slideway

The pressure at the recesses is P_r. An effective area of the sliders is represented by Ae.

Therefore the stiffness of the slideway is shown as Eq. 1.

$$K = -\frac{\Delta W}{\Delta H} = -Ae\ \frac{\Delta P_r}{\Delta H} \qquad (1)$$

In Eq. (1), ΔW and ΔH represent changes from equilibrium of weight and clearance of the slideway, respectively.

Next, four parameters are introduced[1)]

$$\left.\begin{aligned} b_1 &= \frac{H}{Q}\frac{\partial Q_{in}}{\partial H}, \quad b_2 = \frac{H}{Q}\frac{\partial Q_{out}}{\partial H} \\ a_1 &= \frac{P_r}{Q}\frac{\partial Q_{in}}{\partial P_r}, \quad a_2 = \frac{P_r}{Q}\frac{\partial Q_{out}}{\partial P_r} \end{aligned}\right\} (2)$$

where Q_{in} and Q_{out} are mass flow rates into and out from the slider respectively, and Q is the mass flow rate in a state of equilibrium.

Due to the parameters, the net mass flow rate of the slider is represented as

$$\frac{\Delta Q_{in} - \Delta Q_{out}}{Q} = (b_1 - b_2)\frac{\Delta H}{H} + (a_1 - a_2)\frac{\Delta P_r}{P_r} \qquad (3)$$

If the slideway is at equilibrium, the net mass flow rate is 0. Thus from Eq. (3), static stiffness is written as

$$K_s = -Ae\frac{\Delta P_r}{\Delta H} = Ae\left(\frac{P_s}{H}\right)\left(\frac{P_r}{P_s}\right)\frac{(b_2 - b_1)}{(a_2 - a_1)} \qquad (4)$$

In the slideway which has orifice restrictors, Q_{in} is represented as

$$\left.\begin{aligned} Q_{in} &= k_1\left\{\left(\frac{P_r}{P_s}\right)^{\frac{2}{\kappa}} - \left(\frac{P_r}{P_s}\right)^{\frac{\kappa+1}{\kappa}}\right\}^{0.5} \quad \left(\frac{P_r}{P_s} > 0.528\right) \\ &= 0.259\,k_1 \quad \left(\frac{P_r}{P_s} \le 0.528\right) \end{aligned}\right\} (5)$$

and, Q_{out} is shown as

$$Q_{out} = \frac{k_2}{\eta} Pa\left\{\left(\frac{P_s}{Pa}\right)^2\left(\frac{P_r}{P_s}\right)^2 - 1\right\}H^3 \qquad (6)$$

This is based on the following conditions thart k_1 is a constant which is determined by shape of the orifice and the supply pressure, k_2 is a constant which is determined by shape of slider, κ is the ratio of the specific heats of the air: 1.4, and P_a is atmospheric pressure.

From Eqs. (3), (5) and (6), the four parameters are determined as

$$\left.\begin{aligned} &b_1 = 0,\ b_2 = 3, \\ &a_1 = \left(\frac{P_r}{P_s}\right)\left\{\left(\frac{2}{\kappa}\right)\left(\frac{P_r}{P_s}\right)^{\frac{2-\kappa}{\kappa}} - \left(\frac{\kappa+1}{\kappa}\right)\left(\frac{P_r}{P_s}\right)^{\frac{1}{\kappa}}\right\} \quad \left(\frac{P_r}{P_s} > 0.528\right) \\ &\quad = 0 \quad \left(\frac{P_r}{P_s} \le 0.528\right) \\ &a_2 = \frac{2\left(\frac{P_s}{Pa}\right)^2\left(\frac{P_r}{P_s}\right)^2}{\left\{\left(\frac{P_s}{Pa}\right)^2\left(\frac{P_r}{P_s}\right)^2 - 1\right\}} \end{aligned}\right\} (7)$$

The relationship between $(a_2 - a_1)$ and the pressure ratio (P_r/P_s) is shown in Fig. 2.

If the slideway is in a dynamic state, the mass flow rate into the slide and the mass flow rate out from the slide do not balance.

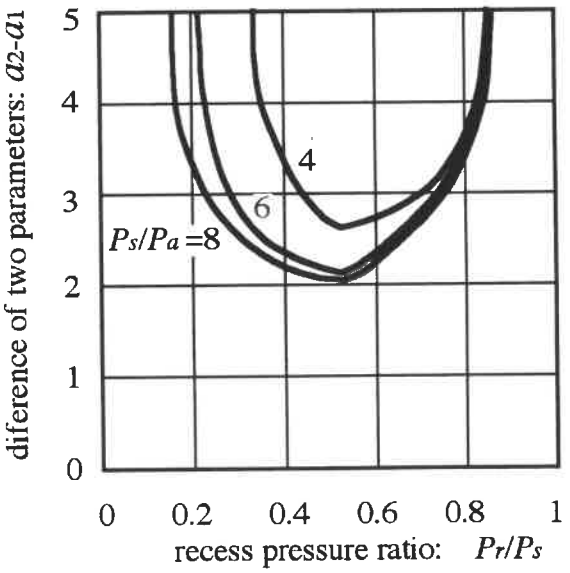

Fig. 2 Relationship between the difference of two parameters: a_2-a_1 and the recess pressure

The difference of the two mass flow rate increases mass in the clearance and recesses. Thus the net mass flow into the slider is

$$\frac{\Delta Q_{in}-\Delta Q_{out}}{Q}=\frac{\rho}{Q}\frac{BLH\,(1+\frac{D}{B})}{2}\frac{d}{dt}(\frac{\Delta H}{H})$$

$$+\frac{\rho}{Q}\{v_r+\frac{BLH\,(1+\frac{D}{B})}{2}\}\frac{d}{dt}(\frac{\Delta\rho}{\rho}) \quad (8)$$

where ρ is air density at the recess and v_r is the recess volume.

The relationship between the recess pressure and the density is

$$\frac{\Delta P_r}{P_r}=n\,\frac{\Delta\rho}{\rho} \quad (9)$$

where n, the polytropic exponent is equal to κ which is the ratio of specific heats.

Combining Eqs. (3), (8), and (9) gives the dynamic stiffness:

$$K_d=-\frac{\Delta W}{\Delta H}=A_e(\frac{P_s}{H})(\frac{P_r}{P_s})$$

$$\times\frac{\{\frac{\rho}{Q}v_c\frac{(1+\frac{D}{B})}{2}s+(b_2-b_1)\}}{[\frac{\rho}{nQ}\{v_r+v_c\frac{(1+\frac{D}{B})}{2}\}s+(a_2-a_1)]} \quad (10)$$

where v_c ($=BLH$) is the clearance volume and s is the Laplace variable.

Now K_c which represents stiffness and C_2 which represents damping coefficient are introduced.

$$K_c=A_e(\frac{P_s}{H})(\frac{P_r}{P_s})\frac{\{n\,v_c\frac{(1+\frac{D}{B})}{2}\}}{\{v_r+v_c\frac{(1+\frac{D}{B})}{2}\}} \quad (11)$$

$$C_2=A_e(\frac{P_s}{H})(\frac{P_r}{P_s})\frac{\{\frac{\rho}{Q}v_c\frac{(1+\frac{D}{B})}{2}\}}{(a_2-a_1)} \quad (12)$$

We call K_c the compressible stiffness and C_2 the damping coefficient due to the squeeze effect at the recess.

From Eqs. (10), (11), and (12), the dynamic stiffness K_d is represented as

$$K_d=K_s\frac{(\frac{C_2}{K_s}s+1)}{(\frac{C_2}{K_c}s+1)}=K_s+\frac{(1-\frac{K_s}{K_c})}{(\frac{1}{K_c}+\frac{1}{C_2 s})} \quad (13)$$

Eq. (13) shows that C_2 is a damping coefficient due to the squeeze effect of the air-lubricated slideway. However, the damper which makes the damping coefficient of C_2 is combined in series with a spring which has the stiffness of K_c. Furthermore, a coefficient of $(1-K_s/K_c)$ is mulitiplied. Therefore C_2 has a damping force only when K_c is larger than K_s.

3. Equation of motion of air-lubricated slideway

An equation of motion of the air-lubricated slideway is

$$m\ddot{x}+K_d\,x=f \quad (14)$$

where m is the mass of a table which includes sliders of the slideway, x is the upward displacement of the table, and f is the outer force.

Next, two time constants are introduced.

$$T_1=\frac{C_2}{K_s},\quad T_2=\frac{C_2}{K_c} \quad (15)$$

Substituting Eq. (15) into Eq. (13) and Laplace-transforming of Eq. (14) gives

$$X(s)=\{\frac{F(s)}{K_s}\}\frac{1}{(\frac{s^2}{\omega_n^2}+\frac{T_1 s+1}{T_2 s+1})}=\{\frac{F(s)}{K_s}\}G(s) \quad (16)$$

where $X(s)$, $F(s)$ are Laplace transform of x, f, respectively, and $\omega_n^2=K_s/m$.

$G(s)$ is a transfer function which shows the vibration characteristics of the slideway. From Eq. (16) it is represented as

$$G(s)=\frac{(T_2 s+1)\omega_n^2}{(T_2 s+1)s^2+(T_1 s+1)\omega_n^2} \quad (17)$$

4. Frequency response of an air-lubricated slideway

A frequency response of an air-lubricated slideway for an ultra precision machine tool is calculated.

The supply pressure and the recess pressure are $P_s/P_a=6$ and $P_r/P_s=0.75$, respectively. Therefoe, $b_2-b_1=3$, $a_2-a_1=3$ (from Fig. 2), and $\rho=5.42$ kg/m^3 are used. The flow rate, volumes of the clearance and recesses are $Q=2.33$ kg/s, $v_c=3.98\times10^{-6}$ m^3, $v_r=9.42\times10^{-8}$ m^3, respectively. The ratio of D/B is 3/100.

The static stiffness of the table is $K_s=795$ MN/m, and mass is $m=1500$ kg. These are experimental values.

Thus, the compressible stiffness and the damping coefficient due to squeeze effect at the recess are obtained as $K_c=1064$ MN/m and $C_2=1.267$ MN s/m, respectively.

The time constants and the ratio of the time constant are $T_1=1.59\times10^{-3}$ (S), $T_2=1.19\times10^{-3}$ (S), and $T_1/T_2=1.34$, respectively.

A frequency response of $G(s)$ is shown in Fig. 3. The resonant frequency exists at $\omega/\omega_n=1.08$. The gain is 15.44 dB, and the phase is -90 degree at the resonant frequency. The values show that the damping ratio is 0.085 in the second order vibration system. However, the frequency response is very similar to the frequency response of the second order vibration system. Therefore, it is known that the air-lubricated slideway for ultra precision machine tools have a damping ratio of 0.085.

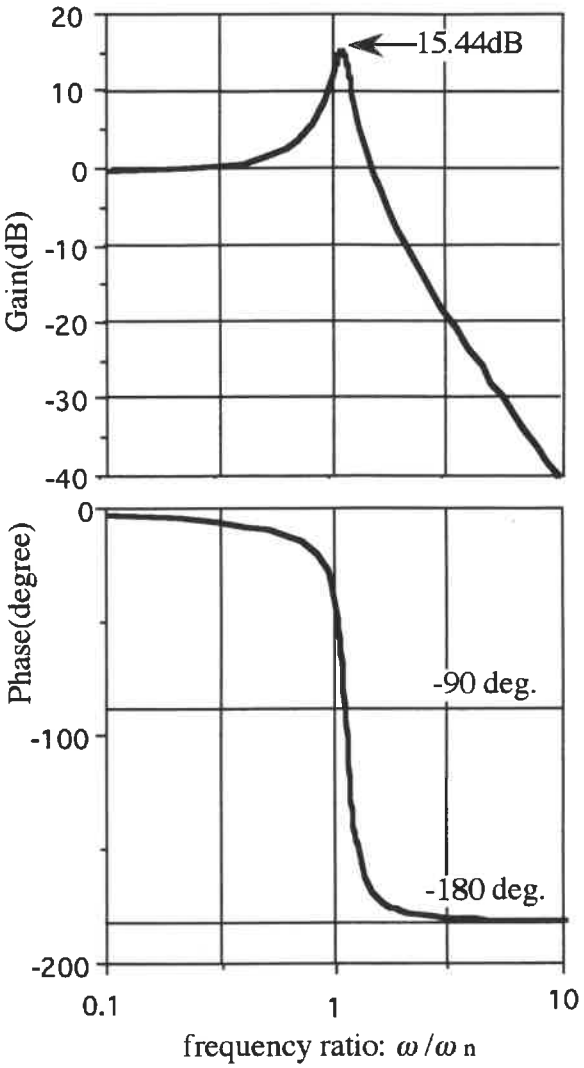

Fig. 3 Frequency response of the slideway

5. Conclusion

The damping force due to the squeeze effect in the case of air-lubricated slideways was analyzed. The results have been applied on a slideway of an ultra precision machine tool. It has been known that the vibration of the air-lubricated slideway is reated as if it were a second order vibration system by its frequency response.

A damping ratio equivalent to 0.085 has been detetmined to be the typical value of the damping force. This value is greater than the damping ratio of an anti-vibration rubber which suspends machine tools, at about 0.05.

Therefore, the air-lubricated slideways provided with orifice restrictors were recognized to be suitable for not only light cutting diamond lathes, but also for hard cutting ultra precision machine tools.

6. Reference

1) Richardson, H.H., Static and Dynamic Characteristics of Compensated gas Bearings. Trans. of ASME, Vol. 80, No. 7 (1958) 1503.

Low Cost, Highly Damped, Precision Linear Guideways Using Porous Carbon Air Bearings and Epoxy Replication

Michael A. Chiu
Massachusetts Institute of Technology, Cambridge, MA

Bradley N. Damazo
National Institute of Standards and Technology, Gaithersburg, MD

Andrew J. Devitt
Devitt Machinery Co., Aston, PA

Alexander H. Slocum
Massachusetts Institute of Technology, Cambridge, MA

Introduction

A high precision linear guideway was developed using porous carbon air bearing pads[1,2] and replication assembly methods. Epoxy replicant was used to reduce the need for expensive precision components by potting the air bearings pads in position. A 'zero-clearance' assembly methodology was used to simplify construction and minimize bearing air gap, which yields the maximum bearing stiffness.

The guideway was built to replace an existing bearing system with the size and mass constrained. This guideway was tested for straightness, static stiffness and dynamic response. The stiffness and straightness results were comparable to those of a conventional orifice air bearing[3]. Dynamic tests also showed that the porous air bearing system was well damped for frequencies below 4 kHz.

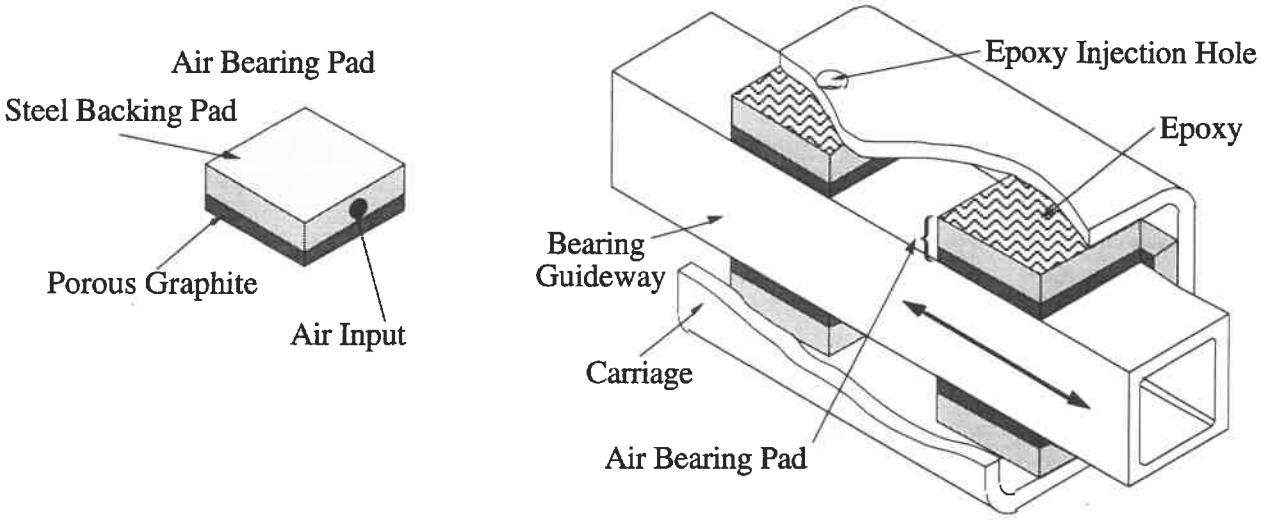

Figure 1. Air Bearing Linear Guideway

Design Description

A high precision linear guide or bushing type bearing was designed to run on a square section, ground and anodized, aluminum bearing guideway. The guideway design required approximately 25 mm of travel and had to support loads of up to 200 N.

The carriage, shown in Figure 1, was designed using 6.5 mm wall welded steel tube and porous air bearing pads. The set of eight pads were constructed of steel backed porous carbon and were fixtured to the carriage using

Diamant™ DWH316[1] replicating epoxy. This epoxy was chosen because of its high stiffness and low shrinkage. Clean, dry air is supplied to the pads through a manifold mounted in the rear of the system. Several larger bearing guideways of similar design were also manufactured. These guideways used larger pads as well as different guideway and carriage materials such as aluminum, alumina and cast iron. Photo 1 at the end of the paper, shows one such system that has 600 mm of travel.

$$k = \beta \frac{P A}{\delta}$$

β = Approximately 1/2
P = Pressure
A = Area of Pad
δ = Airgap

Equation 1. Air Bearing Stiffness

The stiffness k, of a porous air bearing system can be approximated using equation 1, which is derived from fluid dynamics and empirical data. For this design, the pad area was limited to two 40 mm square pads per side with a desired line pressure of 400 kPa (60 lbf/in^2). With these constraints, stiffness can be increased only by reducing the air gap between the bearing pad and guideway. Using four 40 mm pads and 400 kPa air, a bearing with a stiffness of 50 N/µm requires an air gap of approximately 4 µm. A guideway of this precision can be expensive to manufacture using conventional machining and assembly methods.

Manufacturing

The need for precision machining and assembly can be greatly reduced with the use of epoxy potting compounds that are specially formulated for high stiffness and low shrinkage. In addition to the precision ground bearing guideway, the only additional precision machining required is the lapped surface of the porous bearing pads. All other dimensions of the bearing pads and steel carriage can be left 'as machined', with no precision tolerance or surface finish. In fact, roughening the back surface of the bearing pads and inside surface of the carriage can help increase the bond strength of the replicating epoxy.

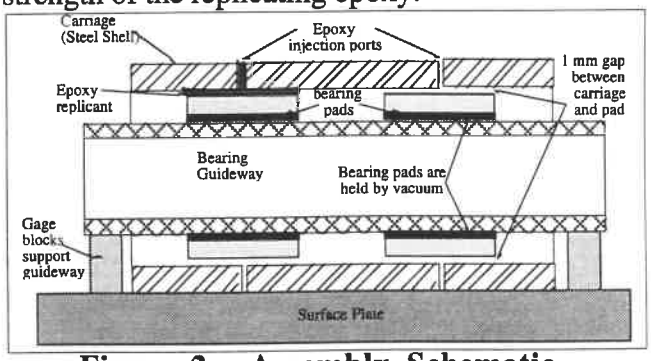

Figure 2. Assembly Schematic

Assembly of the bearing is shown in Figure 2 and proceeds as follows:

1. Bearing pads are plumbed to manifold with flexible tubing. Manifold is then connected to a vacuum source.
2. Pads are positioned on the bearing guideway and held with the vacuum.
3. Bearing guideway with pads are aligned inside carriage using gage blocks. The blocks are sized so that there is approximately 1 mm gap between pad and inside of carriage.
4. Epoxy is injected into pad/carriage gap through a hole in the steel carriage.
5. System is allowed to cure (usually 24h), and vacuum is removed.
6. Manifold is supplied with 400 kPa air; the bearing guideway is now operational.

The bearing manifold simply divides the airflow into four parallel streams, one for each side. Each pair of side bearings are then connected in series. Because the bearing gaps are so small, the pads consume very little air (approx 2 L/min), and the pressure drop between pads in series is negligible.

After assembly, the guideway has zero clearance or air gap, because the pads are in contact with the bearing surface. Theoretically, according to equation 1, a zero air gap will yield infinite stiffness when supplied with pressurized air. However, both the carriage and the bearing guideway have finite stiffness and the supply pressure, distributed over the pad area, will tend to deform them. The resulting deformation creates an air gap between the pad and the guideway, generating a finite bearing stiffness. Because the system relies on the compliance of the structure rather

[1] Product listings are provided throughout this document for the sole purpose of clarifying the discussion, and in no way imply recommendations by NIST.

than precision manufacturing to generate the air gap, the bearings will have the highest stiffness that the structure can support. Stiffer bearings of the same size can only be achieved by using a stiffer support structure. Air gaps of 4 μm were achieved on this system at 400 kPa, which is on the order of the bending deflection of the wall of the steel tube. The small air gaps are a problem only if the bearing guideway has a poor surface finish and/or large geometric errors.

Experiments

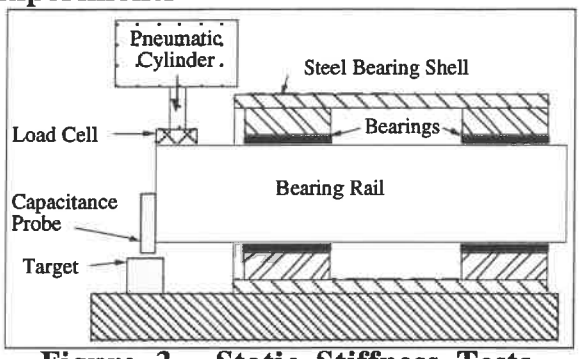

Figure 3. Static Stiffness Tests

The replicated air bearing guideway was tested for stiffness, straightness and dynamic response. All tests were conducted using a similar setup, with the bearing carriage extended and measurements taken at the tip of the extended bearing guideway, as shown in Figure 3.

Stiffness data were collected with the bearing guideway extended 25 mm and a load applied at the tip. The applied force was measured with a load cell and displacement at the endpoint was measured with a capacitance probe. Figure 4 shows the results from a vertical stiffness test. Due to the symmetry of the design, the horizontal tests yielded similar results.

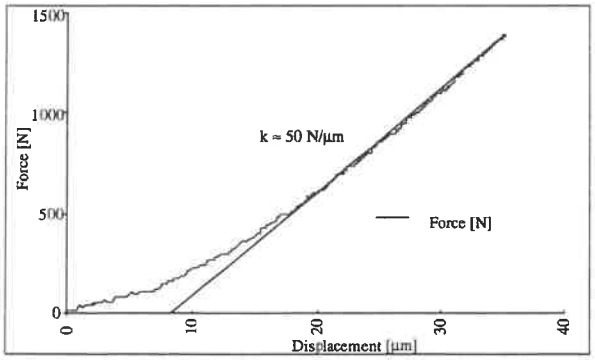

Figure 4. Bearing Stiffness Data

These results show that the air bearing system developed a stiffness of approximately 50 N/μm. The lower stiffness (12 N/μm) in the initial portion of the air bearing curve is due to compliance in the fastening of the bearing to the machine frame.

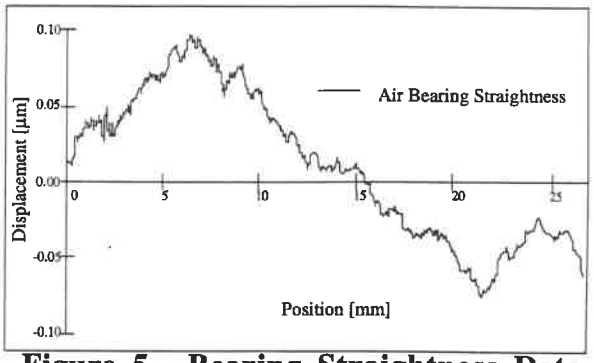

Figure 5. Bearing Straightness Data

Straightness data for the bearing system were collected using the same capacitance probe setup with an aluminized Zerodur optical flat as a target. The bearing guideway was ground flat and parallel to 0.03mm over a 150 mm length and lapped to a 0.4 μm R_a surface finish. The combination of the bearing bushing and guideway yielded a total of 25 mm of travel. Typical results, from a vertical straightness test, are shown in Figure 5.

Total peak to valley error motion of the air bearing was approximately 0.18 μm over the total range of 25 mm of travel. The air bearing pads tended to average out the straightness errors of the bearing guideway.

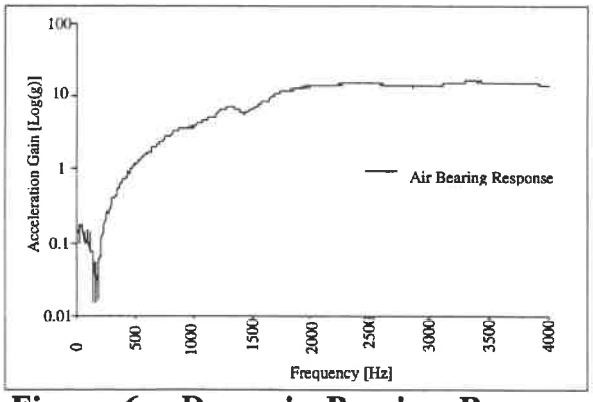

Figure 6. Dynamic Bearing Response

Dynamic response data were collected by using an impulse hammer and a drive point accelerometer located at the same position as the load cell in Figure 3. Several hammers,

accelerometers and frequency ranges were used, all with similar results. Typical results are shown in Figure 6.

The smooth response curve of the air bearing clearly shows that it is extremely well damped. The high damping of the system is likely caused by the very small air gaps (δ). The dominant damping mode in this type of system is squeeze-film damping, which scales with $(1/\delta)^3$. The gain and phase data (not shown) suggests that the guideway can be modeled as a second order system between 0 to 4 kHz with a well damped resonance near 1.5 kHz. Examination of the coherence plot (also not shown) suggests that the feature at 200 Hz is likely due to the positioning of the accelerometer at an anti-node. The superior damping of these bearings means improved accuracy of motion and better controllability.

Additional tests on similar guideways show several other important characteristics. Bearings run at higher pressures did not yield correspondingly higher stiffnesses. This suggests that Equation 1 is not linear with pressure. This is due to the coupling of pressure and gap height. Also, increasing the surface area with the use of full length pads, rather than two discrete pads does not yield a linear increase in bearing stiffness, nor does dynamic response change significantly.

Conclusions

The combination of porous air bearings and epoxy replication with zero-clearance assembly methods has several potential benefits. These include the production of highly damped bearings with good stiffness and straightness properties, as well as reduced manufacturing and assembly costs. Although the test system was designed to accommodate specific size constraints, the basic design can be easily scaled to accommodate larger systems.

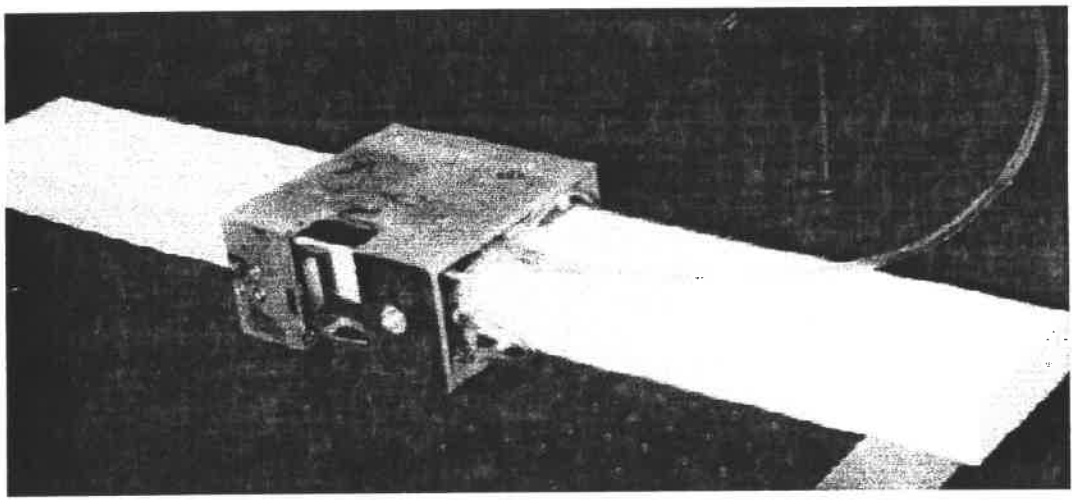

Photo 1. 1 m Bearing Guideway with Instrumentation

Acknowledgment

The authors wish to thank the US. DOE Computational Science Graduate Fellowship program for their support of this research.

References

[1] Rasnick, W. H. et al., "Porous Graphite Air-Bearing Components as Applied to Machine Tools," SME Tech. Report MRR74-02

[2] Devitt, Andrew J. "Development of Porous Air Bearings", Motion Control, May, 1993

[3] Product brochures from Dover Instruments, Westboro, MA

Do Hydrostatic Bearings Generate Mechanical Noise?

David H. Youden
Rank Pneumo, Inc.
P. O. Box 543, Precision Park
Keene, NH 03431-0543

Abstract

Hydrostatic bearings are often used in ultra-precision equipment because of the extreme smoothness of motion which they provide. These bearings exhibit no coulomb friction, and therefore are not subject to the stick-slip phenonema common to other types of bearings. Hydrostatic bearings can be designed to average the imperfections in the guide surfaces used to control the moving element supported by the bearings, thus providing motion which is considerably more accurate than the geometry of the surfaces which comprise the bearings.

Because hydrostatic bearings are active devices, i.e., they rely upon a source of hydraulic fluid at some pressure above ambient, they can serve as a source of mechanical noise in the system which they serve. Much has been written about the importance of quiet hydraulic systems, and how to design them. It is not the writer's intent to relate the litany of hydraulic system design, but rather to examine a typical, high performance hydrostatic slide in an attempt to quantify the noise generated by the hydrostatic bearings and the pumping system.

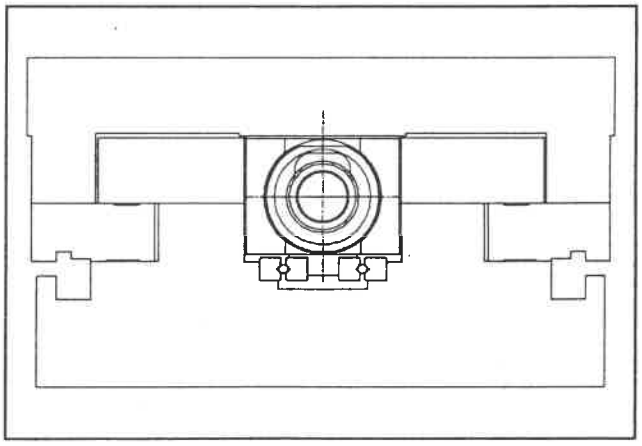

Figure 1: A cross section of the hydrostatic slide used for the noise tests. The actual slide is 381 mm wide.

What mechanisms might contribute to any noise generated by the bearings supporting the test slide? Pulsations in the hydraulic pressure caused by the pump are an obvious example. White noise caused by the fluid flowing in the passageways leading to and from the bearing recesses, in the restrictors, and in the bearing film might contribute to the noise spectrum.

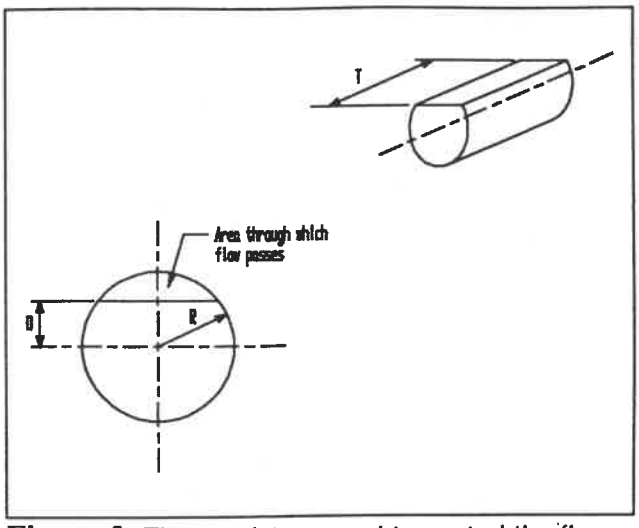

Figure 2: The restrictors used to control the flow in the hydrostatic bearings are laminar flow devices.

The slide that was selected for our tests is the Z axis of a Rank Pneumo Nanoform-600 which has been stripped of all equipment which might generate noise which would confuse our test results. The only systems which were left on the machine in a functioning state were the hydrostatic bearings and the pneumatic isolation and levelling system. Figure 1 illustrates the slide construction. All of the bearings which support, guide, and translate the slide are arrayed in preloaded pairs. The restrictors, which are located directly at the bearing recesses, are laminar flow devices that are manufactured by precisely grinding a flat on a steel pin to produce the geometry shown in figure 2. The equation of flow through this geometry is as shown below:

$$Q=\frac{\Delta P}{12\mu T}\left[\frac{3}{2}D^3\sqrt{R^2-D^2}-\frac{21}{4}R^2D\sqrt{R^2-D^2}+2D\left(\sqrt{R^2-D^2}\right)^3+\left(3R^2SIN^{-1}\frac{\sqrt{R^2-D^2}}{|R|}\right)\left(\frac{R^2}{4}+D^2\right)\right]$$

The hydraulic system on the machine is unusual in that it uses a DC servo motor to drive a small gear pump (.25 cc/rev). The servo motor's speed is controlled by the signal from a pressure transducer so that the output pressure is held constant, even if the flow through the bearings changes because of changing loads. There are no accumulators or other noise control devices in the hydraulic system. Figure 3 is a diagram of the complete hydraulic system on the test machine.

The hydraulic pump has 44 teeth in each of its gears, and at the time the testing was done, it was running at about 1100 rpm as measured with a tachometer, although this speed varied by a percent or two over the course of the test program. 1100 rpm gives a tooth pass frequency of about 807 Hz. The pump was supplying oil to both of the two slides on the machine. Each slide was therefore using 137.5 cc of oil at 17.6 Kg/cm^2 (250 psi) per minute for a power consumption of just under 4 watts.

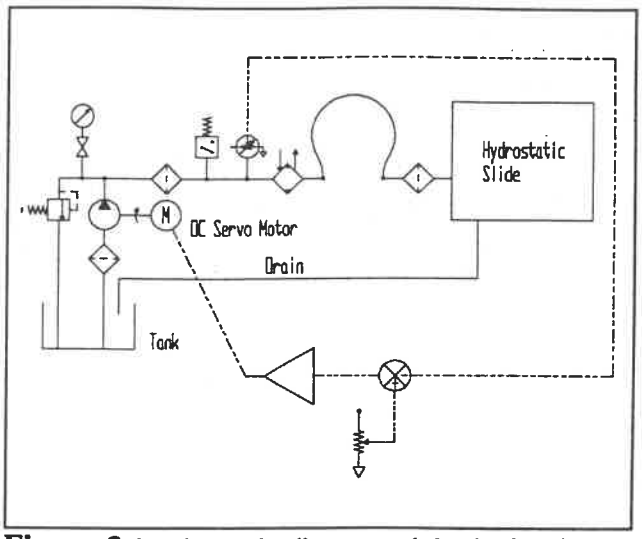

Figure 3:A schematic diagram of the hydraulic power supply used to operate the hydrostatic slide. The relief valve on the left is set to 300 psi. The feedback loop is set to maintain 250 psi.

Testing was done using a Scientific Atlanta model SD-380 signal analyzer. The input signal to the analyzer was generated by a PCB model 393C seismic accelerometer. This accelerometer is designed to measure very low levels of vibration, such as those induced by earth tremors. It has a sensitivity of 1138 mv/g and a frequency range of .01-1200 Hz. The signal from the accelerometer was fed to the analyzer through a PCB model 482A power supply. Pressure measurements were made with a PCB model 112A21/62 dynamic pressure transducer which has a sensitivity of 739 mv-cm^2/Kg.

The signal analyzer was configured to operate in the frequency domain and to double integrate the acceleration signal so as to give a P-V displacement reading vs. frequency. 100 sweeps of the spectrum were exponentially averaged and the

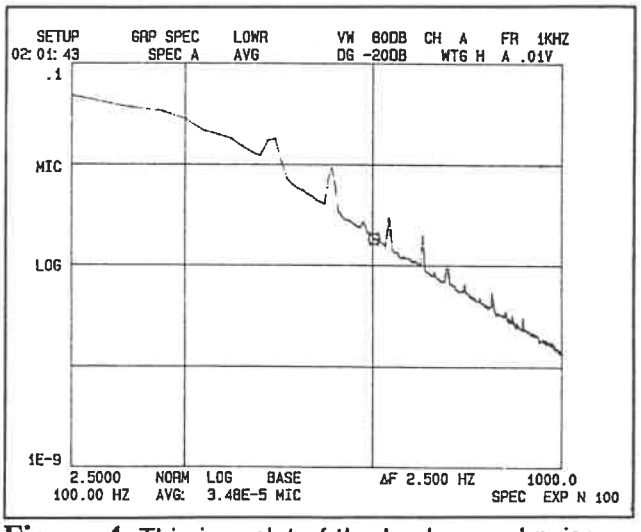

Figure 4: This is a plot of the background noise level. Nothing was running, and the accelerometer was suspended from the base.

results were plotted. Pressure readings averaged and plotted directly.

The air isolation and levelling system under the machine was active during all testing.

Tests were run with the accelerometer mounted vertically on top of the machine's Z axis with the hydrostatic bearings on, and with the bearings turned off. Noise floor measurements were made by suspending the accelerometer from the base with a short length of wire. All testing was done during quiet periods in the laboratory, as even slight disurbances caused spurious results.

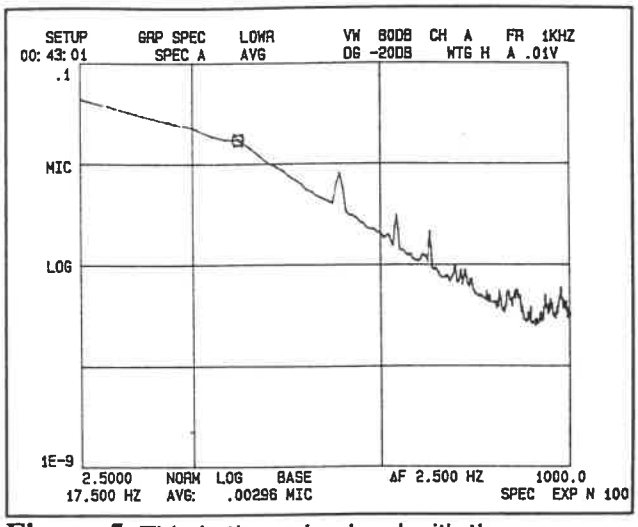

Figure 5: This is the noise level with the accelerometer on top of the slide with the bearings turned off.

Test Results

Figure 4 shows the results obtained with the accelerometer suspended from the base. The minimum detectable acceleration is approximately 2 $\mu m/sec^2$ or $2x10^{-7}$ Gs. At this gain setting, the harmonics of 30 Hz are the most noticeable artifacts on the data.

When the accelerometer is moved to the top of the machine slide, disturbances appear in the regions above 200 Hz. Figure 5 illustrates data taken with the

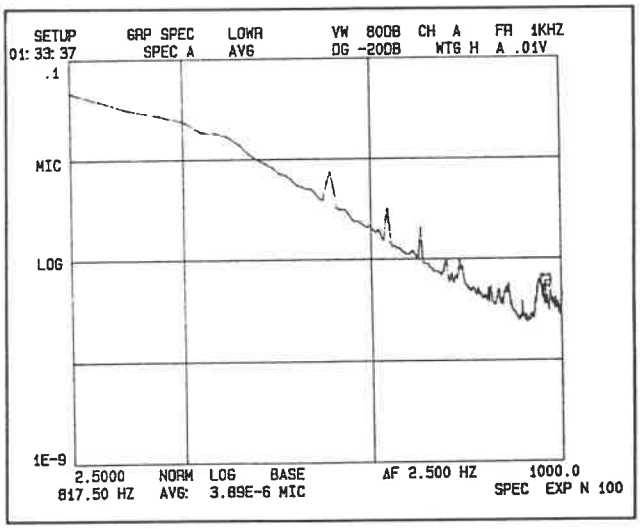

Figure 6: This shows the noise level when the bearings are operating. Note the differences between this trace and the one in figure 5 above 500 Hz.

hydrostatic bearings off and the accelerometer located on top of the machine slide measuring displacement in the vertical direction. The maximum displacement is about $1X10^{-5}$ microns, or 10 picometers.

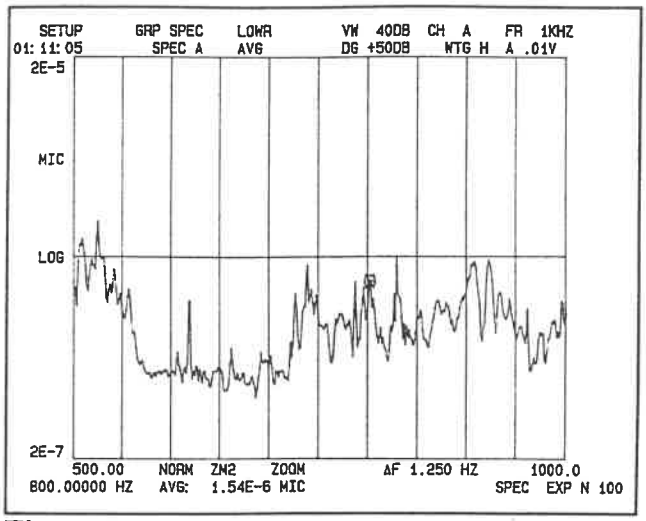

Figure 7: This is an expanded view of the spectrum from 500 Hz to 1000 Hz with the bearings turned off.

Figure 6 shows the changes which take place when the hydraulic pump is turned on. The only detectable changes in the spectrum occur in the region above 500 Hz. The cursor is located on the trace at the frequency of the gear teeth in the hydraulic pump. Careful examination of the trace shows a peak here with a height of just under 4 picometers P-V.

Figures 7 & 8 are expanded views of the region from 675 Hz to 925 Hz showing the differences between the oil off condition and the oil on condition. There is a distinct increase in the vibration in the area around 770 Hz. and the tooth pass frequency is clearly visible. There is a four fold increase in the amplitude at the pass frequency, from 0.7 picometers to 2.8 picometers.

Pressure measurements gave somewhat more interesting results. When the pump was operating there were numerous frequencies where pressure pulsations could be detected. Nearly all of these were below 200 Hz, and most of them were harmonics of the pump rotational speed. The greatest amplitude was found at the pump rotational speed of 18.5 Hz,

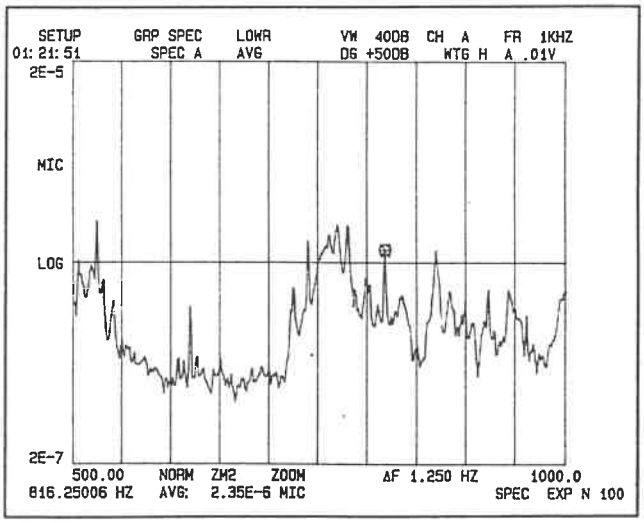

Figure 8: This is the expanded spectrum view with the bearing operating.

where the pressure pulsations were about .0004 Kg/cm^2. Only a slight disturbance, with a P-V amplitude of 1x10^{-6} Kg/cm^2, could be detected at the gear tooth pass frequency. Figures 9 shows the many harmonics of the pump rotational speed, and figure 10 shows the disturbance at the tooth pass frequency. An attempt to obtain a transfer function using the pressure as the input and slide acceleration as the output showed very poor coherence and was abandoned.

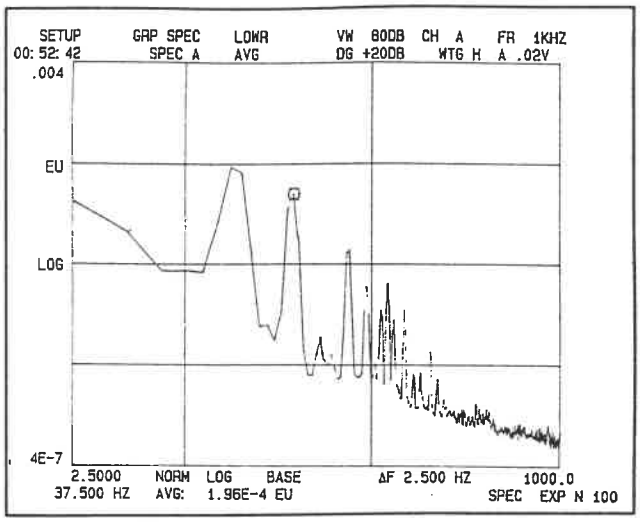

Figure 9: The output of a dynamic pressure tranducer. The units labelled EU are Kg/cm^2.

Conclusions

Although it is clear that the operation of the hydraulic system does contribute to the noise level in the machine, one must wonder whether vibrations with P-V levels in the picometer regime are significant to machines which operate, as the subject test machine does, in the realm of nanometers. While the hydraulic pump certainly generates pressure fluctuations related to its rotational speed, there was little, if any, movement detected at these frequencies. At higher frequencies where some motion was detected, it was several orders of magnitude larger than could be accounted for by the bulk modulus of the oil and the observed pressure variations. Acoustic noise is one potential explanation. Tests were run to determine whether acoustically shielding the hydraulic system

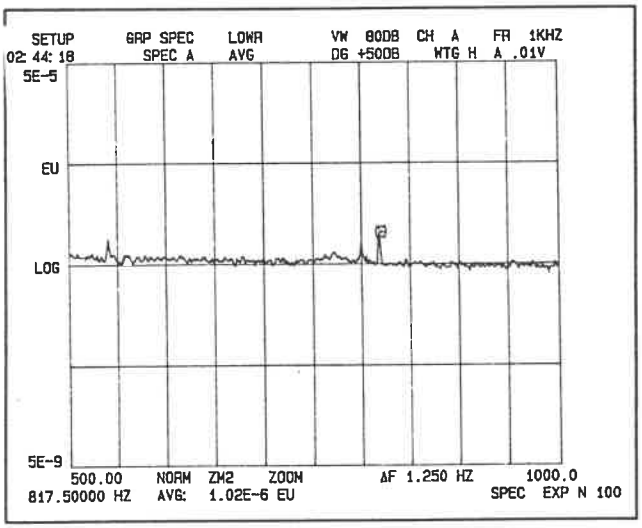

Figure 10: The expanded pressure spectrum showing the disturbance at the tooth pass frequency of the pump. EU=Kg/cm^2.

from the machine made any difference in the vibration. No changes in vibration levels were detected. Shielding the accelerometer from airbourne acoustic vibration did not have a noticeable affect upon the noise levels recorded so, if acoustic vibrations cause some of the noise, they must be transmitted to the machine through the hydraulic hose which carries the oil from the pumping system to the machine base.

Magnetic/Fluid-Bearing Stage for Atomic-Scale Motion Control

David L. Trumper
Mechanical Engineering Department, MIT, Cambridge, MA

Michael Holmes, Roxana Behrouzjou, David Batchelder
Precision Engineering Group, UNC-Charlotte, Charlotte, NC

1 Introduction

This extended abstract briefly describes the design, construction, controller implementation, and performance of a magnetically-suspended six-degree-of-freedom precision motion control stage. The suspended platen (3 kg mass) is floated in oil to support its weight and to provide mechanical damping and high-frequency coupling. Twelve electromagnets and six capacitance probes operate through the resulting oil film to exert control forces and to measure the position of the stage, respectively. Our hybrid approach of magnetic and fluid bearings allows the stage to achieve performance not possible with either approach alone. The magnetic/fluid-bearing stage is designed to ultimately achieve 1 angstrom (.004 μin) resolution in a 100 μm cube of accessible travel. The stage has applications in areas such as scanned probe microscopy, fine motion control for X-ray and optical photolithography, diamond tool machining, and probing and analysis of integrated circuit structures.

At the present time, the stage is operational, with travel of 100 μm and noise under one nanometer peak-to-peak. We have used the stage to provide scanning motions for scanned tunnelling microscopy and have imaged nanometer-scale features with good performance.

2 Mechanical Design

Figure 1 shows a cross-section through the center of the stage. In this figure, a 30 cm line is included to indicate the scale. This view shows the platen inside the oil-filled chamber created by the frame. The sample holder is mounted kinematically to the sample holder support column which is bolted to the top of the platen. Three ruby spheres epoxied into pockets in the bottom of the sample holder fit into three corresponding grooves in the sample holder support column. The kinematic mount is pre-loaded with a permanent magnet. The STM head has three support columns. The foot of each support column is a steel sphere. The steel spheres fit into three grooves in the frame forming a kinematic mount. Each groove is formed by two parallel cylinders which are pressed into pockets

located in the frame. The position of the cylinders is such that the STM tip aligns over the center of the sample holder. This kinematic mount is pre-loaded with three springs. With the platen inside the chamber and the top of the frame bolted in place, the chamber is filled with oil such that the oil level is approximately halfway up the sample holder support column. This ensures that all actuators and capacitance probes are operating in oil. The frame is approximately 30x30x20 cm and is fabricated from aluminum. The platen is approximately 17x17x8 cm and is also fabricated from aluminum. The platen is light-weighted and floated in oil to support its weight and to provide mechanical coupling of high frequency vibrations. The oil-filled capacitance probe sensor gaps form squeeze film dampers which provide viscous damping of the platen motions. The light-weighted platen

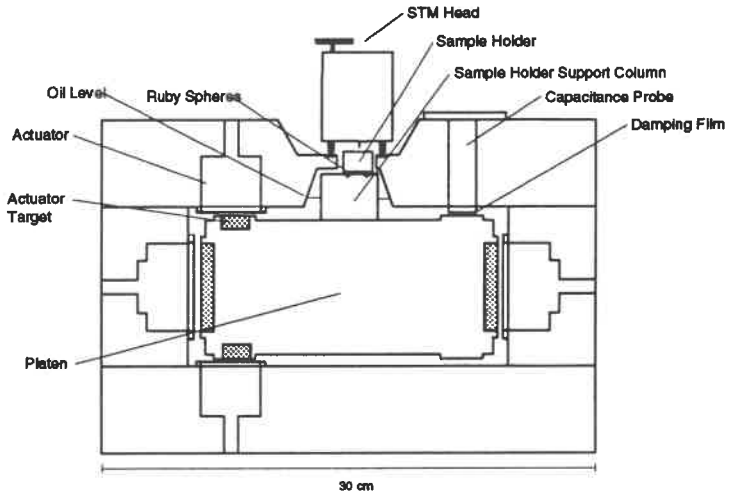

Figure 1: Cross Section of the Oil-Floated Stage

is shown in Figure 2. Each of the triangular pockets is vented to the cylindrical hole in the center of the platen which is vented through the sample holder support column to the atmosphere. The platen's mass is tuned to approximately equal the mass of oil that it displaces. The platen and sample holder assembly has a combined mass of 3.09 kg.

Figure 3 shows a 3 dimensional exploded view of the frame and platen as well as the actuator and sensor designs. Each of the electromagnetic actuators is fabricated with 230 turns of 22 gauge copper wire around 50-50 Ni-Fe E-core laminations. The actuators operate with a gap of 300 μm and are capable of producing in excess of 50 N at this gap, though normal operational forces will be less than 5 N. The electromagnetic actuators are potted directly into rectangular pockets in the frame. Each actuator acts on a corresponding I lamination target which is epoxied opposite the actuator in the platen. The capacitance probes are fabricated from brass and designed for operation in the oil with a nominal standoff of 100 μm and a range of ± 50 μm. The capacitance probes are inserted through cylindrical holes in the frame and bolted to the outer side of the frame. Precision ground aluminum pads on the platen act as the capacitance probe targets.

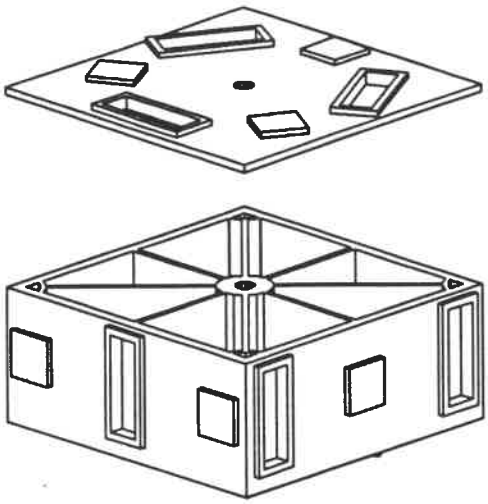

Figure 2: Light-Weighted Platen

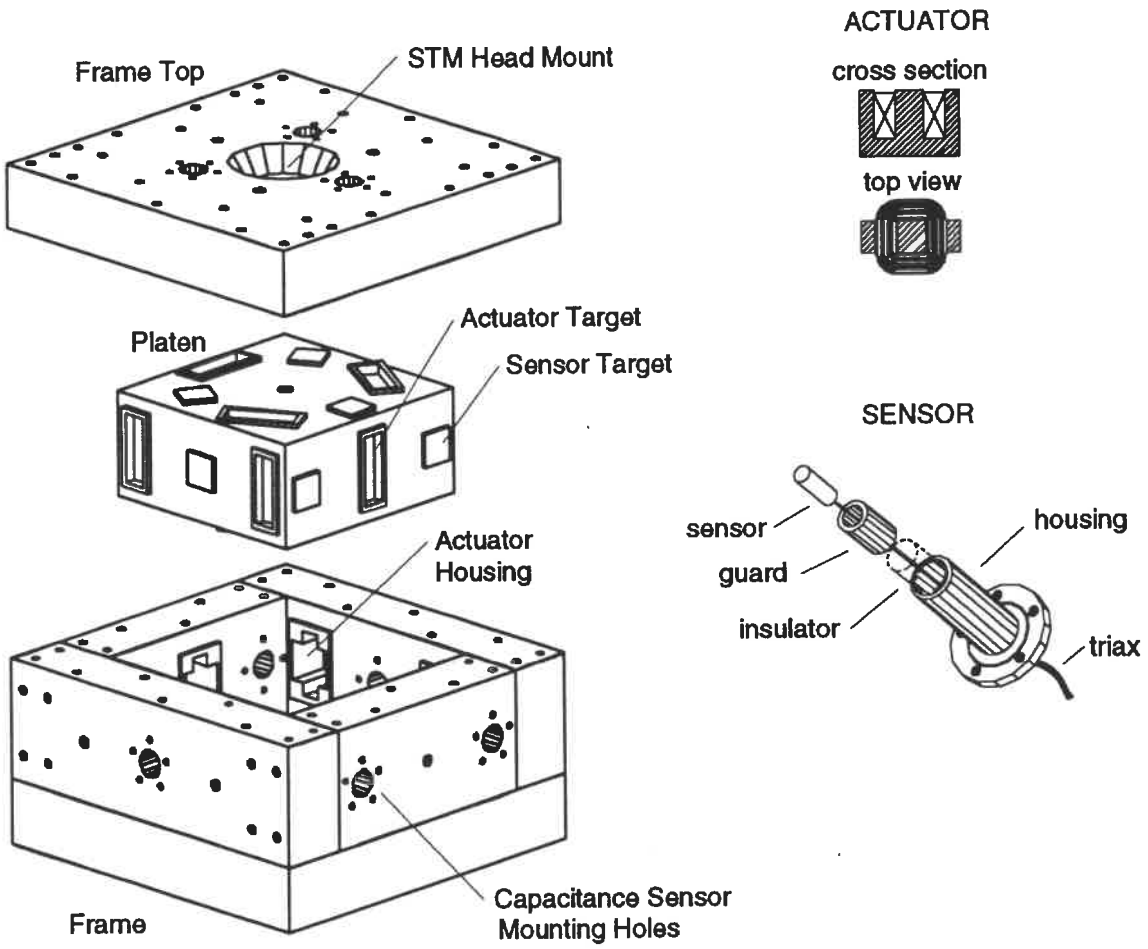

Figure 3: Oil-Floated Stage Exploded View

Figure 4 shows the actuator and sensor orientations. In Figure 4, the capacitance probes, C1-C6, and the actuators, E1-E12 (E8 is opposite E11 and not visible in this view), are contained in the frame which is removed in this view. Once the platen is under suspension, due to the kinematic nature of the capacitance probe sensor sub-system, a nominal capacitance probe gap of 100 μm can be achieved by all of the sensors, representing zero position in all degrees of freedom, regardless of fabrication errors. Any fabrication errors show up in the less critical actuator gaps, which are nominally 300 μm.

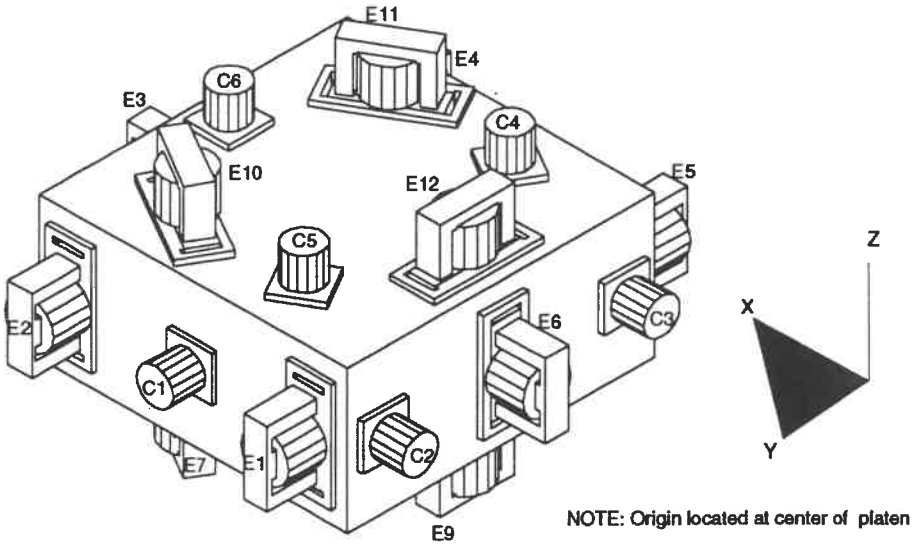

Figure 4: Actuator and Sensor Orientations

3 Controller

The six degree of freedom controller was implemented on a TMS320C30-based DSP. The DSP board resides in a 50 MHz 80486 PC which provides the I/O bus. Also located in the PC's I/O bus are the A/D and D/A boards utilized by the stage controller.

4 Performance

Figure 5 is a scaled trace of the STM Z piezo voltage during a one nanometer step of the platen in the positive Z direction. In order to characterize the lowest possible noise performance of the stage, the viscous damping of the platen motions was increased by pulling the platen into the capacitance probe sensors thereby increasing the squeeze film damping of each damper. This step response was taken with capacitance probe sensor gaps of 55 μm. The rise time is approximately 0.5 seconds which indicates a bandwidth of approximately 1 Hz. The vibration of the platen is approximately 3 angstroms peak-to-peak at this gap.

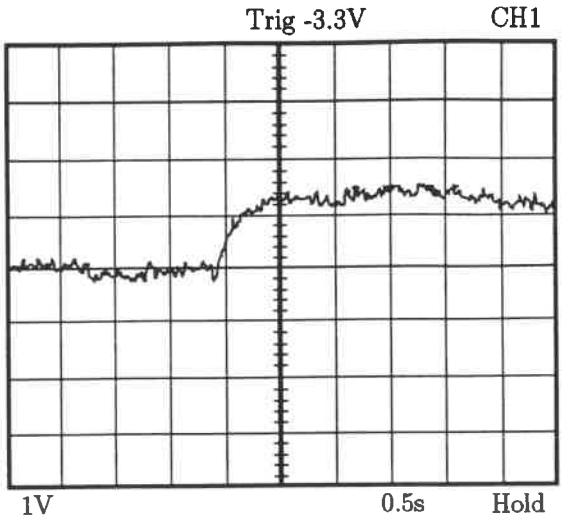

Figure 5: 1 nm Step Response

5 Noise Sources

The present level of stage noise does not allow atomic-scale features to be imaged. However, the present limits to performance are not fundamental; these are dominated by the 16-bit analog-to-digital converter noise and by the finite resolution of the 12-bit digital-to-analog converter which interface the control computer with the stage. The noise level of the capacitance probes is also a limit, but is of less significance at the present time than the converter noise. These noise sources will be corrected in the second pass through the design which is currently in planning.

6 Conclusions

We have designed and constructed a stage which achieves a noise level as low as 0.3 nm. To ultimately reach the level were atomic scale imaging is possible, this noise must be reduced by a factor of three. However, even at the present noise level, this stage offers a promising alternative to piezo-electric-based motion control systems for precision tasks such as scanned probe microscopy.

7 Acknowledgements

This work is based upon research supported by the National Science Foundation under grant DDM-9396305. The ADE Corporation provided design support for the capacitive gauging electronics.

Design Strategies for a Monolithic Micro-Tilt Face-Plate Piezo Flexure Stage

H Mizuno[1] and A E Gee[2]

1 NSK Ltd., Fujisawa, Kanagawa, Japan (on leave at 2, 1990-1993)
2 School of Industrial and Manufacturing Science, Cranfield University, Cranfield, Bedford, UK

1. Introduction

In the precision engineering field, ultra-precision positioning techniques have an important role. Such techniques have been extended from single axis rectilinear positioning to multi-axis positioning for rising demands, such as a fine motion stage for positioning wafers [1], a controlled rotating head micro-tilt stage for single-point diamond turning [2], and a stiff three-point supported structure, for grinding [3]. This paper addresses design strategies for a micro-tilt stage guided by leaf springs and activated by three piezo-electric actuators, particularly designed for workpiece-position control in single-point diamond turning.

2. Design criteria

The required specifications for the proposed micro-tilt stage were based on a reasonable travel range with fine resolution:

Travel range	:	8 μm (Axial)	40 arcsec (Tilt)
Resolution	:	10 nm (Axial)	0.05 arcsec(Tilt)
Stiffness	:	200 N/μm	
Resonant frequency	:	2 kHz	

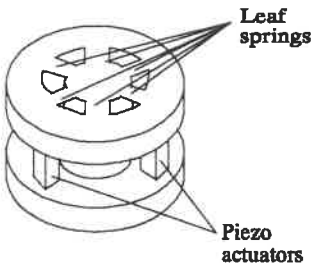

Fig.1 Basic structure of micro-tilt stage

In addition, because the stage is aimed to be controlled under rotation, fast response is desirable and symmetrical structure is preferred to maintain good rotational balance. To satisfy these requirements, a structure, guided by six leaf springs and activated by three piezo-electric actuators as shown in Fig.1, was proposed, which permits fine positioning and stiff structure.

3. Behaviour of the leaf spring structure

In order to analyze the behaviour of the leaf spring structure shown in Fig.1, two kinds of mode were assumed for the deformation of a leaf spring. Fig.2 shows the bending mode, where only one end of a leaf spring is restrained (i.e. single-supported cantilever). The deflection is given by equation (1), the stiffness is given by equation (2), and the maximum deflection is given by equation (3).

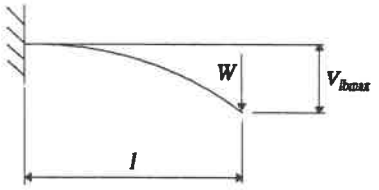

Fig.2 Bending mode of a leaf spring

$$V_{lbmax} = \frac{Wl^3}{3EI} \qquad \left(I = \frac{bh^3}{12}\right) \qquad (1)$$

$$K_{lb} = \frac{W}{V_{max}} = \frac{3EI}{l^3} = \frac{Ebh^3}{4l^3} \qquad (2)$$

$$x_{1bmax} = \frac{2l^2\sigma_{ymax}}{3hE} \tag{3}$$

where v_{lbmax} is maximum deformation, K_{lb} is stiffness, x_{lbmax} is maximum deflection allowed of a leaf spring in bending mode, W is the end load, E is Young's modulus, I is second moment of area, l is length, b is width, and h is thickness of a leaf spring [4].

Fig.3 shows the 'parallel end deflection' mode, where the angles of deflection at both ends are restrained to be zero as in the "built-in" beam. The deflection is given by equation (4), the stiffness by equation (5), and the maximum deflection which is allowed is given by equation (6).

$$v_{1pmax} = \frac{Wl^3}{12EI} \tag{4}$$

$$K_{1p} = \frac{W}{v_{max}} = \frac{12EI}{l^3} = \frac{Ebh^3}{l^3} \tag{5}$$

$$x_{1pmax} = \frac{l^2\sigma_{ymax}}{3hE} \tag{6}$$

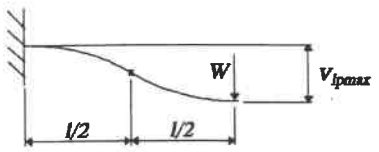

Fig.3 Parallel spring mode of a leaf spring

where v_{lpmax} is maximum deformation, K_{lp} is stiffness, and x_{lpmax} is maximum deflection allowed in parallel spring mode.

Assuming that a pair of leaf springs as shown in Fig.4 works against a force moment around a centre point O as follows:

1) Leaf springs behave in a mixture of parallel end-deflection mode and bending mode. 2) Each mode behaves as one of a pair of springs in parallel, i.e. with cumulative stiffness. 3) The outer ring is assumed to be rigid. Therefore, the angle of deflection at the connection point has to be equal to the tilt-angle of the ring.

Under these assumptions, deflection, stiffness, and maximum deflection of the leaf spring arrangement in mixed mode are as follows:

$$v_{1pb} = \frac{Wl^3}{EI}\left[\frac{-r_1}{2(3l-6r_1)}\right] \tag{7}$$

$$K_{1pb} = \frac{Ebh^3}{l^3}\left(\frac{l-2r_1}{-2r_1}\right) \tag{8}$$

$$x_{1pbmax} = \frac{l^2\sigma_{ymax}}{Eh}\left(\frac{-r_1}{2l-3r_1}\right) \tag{9}$$

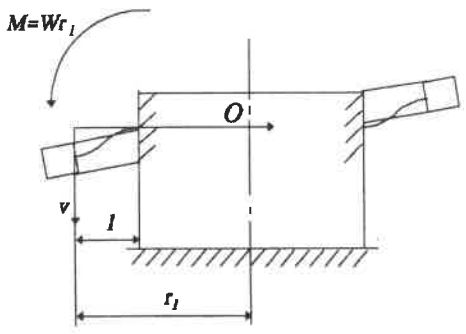

Fig.4 Behaviour of a pair of leaf spring

where v_{lpbmax} is deflection, K_{lbp} is stiffness and x_{lbpmax} is maximum deflection of a leaf spring in mixed mode.

For determining the shape of the leaf springs, where the length l and the width b is restricted by size requirements for the micro-tilt stage, the optimum value of the thickness h has to be chosen. After examining the value to satisfy the travel range and stiffness requirements based on the above equations, h was determined to be 2 mm.

4. Dynamic characteristics of the micro-tilt stage

Fig.5 shows a model of the micro-tilt stage, where three piezo-electric actuators are expressed by springs end of stiffness K_p and damping coeficient c_p, and K_l and c_l show stiffness and damping coefficient of leaf springs, each of them is equivalent for two leaf springs.

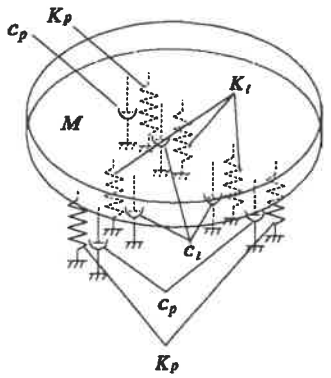

Fig.5 Model of the micro-tilt stage

Fig.6 shows a block diagram of the micro-tilt stage for dynamic analysis, where inputs are voltage signals and outputs are displacements. In the diagram, $\boldsymbol{J}$ is the coordinate transfer matrix, $\boldsymbol{A}$ is the piezo constant matrix, $\boldsymbol{K_p}$ and $\boldsymbol{D_p}$ are stiffness and damping coefficient matrices of the piezo-electric actuators, and $\boldsymbol{L}$ is the matrix showing the dynamic characteristics of the leaf spring structure. Transfer function for the model is given as equation (10).

$$\boldsymbol{J^{-1}}\left[\boldsymbol{I}+\boldsymbol{L}(\boldsymbol{K_p}+\boldsymbol{D_p}s)\right]^{-1}\boldsymbol{L}(\boldsymbol{K_p}+\boldsymbol{D_p}s)\,\boldsymbol{JA}$$

$$= d\begin{bmatrix} \frac{a(s)}{3}+\frac{2b(s)}{3} & \frac{a(s)}{3}-\frac{b(s)}{3} & \frac{a(s)}{3}-\frac{b(s)}{3} \\ \frac{a(s)}{3}-\frac{b(s)}{3} & \frac{a(s)}{3}+\frac{2b(s)}{3} & \frac{a(s)}{3}-\frac{b(s)}{3} \\ \frac{a(s)}{3}-\frac{b(s)}{3} & \frac{a(s)}{3}-\frac{b(s)}{3} & \frac{a(s)}{3}+\frac{2b(s)}{3} \end{bmatrix} \tag{10}$$

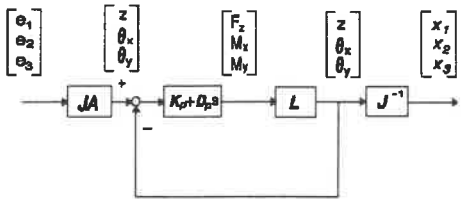

Fig.6 Tilt stage block diagram

where

$$a(s) = \frac{c_{pz}s+K_{pz}}{Ms^2+(c_{pz}+c_{lz})s+K_{pz}+K_{lz}}, \quad b(s) = \frac{c_{pm}s+K_{pm}}{Is^2+(c_{pm}+c_{lm})s+K_{pm}+K_{lm}}$$

In the above equations, $a(s)$ shows the dynamic characteristic in the axial direction and $b(s)$ shows the characteristic in tilt, with subscripts p for piezo actuator, l for leaf spring, z for axial direction and m for tilt. By making $a(s) = b(s)$, i.e. making the dynamic characteristics in the axial and tilt directions equal, the transfer function can be diagonalized, which is beneficial in designing a control system for the stage. Conditions for making $a(s) = b(s)$ are as follows:

$$r_p^2 = \frac{r_l(2r_l-l)}{2} \tag{11}$$

$$I = \frac{1}{2}Mr_p^2 \tag{12}$$

Both static and dynamic cross-interferences between modes are minimized by placing the piezo-electric actuators and the leaf springs at the radial positions r_p and r_l satisfying equation (11), and the mass M and inertia I satisfying equation (12). Resonant frequency in axial direction, f_z, and in tilt, f_m, were examined based on the following equations:

$$f_z = \frac{1}{2\pi}\sqrt{\frac{K_z}{M}} \tag{13}$$

$$f_m = \frac{1}{2\pi}\sqrt{\frac{K_m}{I}} \tag{14}$$

where K_z is the axial stiffness and K_m is the tilt stiffness of the leaf spring structure.

5. Mechanical arrangement and characteristics of the micro-tilt stage

Dimensions of the leaf spring and the moving parts of the micro-tilt stage are determined to satisfy the required specification based on the analyses in previous sections. Fig.7 shows the cross-section view of the stage. The characteristics of the developed tilt stage are the followings:

Travel range	:	8 μm (Axial)	40 arcsec (Tilt)
Resolution	:	10 nm (Axial)	0.05 arcsec(Tilt)
Stiffness	:	196 N/μm (Axial)	77 Nmm/μm (Tilt)
Resonant frequency	:	3 kHz (Axial)	3 kHz (Tilt)

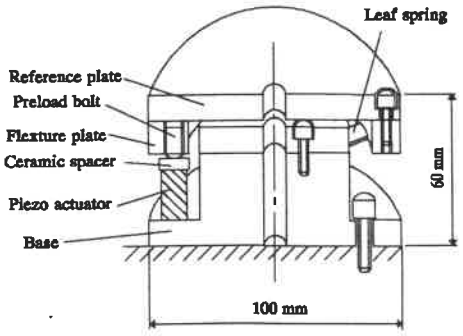

Fig.7 Cross section view of the micro-tilt stage

Fig.8 shows the open loop positioning in (a) axial direction and (b) tilt direction with the micro-tilt stage measured with three optical fibre displacement sensors. The results indicate that the micro-tilt stage is capable of positioning over 8 μm with 10 nm resolution in the axial direction and over 40 arcsec with 0.05 arcsec resolution in tilt. Although hysteresis and cross-coupling between each degree of freedom are seen in the results caused by the differences of the characteristics between three piezo-electric actuators and hysteresis of the actuators, these problems are considerably reduced by closed loop control [2].

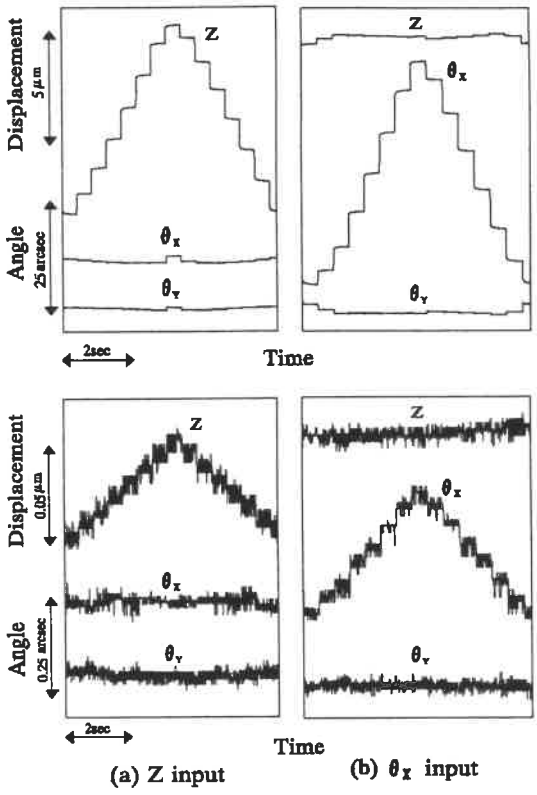

Fig.8 Open loop positioning with the micro-tilt stage

6. Summary

A micro-tilt stage has been designed and developed with the design strategies shown for satisfying the required specification in respect of travel range, resolution, stiffness and resonant frequency. Design effort was also made for minimizing the cross-coupling between each degree of freedom. The performance of the stage has been tested.

7. References

1. N Kikuiri, S Kuwabara and N Uchida, Proc. JSPE Spring Meeting, Tokyo, Mar 1988, pp 943-944
2. H Mizuno and A E Gee, Proc. ASPE, Seattle, USA, 1993.
3. Z-W Zhong and I Nakagawa, Proc. JSPE Autumn Meeting, Sapporo, Oct 1990, pp 617-618
4. J M Gere and S P Timoshenko, Mechanics of Materials, 3rd Ed., Chapman & Hall, London, 1991
5. H Mizuno, PhD thesis, Cranfield University, 1993

3-METER DELAY LINE FOR OPTICAL INTERFEROMETRY IN ASTRONOMY

J.M. Leblanc [1] , M. Sghedoni [1]
Ph. Bourlon [2] , A. Glentzlin [2]
S. Mekid [3], M. Bonis [3]
B. Lhenry [4]

1. INTRODUCTION

Ground-based optical stellar interferometers need optical delay lines in order to equalize the pathlengths from the target star to the beam combiner through telescopes. These delay lines have to maintain nanometer level pathlength accuracy during a coherent integration time of observation. The light of one of the two telescopes is reflected on a moving mirror attached to the delay line, which movement compensates for sideral motion. The movement fluctuations are specified to be significantly less than those induced by atmospheric turbulences (ratio between 5 to 10).

The Aerospatiale Company already developed a first delay line for the CHARON program of "Observatoire de la Côte d'Azur" (OCA, France) around a 1 meter stroke, retail-market translation table [1]. The aim of this second delay line, called LAROCA (Ligne à retard pour l'OCA) was to equip OCA's I2T interferometer. This project offered the opportunity to be a test model for the delay lines of the interferometric systems of the European Southern Observatory (ESO) Very Large Telescope (VLTI).

LAROCA is consequently based on both OCA and VLTI requirements, the main requirements being :

- travel : 3 m extendable to 60 m for VLTI
- tracking speed : 0,2 µm/s to 3 mm/s
- relative positioning accuracy : 10^{-6}
- axial vibrations of the moving mirror in tracking mode : jitter < 12,5 nm RMS for a 15 ms time window
  jitter < 62,5 nm RMS for a 100 ms time window
- operational conditions are atmospheric pressure and temperature range 5 to 15°C

LAROCA was developed under the prime-contractorship of GIE TELAS, (French Organization devoted to hightech products for the astronomy world), in a teaming effort that included the Aerospatiale company for more specifically system studies and control laws, the "Université de Technologie de Compiègne" (UTC) for mechanical design [2], the OCA for realization commissioning, assembly and tests.

1. *AEROSPATIALE, 100 Bd du Midi - 06322 CANNES LA BOCCA CEDEX FRANCE*
2. *CNRS, URA 1361 OCA, BP 229 - 06304 NICE CEDEX 4 FRANCE*
3. *Université de Technologie de Compiègne, Unité Système Mécanique BP 649 60206 COMPIEGNE CEDEX FRANCE*
4. *FRAMATOME, BP 13, 71201 LE CREUSOT CEDEX FRANCE*

2. GENERAL CONFIGURATION

LAROCA's design was driven by the wish to minimize the vibration level applied to moving mirror. The main idea was to mount this mirror onto a carriage guided by low noise bearing devices, in particular in the longitudinal direction, associated with only one force connection for motorization purposes. This was achieved by supporting the carriage with air bearings to obtain zero friction in axial direction. We elected to limit the air bearing guiding stroke to a few millimeters and to achieve the required long stroke by supporting the mirror carriage on a first stage guided by high-precision mechanical devices.

LAROCA's overall configuration is illustrated on Figure 2.1, showing the two-stage superposition concept. The upper carriage is driven relatively to the lower one through the voice coil motor (V/C). This drive system acts like a linear motor at a fraction of the cost, over a long stroke.

Absolute upper carriage position is controlled with regard to the requests coming from the OCA master computer. Position is measured by a high resolution grating linear encoder linked to the upper carriage and moved in front of fixed optical heads. This sensor layout yields the high performance of a one-meter long encoder over a substantially longer, e.g. 60-meter stroke.

Lower carriage position is controlled relatively to the upper carriage through a displacement transducer (Linear Variable Differential Transformer, LVDT), so that upper stage voice coil motor is kept centered.

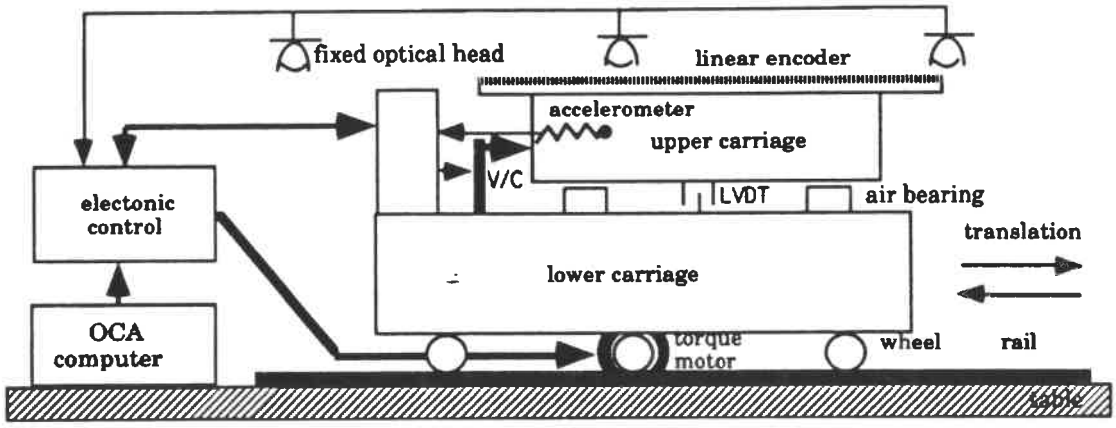

Figure 2.1 - LAROCA General Configuration

3. LOWER CARRIAGE

The framework and lower carriage were built from natural granite for its damping and low thermal expansion properties. The translation was designed to be ensured on circular rails by three wheels on roller bearings allowing high stiffness and low induced noise. Two wheels on one side have V-grooves ensuring lateral stiffness, one of them being motorized.

The opposite wheel is cylindrical, allowing a non-kinematic lateral linkage with very low stiffness and frictions. Wheels and brackets were machined with a Moore machine to achieve high geometrical and roughness precisions.

4. UPPER CARRIAGE

The upper carriage is also manufactured from granite for damping purposes. It is guided on four air bearings installed in a V-shapped design. This guidance design allows high stiffness (40.10^{-6} N/m for one bearing) and damping capacities in lateral directions with zero friction axially. The selected type of air bearings was chosen as of the porous type due to the low noise level ($< 30.10^{-6}$ m/s$^2\sqrt{Hz}$) afforded by that type. For proper working the very thin air gap (3 to 5 µm) requires tremendous geometrical precisions between air bearing planes and opposite faces on upper carriage.

5. CONTROL ARCHITECTURE

For the upper carriage control sensor, we avoided laser metrology for noise measurement, simplicity and cost reasons. Measurement fluctuations coming from air turbulences have to be assimilated to noise, unless stellar beam and metrology beam can be superimposed, which is not the case. The selected linear encoder is a high resolution grating from Heidenhain giving a resolution of 15 nm and a relative accuracy of 10^{-6}.

The upper carriage control loop is shown on Figure 5.1. It consists of two servo control levels. The main loop includes the linear encoder and is compensated with a digital controller. This servo samples at 100 Hz and the closed loop bandwidth is 3 Hz. It is dedicated to position, velocity control and rejection of low-frequency pertubations. The second loop uses the feedback from a piezo accelerometer located on the upper carriage and provides filtering of high-frequency perturbations by a virtual increase of mass carriage (ratio of 6). The accelerometer loop is analogue, its closed-loop bandwidth is about 40 Hz.

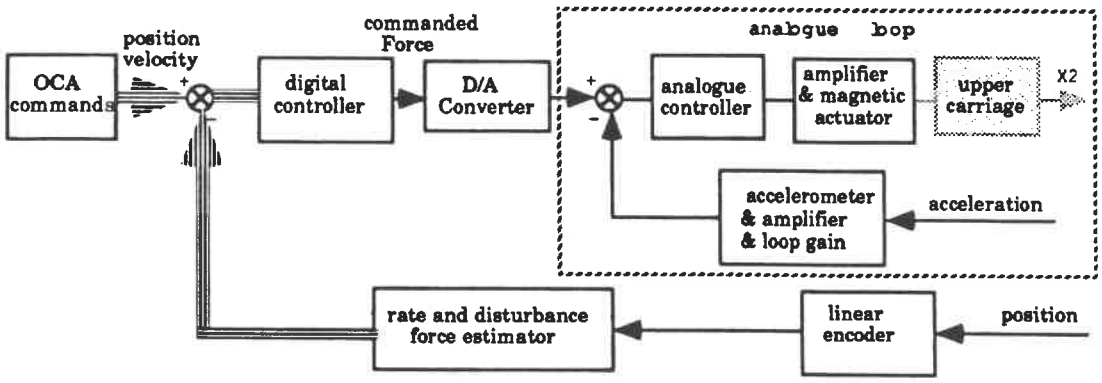

Figure 5.1 - Upper Carriage control loop

The lower carriage control may be less efficient than the upper one, its function is only to keep the voice coiled motor centered. The control loop is shown on Figure 5.2. Sampling and bandwidth are identical to those of the upper stage.

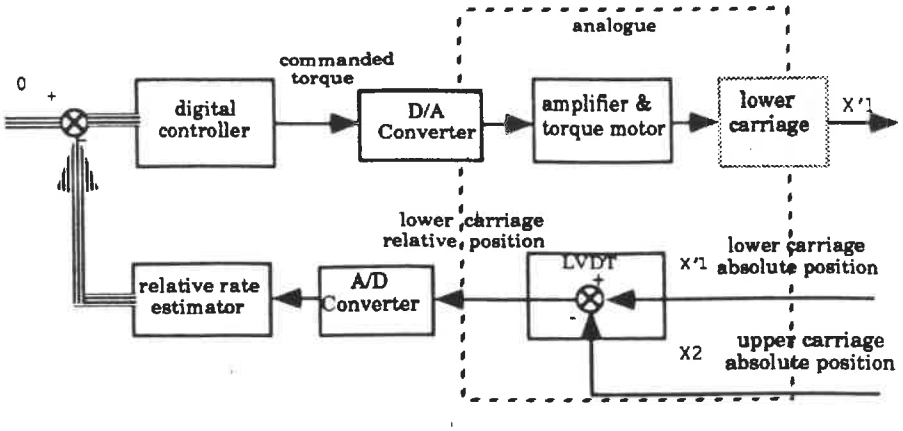

Figure 5.2 - Lower carriage control loop

6. RESULTS

LAROCA was successfully tested in September 1993 and the performance data measured on the 3-meter stroke are perfectly scalable to a longer distance, e.g. the 60-meter stroke to be considered in the VLTI case.

Figure 6.1 shows the performances obtained at maximum speed (3 mm/s) compared to the windowed jitter specification. Figures 6.2 and 6.3 respectively show spectra on longitudinal and lateral directions. LAROCA's performances are compliant with the nanometer level pathlength accuracy required by stellar intereferometry. This has been made possible by engineering team work and by using off-the-shelf commercial devices, sensors, actuators and computer.

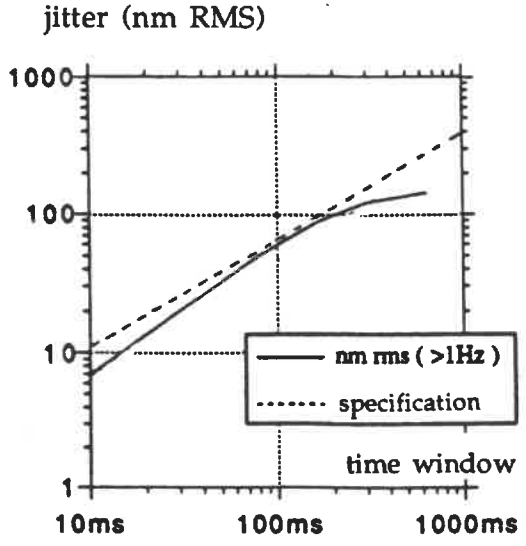

Figure 6.1 - Windowed jitter measurements (3 mm/s)

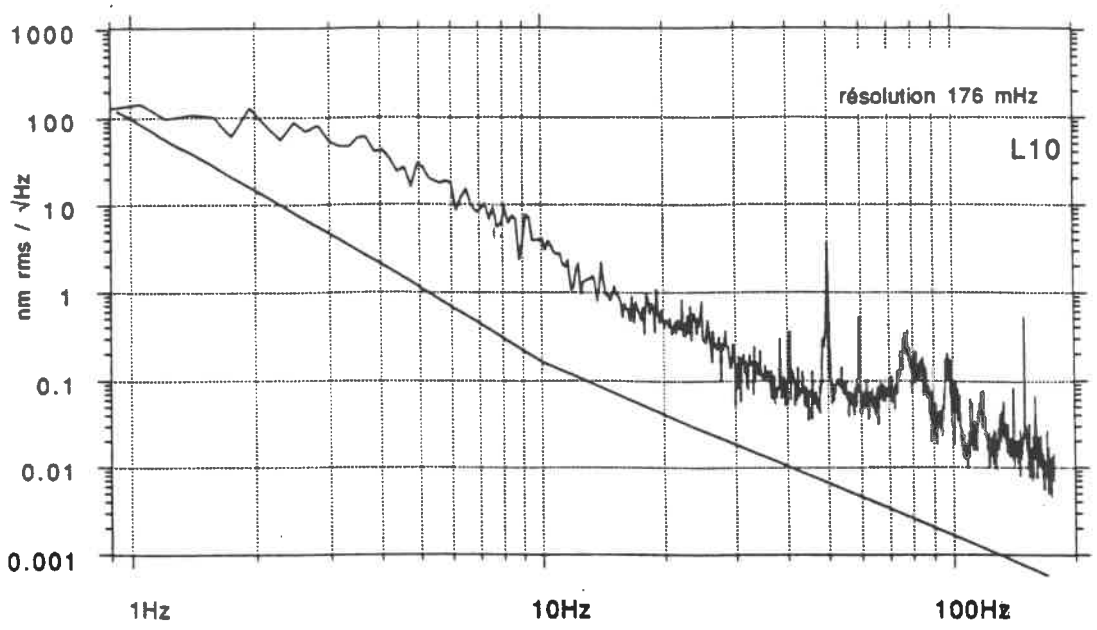

Figure 6.2 - Displacement spectra on longitudinal axis (3 mm/s)

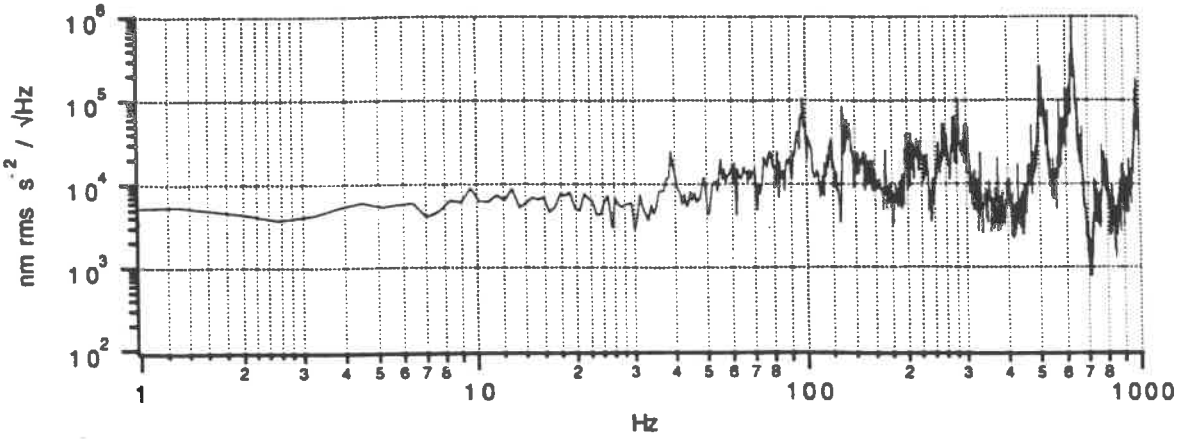

Figure 6.3 - Acceleration spectra on lateral (vertical) axis (3 mm/s)

REFERENCES

[1] B. KOEHLER, E. MANIL - Optical Delay line for stellar interferometer - SPIE Volume 1236, 1990

[2] S. MEKID - Méthodologie de Conception et de Modélisation des Systèmes Mécaniques de Haute Précision - Thèse de Doctorat, UTC 1994

ACKNOWLEDGEMENTS

LAROCA development was co-financed by French Ministry of Research and Education, GIE TELAS, OCA and Institut National des Sciences de l'Univers (CNRS).

Application for patents was filed by TELAS.

The Subtle Causes of *Apparent* Non-Repeatability

Herman Hauschildt
Lawrence Livermore National Laboratory
Livermore, California

SUMMARY

Machine tools are highly deterministic, i.e., they obey cause and effect relationships that are within our ability to understand and control. There is nothing random or probabilistic about their behavior. When apparent non-repeatability occurs in routine machine tool testing, the cause must be sought and identified and possibly dealt with. Four case studies illustrate the humbling but gratifying experience of being a machine tool error detective.

INTRODUCTION

Having had enough practical experience to convince myself that machine tools tend to be very deterministic, I become very suspect when apparent non-repeatability occurs during machine testing. There are many instances when the errors that seem non-repeatable have been caused by subtleties which are often uncovered only after some intensive detective work. Aside from real repeatability errors caused by loose joints, backlash (where the lead screw is the displacement measuring device), and control errors, machine tools generally repeat to within twice the resolution, especially when care is taken to eliminate backlash. There are some recent experiences that I have had in testing machinery that have been very enlightening. They are humbling, in that I should have known better, but they are more than likely overlooked in most testing, because the errors are generally small when compared to other machine errors, and are therefore cast off as yet another machine error. This can unfairly assess the accuracy of the machine as worse than it really might be. Here are four examples I would like to share that will serve as arguments for the deterministic approach and offer insights into the subtle causes that will disguise themselves in the cloak of non-repeatability.

Case 1:

An inspection gauge which uses laser interferometers for positioning also has linear variable differential transformers (LVDTs) which act as the references for establishing the HOME position of the machine. The procedure called for moving the machine to the null position of the LVDT, where the independently mounted core is electronically nulled within the field of a separately mounted coil and setting the lasers at minimum dead path and 'zero' at that point. We had experienced errors in terms of drift between the set point and the laser position value when we would return to the HOME set position, i.e. both were at zero at the start and then when we would move away to measure a part and return to the original set point, the laser display would exhibit several counts when the LVDT was brought to null. This drift was unidirectional, and varied in amplitude dependent on the length of time. Interestingly, the error would eventually decrease to nearly zero if it was allowed to sit long enough at this HOME position. The error could amount to several microns on a machine that has a resolution of .01 microns. Certainly repeatability is better than that - what causes such errors? The error had all the symptoms of thermal drift but the environmental temperature is well controlled. The mystery continued.

Solution: The cause was discovered when the long post to hold the iron core for the LVDT was deflected with a small screwdriver during an attempt to ascertain the sensitivity of the LVDT to core centering. When the screwdriver was merely brought into contact with the post, the meter on the amplifier displayed a large shift. When the screwdriver was then temporarily magnetized the influence was even larger.

When the post was manufactured, it was made out of steel probably for strength and the lower coefficient of expansion. It was then copper plated (the reasoning is unclear) so it appeared to be a copper post. Since it was actually steel, and therefore magnetic, it would affect the flux field of the core when sitting in the surrounding LVDT coil. This affected the amplifier reading and when the core was withdrawn, as during machine use, the magnetic property of the core and the null point would change. The varying time of use would relate to varying amounts of drift.

The steel post was replaced by one made of brass and the problem disappeared completely. Drift or apparent non-repeatability was due to a poor choice of material during design. Now the machine exhibits <.02 micron repeatability.

Case 2:

The machine exhibited excellent unidirectional repeatability during the linear displacement test. An error would occur the instant the direction was reversed which varied depending on where the machine was in its travel. Since this machine used optical scale feedback, there should be no apparent backlash. Angular shift due to a loose fit would tend to be unidirectional. Most bothersome was the fact that if the machine was incrementally moved at the least pulse command of 1 micron using the hand pulse generator and a single pulse in the opposite direction (1 micron) was commanded, the machine would move anywhere from 5 to 22 microns, **sometimes in the wrong direction**, Figs. 1,2,3,&4. The error showed up as a long or short movement if a 10 micron command were made. The disturbing fact is that if corrections for straightness of travel or angular motion were to be installed into the controller, the input of the least command of 1 micron would possibly cause a much larger move in the opposite direction.

Solution: The angular motion was tested in the sensitive direction of each of the axes movement and it was negligible. There was a dynamic component from accel/deccel but the error settled out quickly while the displacement remained in the wrong direction. The linear displacement compensation files were accessed and it was noted that there were different values in the bi-directional tables. Interestingly, the difference in values was very close to being exactly the same amount as the movement in the wrong direction at a given location of travel.

The compensation files were removed and all values were reset to zero. The machine now responded beautifully to 1 micron commands, with no error at reversal Figs. 5&6. The decision was made to recomp the machine and make the values at each increment identical for both directions on the compensation table. After all, the scale feedback should not exhibit backlash.

The test was repeated with the new compensation installed and the data revealed two sets of very repeatable displacement, one set for each direction of travel,. There was separation of the two sets on two of the axes that reached 3 microns at the worst point. This reversal error was due to the influence of chip covers and other hardware that affected the structural compliance of the machine. The scale was satisfied for position but the slight angular distortion of the machine and the large Abbe offset from the scale to the tool location made the 3 micron error inevitable.

The decision that had to be made is: which is better, no shift between the two directional data sets ***or*** absolute response at least command inputs. When the ultimate goal is to be able to correct for all the parametric errors in a machine tool by using compensation files, the large movement initiated by a single pulse command, especially in the wrong direction is an unacceptable situation. The error due to reversal on displacement data was only one half that of the smallest error recorded during the pulse response tests made with offset comp files. Therefore, the use of the same compensation value for both directions seems the wisest choice on a machine tool using scales or lasers for positioning feedback.

Case 3:

During a linear displacement test using a laser interferometer, there appeared to be random errors in the repeatability of the start position while doing displacement tests on a machine tool, Fig. 7. There were also fairly large deviations in the data points and there appeared to be large unidirectional repeatability errors. In this case the errors were + and - values. Prior testing on the machine had not revealed errors of this magnitude. The results of the data were contrary to what one would expect if they believed in deterministic theory, Fig. 8.

Solution: The setup being used was chosen for the ease of placing the optical components of the laser system on the machine components with minimal fixturing. The retroreflector was mounted on the table top and the interferometer was mounted in the spindle. The interferometer itself was offset from the spindle centerline by about 50mm because of the mounting adapter. The spindle was locked by the controller and did not turn noticeably by hand when it was checked.

The spindle 'lock' is actually putting the spindle drive into the lowest range and RPM so that it is least likely to turn. However, the servo for the spindle will hunt to maintain the commanded position and, because of the offset of the interferometer, this hunting shows up as a drifting displacement of the linear axis. Since these rotational moves were large enough to be seen when the machine was at rest, it was easy to diagnose the problem and the spindle was further locked in position with a magnetic base. It is interesting to note that this slight rotational movement could be felt by hand once one realized the movement would be very slight, i.e. like slight backlash in the drive gears. The fact is that even this slight movement caused large displacement errors. The magnet worked to hold position.

The problem was partially solved but lesser errors still occurred, Fig. 9. The cause was traced to the fact that the displacement was being tested at the maximum travel speed of the machine and the dynamics of accel/decel were enough to cause minor hardware movement of the interferometer because it was offset from the spindle centerline. It acted as a pendulum and moved in a direction opposite that of the axis acceleration.

The best solution was to re-configure the setup to minimize the influence of spindle rotation and machine acceleration. This was done by moving the retroreflector onto the spindle with its optical axis near spindle centerline. This makes the setup much less sensitive to rotational movement. The interferometer was moved to the opposite side of the table between the laser head and the retroreflector. The benefit of this change was threefold: 1) Insensitive to spindle rotation, 2) Machine dynamic influences were minimized, and 3) Dead path was made smaller at the start position end rather than having to input offset values. This setup complies with the ANSI B5.54 Standard and provides sound rationale. The errors were minimized to within machine resolution expectations, Fig. 10.

Case 4:

During ensuing displacement tests on the machine, there was still a continuous drift of the start point on each successive set of runs, Fig. 11. The drift was unidirectional, and seemed to be ever decreasing as the runs were being made. The general consensus was that these errors were due to machine settling and therefore several warm-up runs prior to the test were needed. While this appeared to solve the problem, it didn't make sense that a machine with ball roller ways would 'settle in.' The drift of three sets of bi-directional runs was 6 microns, Fig. 12. Bi-directional error was <3 microns and drift between two successive runs in the same direction often exceeded the bi-directional error. This was not acceptable behavior considering this was the last of three axes to be tested and errors on the other two axes were much less.

Solution: The configuration of this machine was such that the same laser placement was used for all three axes displacement tests. The air temperature sensor and material sensor were mounted in the work zone on magnetic surfaces that were in good proximity and yet allowed full travels of the axes without interference with cabling, etc. For the two previous tests, the localized environment around the air sensor remained constant, but in this third and final test, the spindle, which was mounted on the moving axis being tested, came close to the air sensor, which was mounted on a tool setting post, and then traveled away during the test. The spindle has an air/oil lubrication system and the exhaust exits at a hole at the bottom of the spindle housing. The exiting air was at 29.44 deg. C and the environmental air was at 22.22 deg. C.

When setting up for the test, the spindle was near the air sensor and it remained there for some time. When the tests began, the spindle moved away from the sensor. It was away from the influence of the warm exhaust air and the sensor was now monitoring the environmental temperature. During the successive runs, the amount of time that the spindle was in proximity of the sensor declined and therefore the temperature changes measured during the test declined. The test results were exhibiting drift that was due to the compensation of the laser for air temperature changes.

When the air sensor was moved away from the area where the spindle traveled, the drift error disappeared and the results were two data sets that practically overlapped with the reversal shown as a well defined bandwidth, Fig. 13.

This very same spindle exhaust air was later determined to have been the cause of a lesser drift error in a previous straightness test, Fig. 14. When the spindle housing was located over the work table top, the heat of the warmer air was absorbed by the table top and the stands holding the straightedge. The stands themselves are thin and respond quickly to thermal inputs of the warmer air. The table top has a much slower thermal constant because of its mass. The table top caused what appeared to be long term thermal drift and the optical stands short term drift. These two drift errors also caused an apparent non-repeatability. In this instance, parking the spindle away from the table, until the test was ready to begin, eliminated the drift problem and the repeatability was excellent.

The conclusion here is simple. Experience is a great teacher, but even with experience there are subtleties that can be forgotten or overlooked. Machine tools tend to repeat extremely well, whether they are making good parts or scrap, they do it repeatedly. When there appears to be inexplicable errors in repeatability we should be prepared to discover the source of the error and not simply wave it off to the machine as an error in accuracy. I hope the examples I have shared will encourage everyone to use a more deterministic approach when testing machinery and to take a skeptical look at apparent non-repeatable data.

This work was performed under the auspices of the U.S. Department of Energy by Lawrence Livermore National Laboratory under contract No. W-7405-Eng.48.

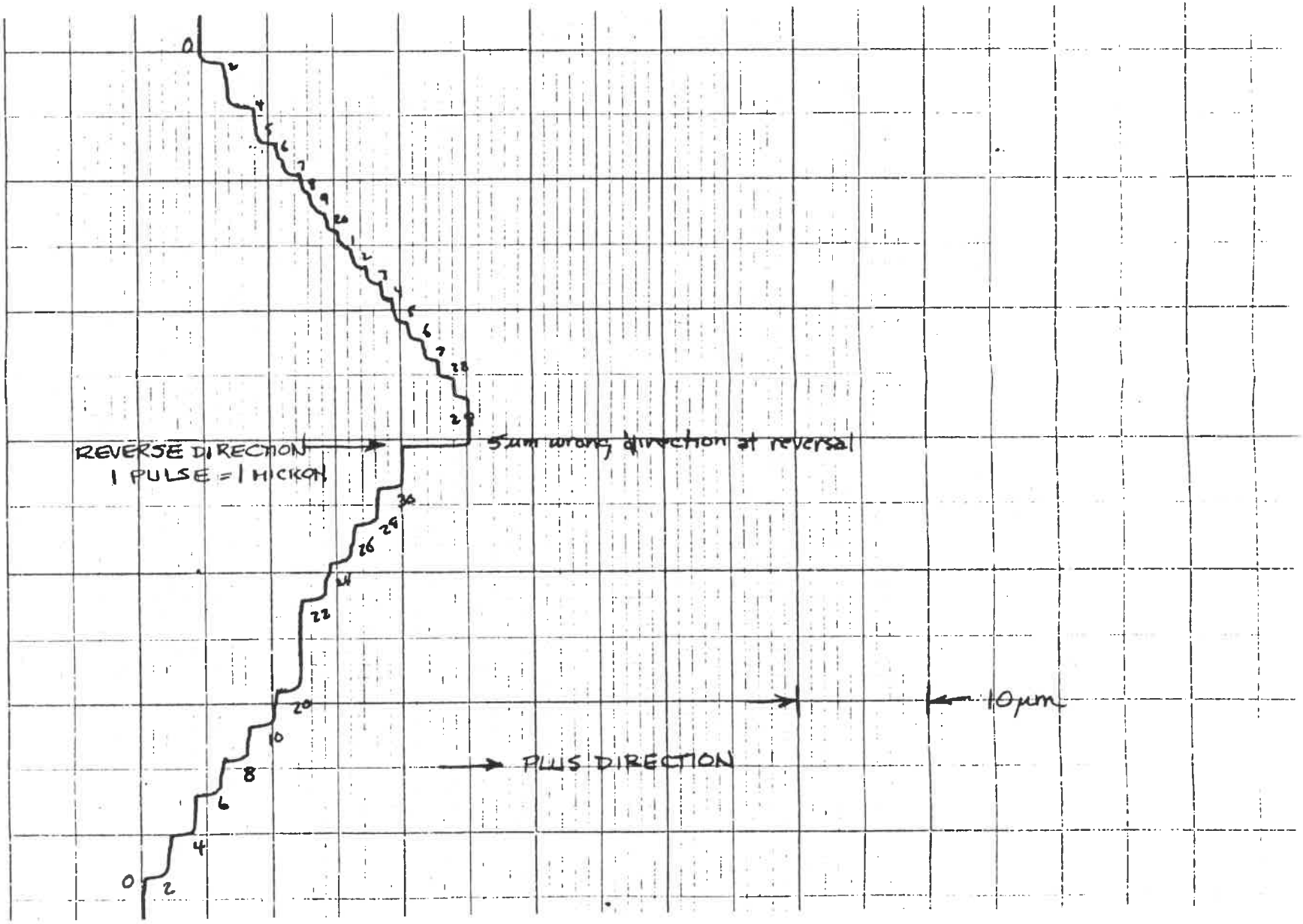

FIG. 1: This chart illustrates machine response to 1 micron pulse commands on the X axis. Note the 5 micron lurch in the wrong direction when the direction is of travel is reversed.

HEWLETT-PACKARD

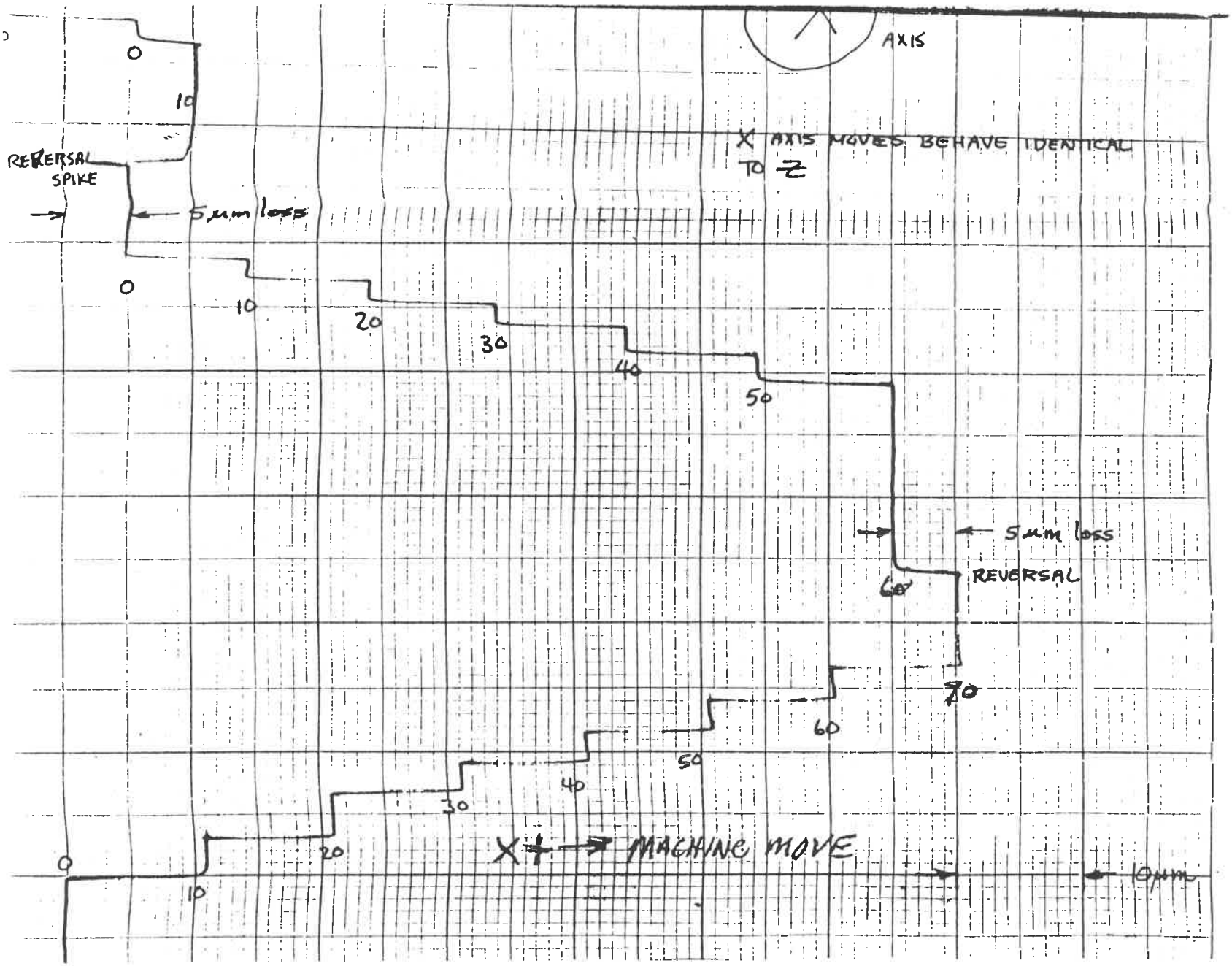

FIG. 2: This chart is the X axis response to 10 micron pulse commands. In this case there appears to be 5 microns of lost motion at reversal.

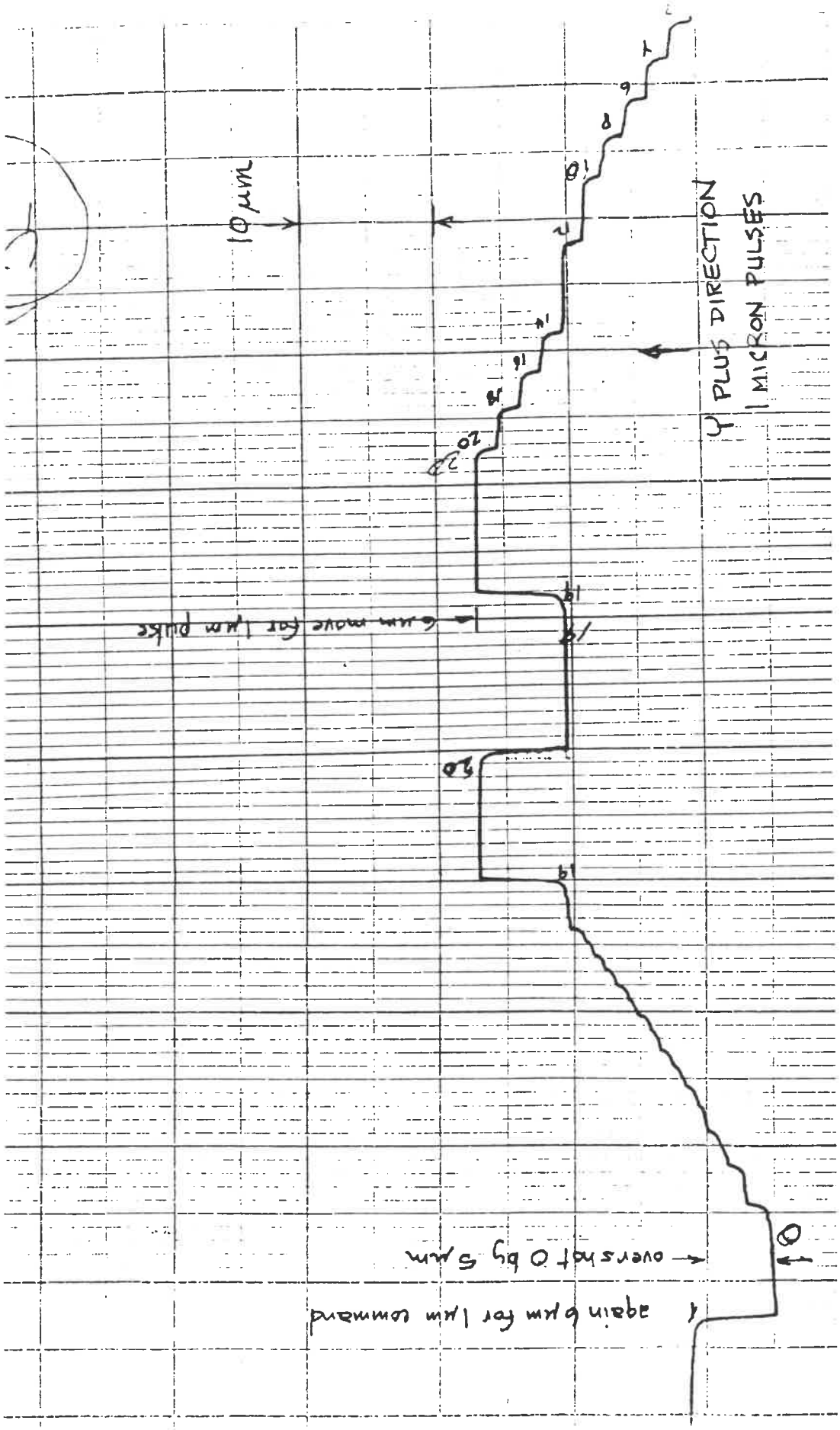

FIG. 3: This chart is of the Y axis response to 1 micron pulse commands. This axis seemed to lurch 6 microns too far when the direction was reversed.

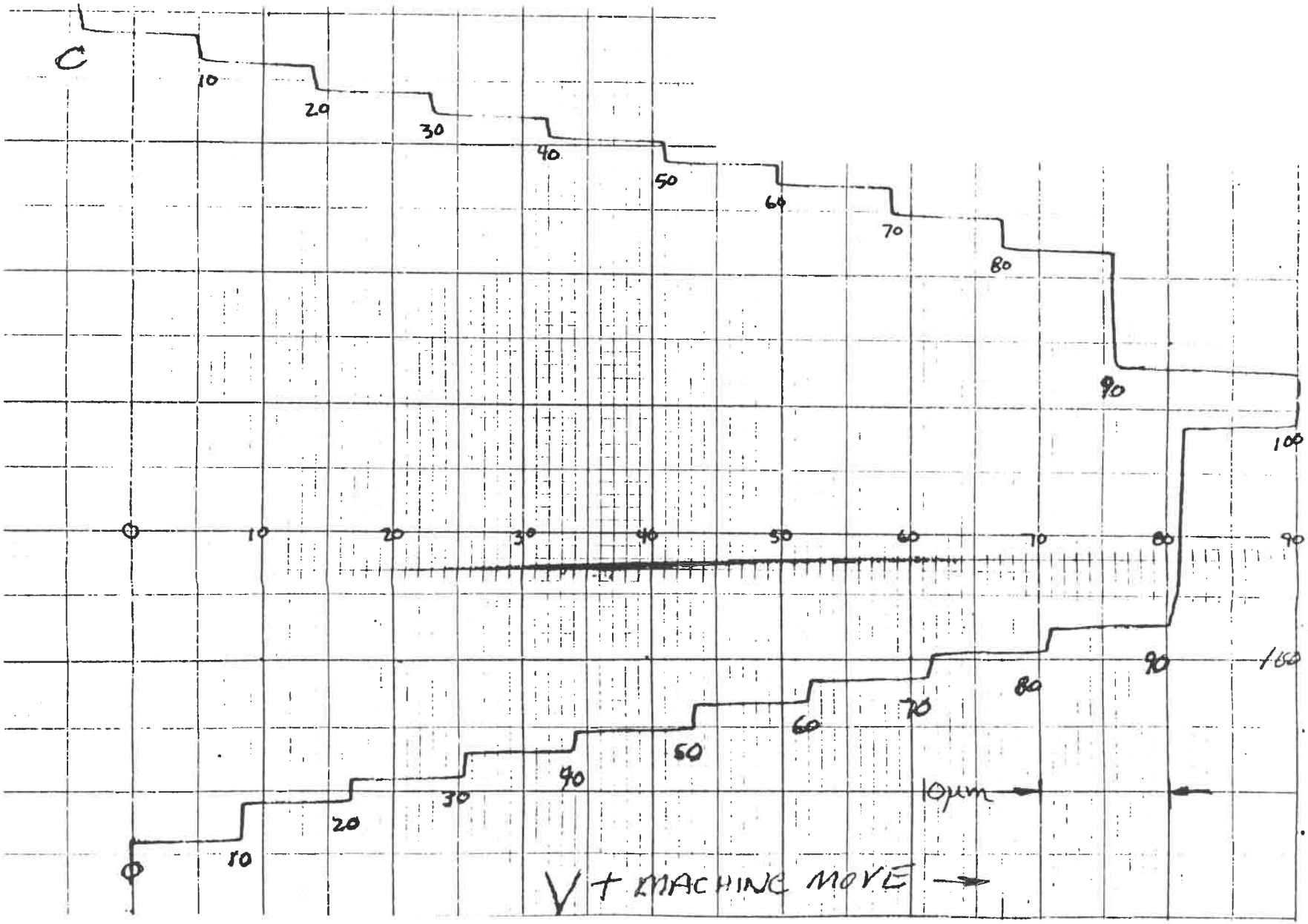

FIG. 4: This chart is the Y axis response to 10 micron pulse commands. In this case the moves is 6 microns too much for the commanded move (16 vs. 10 microns).

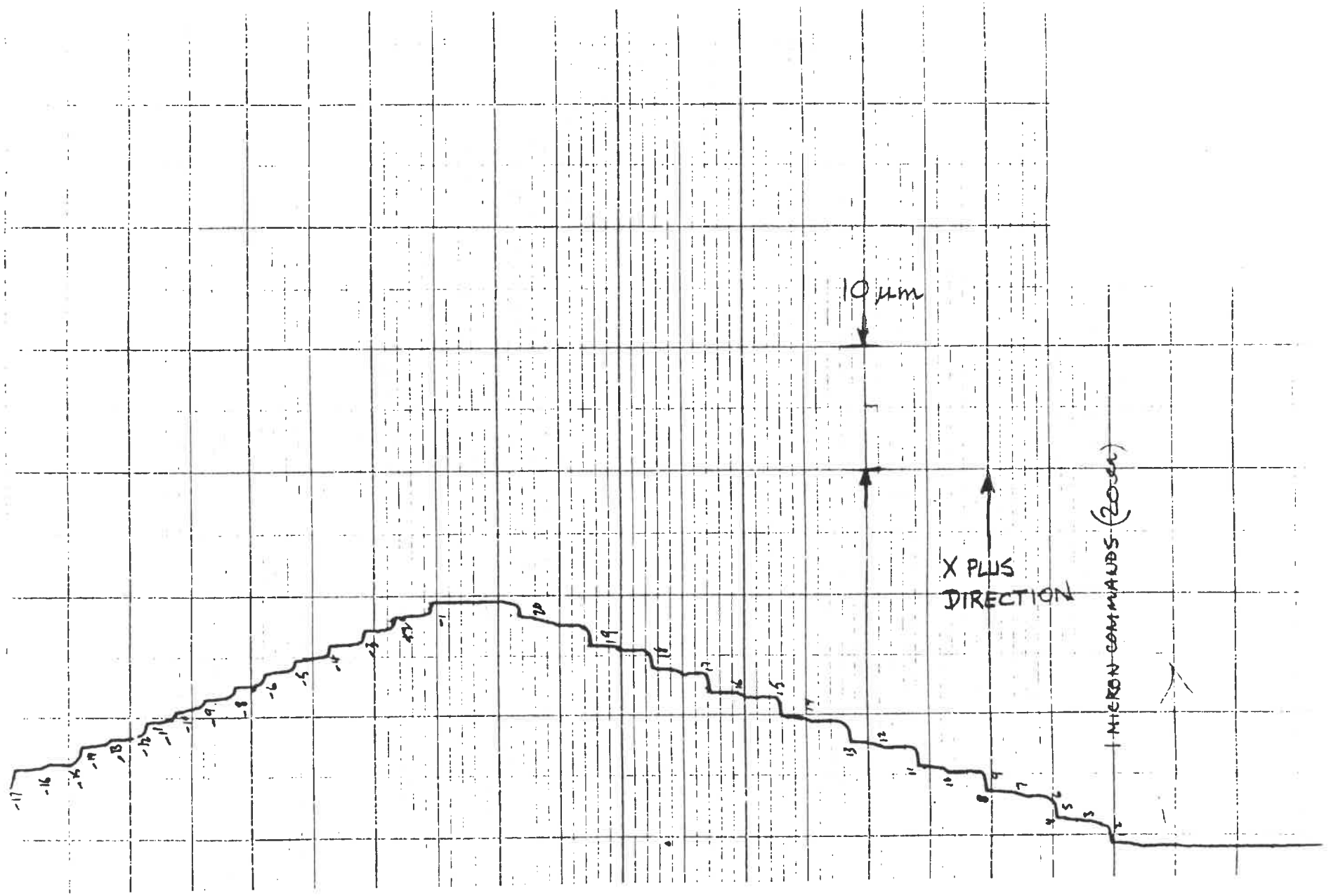

FIG. 5: This chart illustrates the proper X axis response to 1 micron pulse commands and the near perfect response at reversal when the compensation files in both directions were set to the same value.

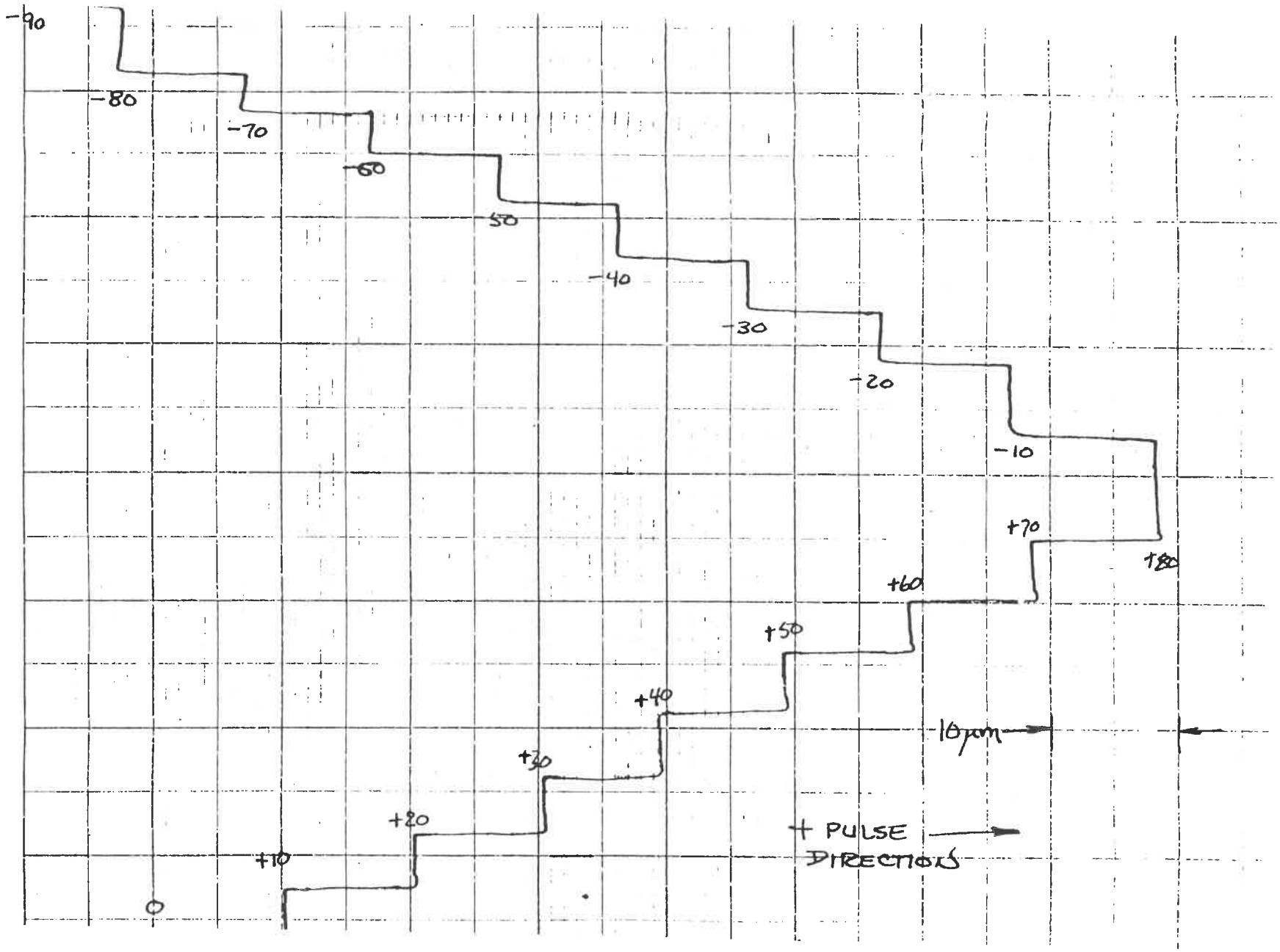

FIG. 6: The X axis response was also better at 10 micron pulse commands although there is a reversal component of about 2 microns not seen on the 1 micron chart. This amount appeared in the final X axis displacement data.

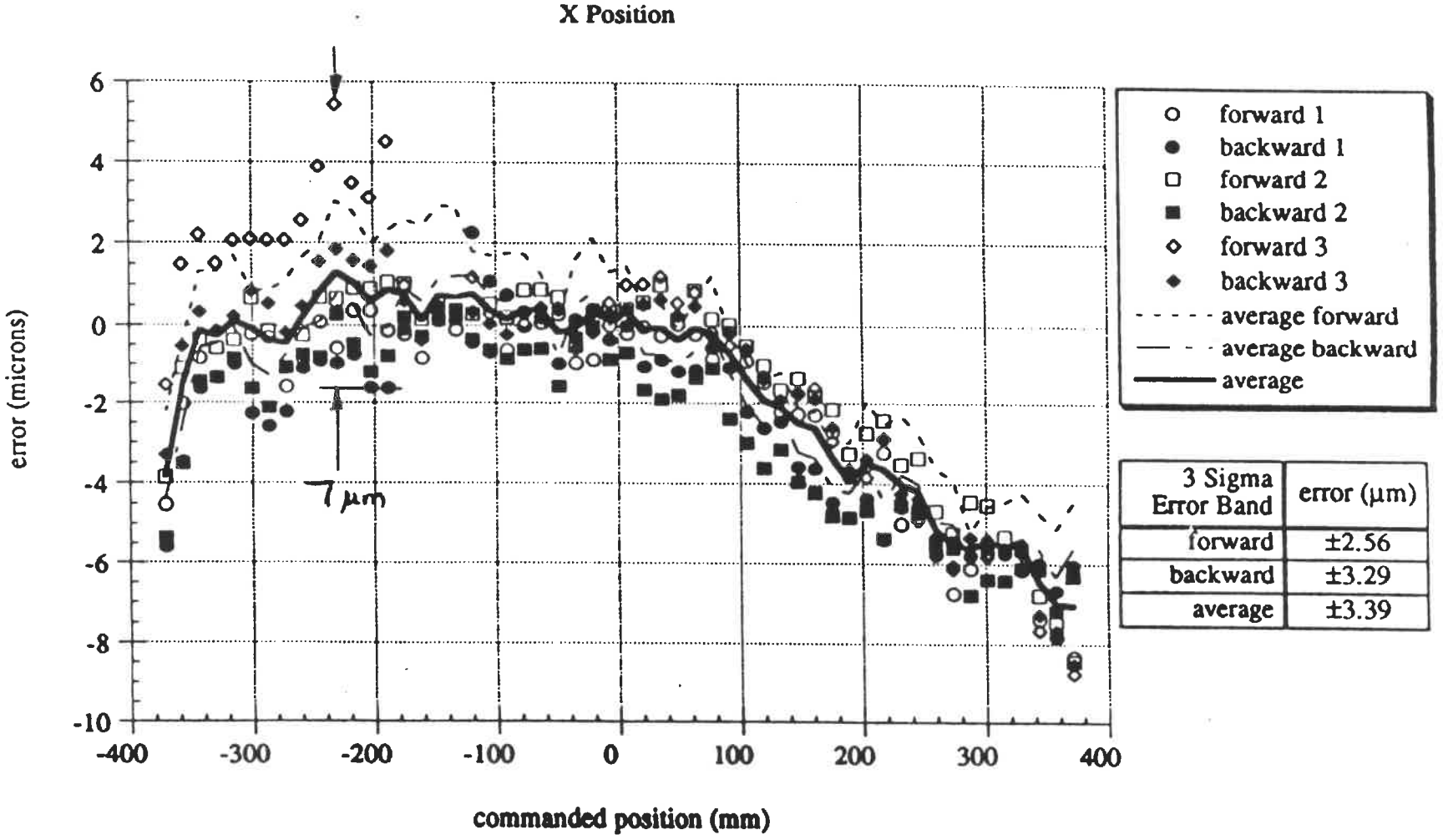

FIG. 7: This in-process chart (best fitted to set zero at machine mid-travels) was full of scattered points that were the cause of investigation into the apparent non-repeatability.

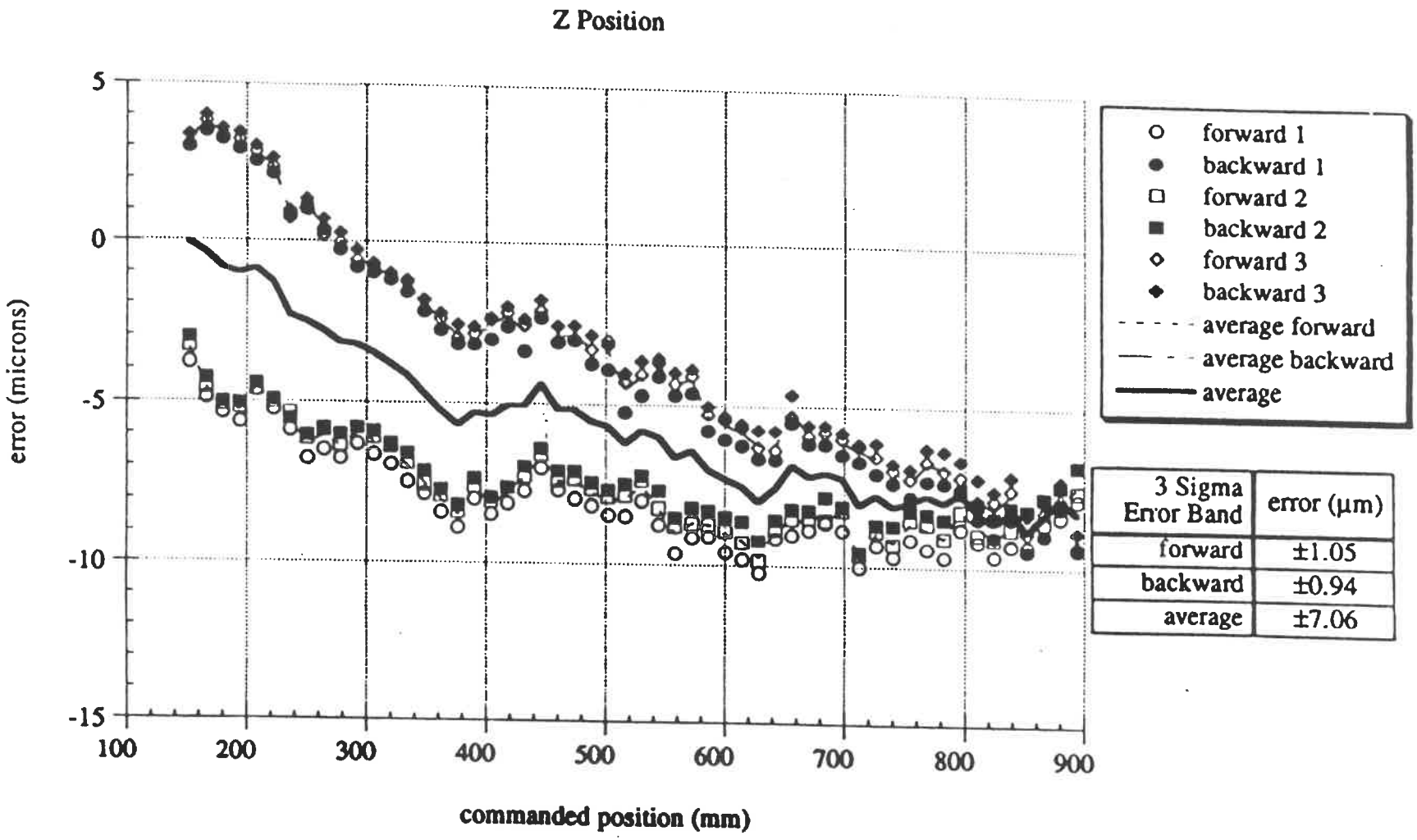

FIG. 8: This chart demonstrates repeatability of another axis , even amid larger errors. Scatter of data is worse when farthest from laser. Incorrect bi-directional compensation caused apparent backlash error.

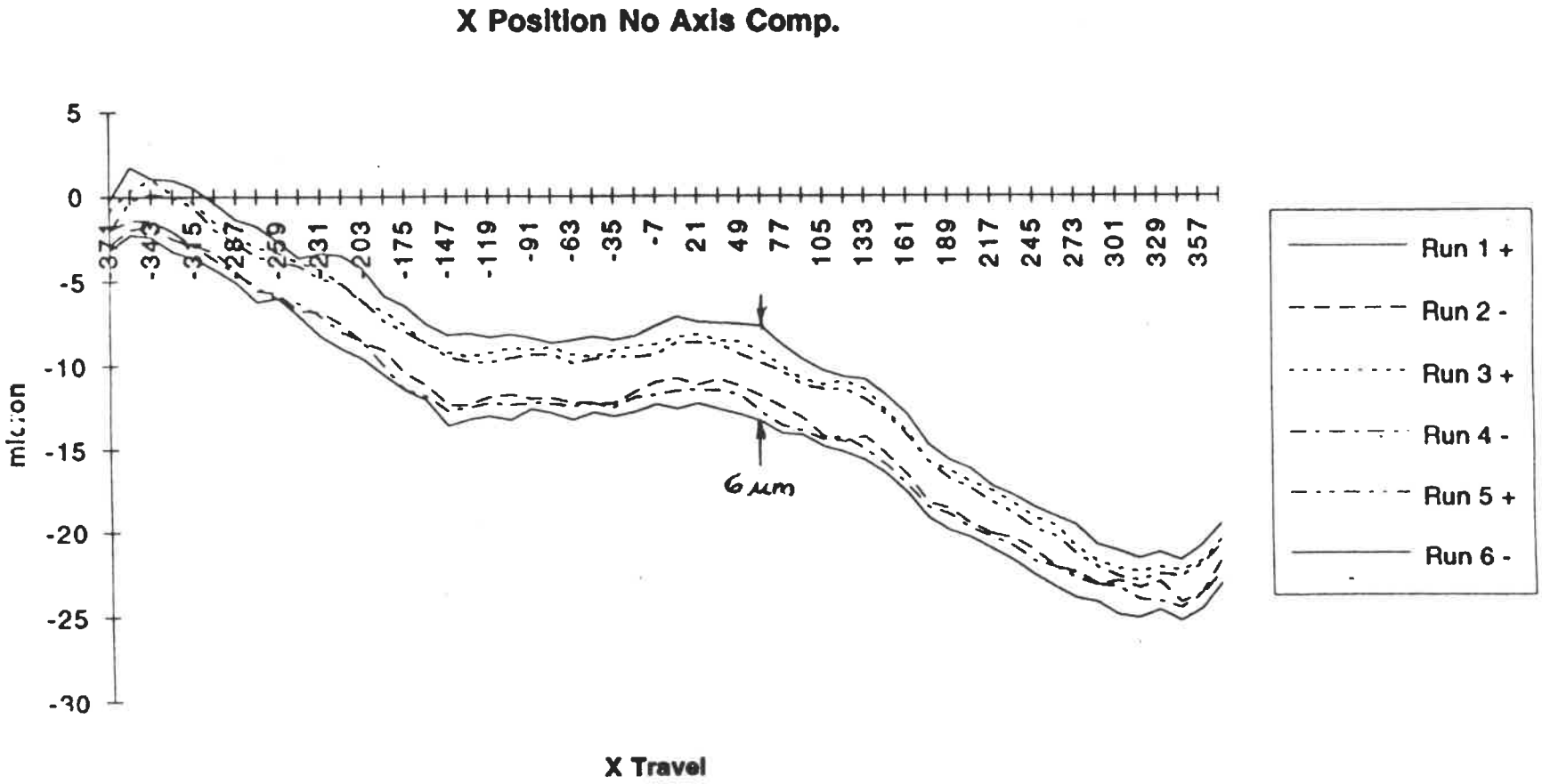

FIG. 9: This was the first chart made of raw data with all of the compensation files removed. Note that Runs 1 & 6 are solid lines bounding data with 6 micron error band.

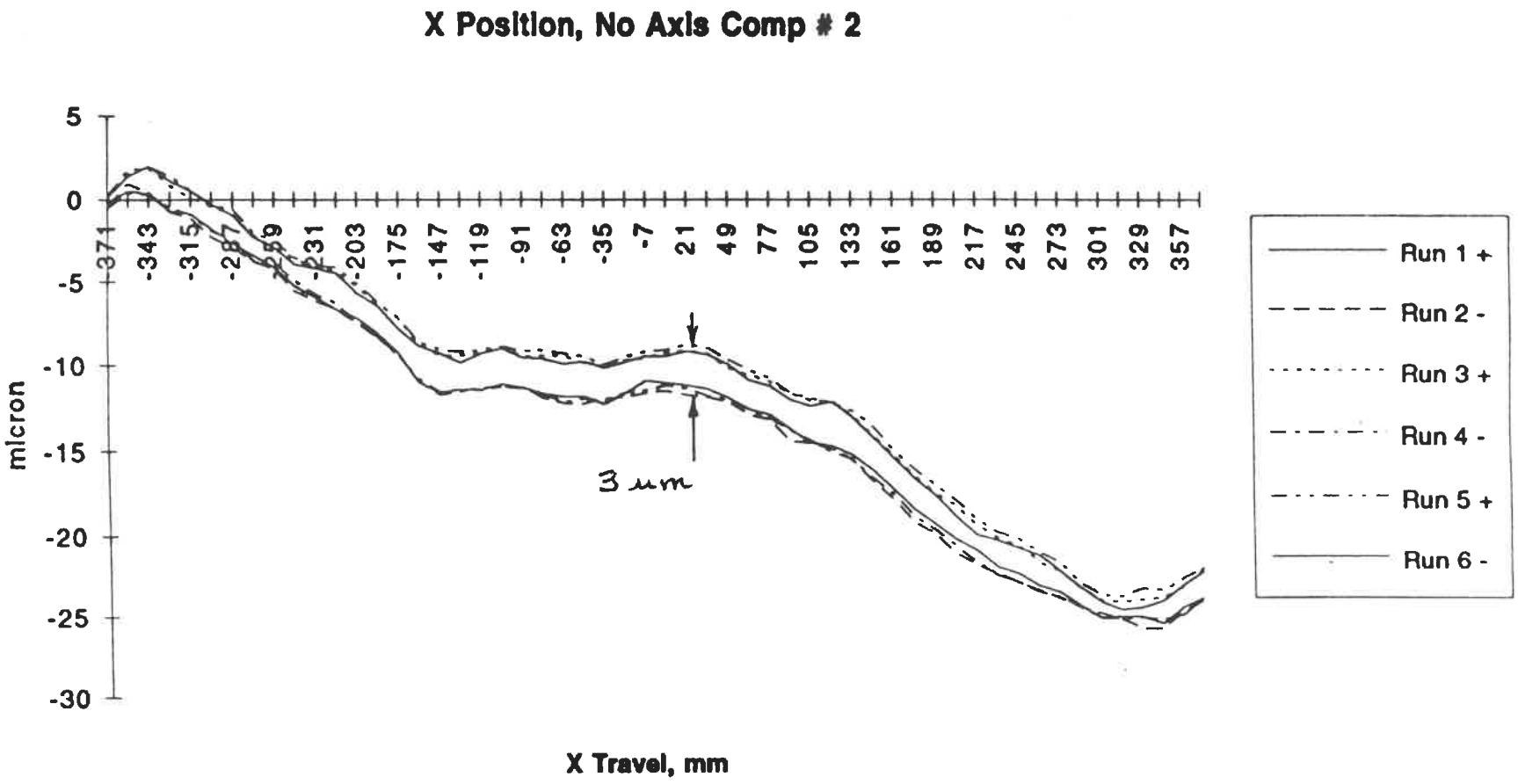

FIG. 10: This chart is of the same tests after all the error sources were addressed. The error band is now 3 microns and same direction runs repeat within resolution.

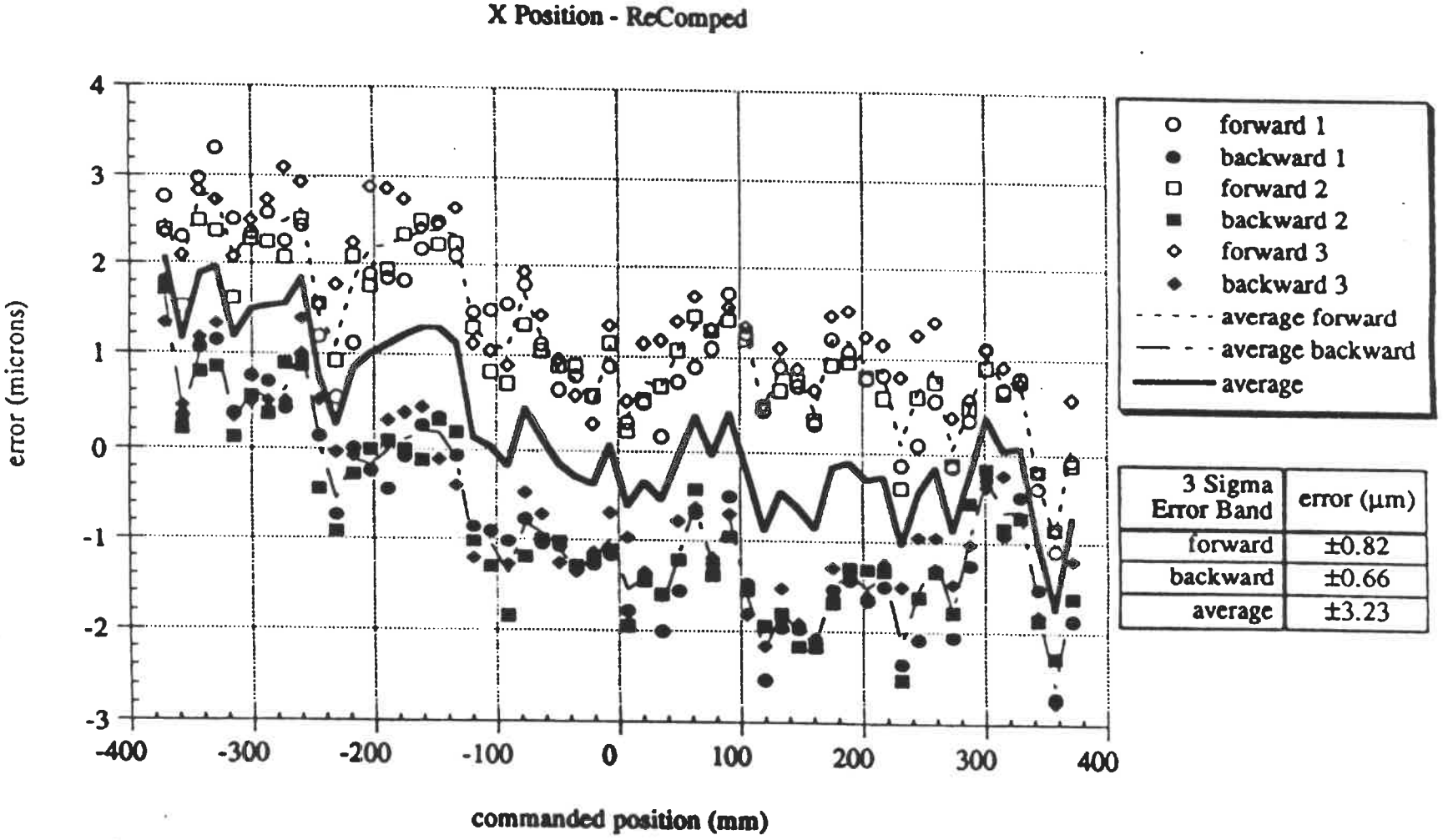

FIG. 11: This chart of compensated data at a finer chart scale still has scatter, but of much less amplitude. The major error is the 3 micron reversal error.

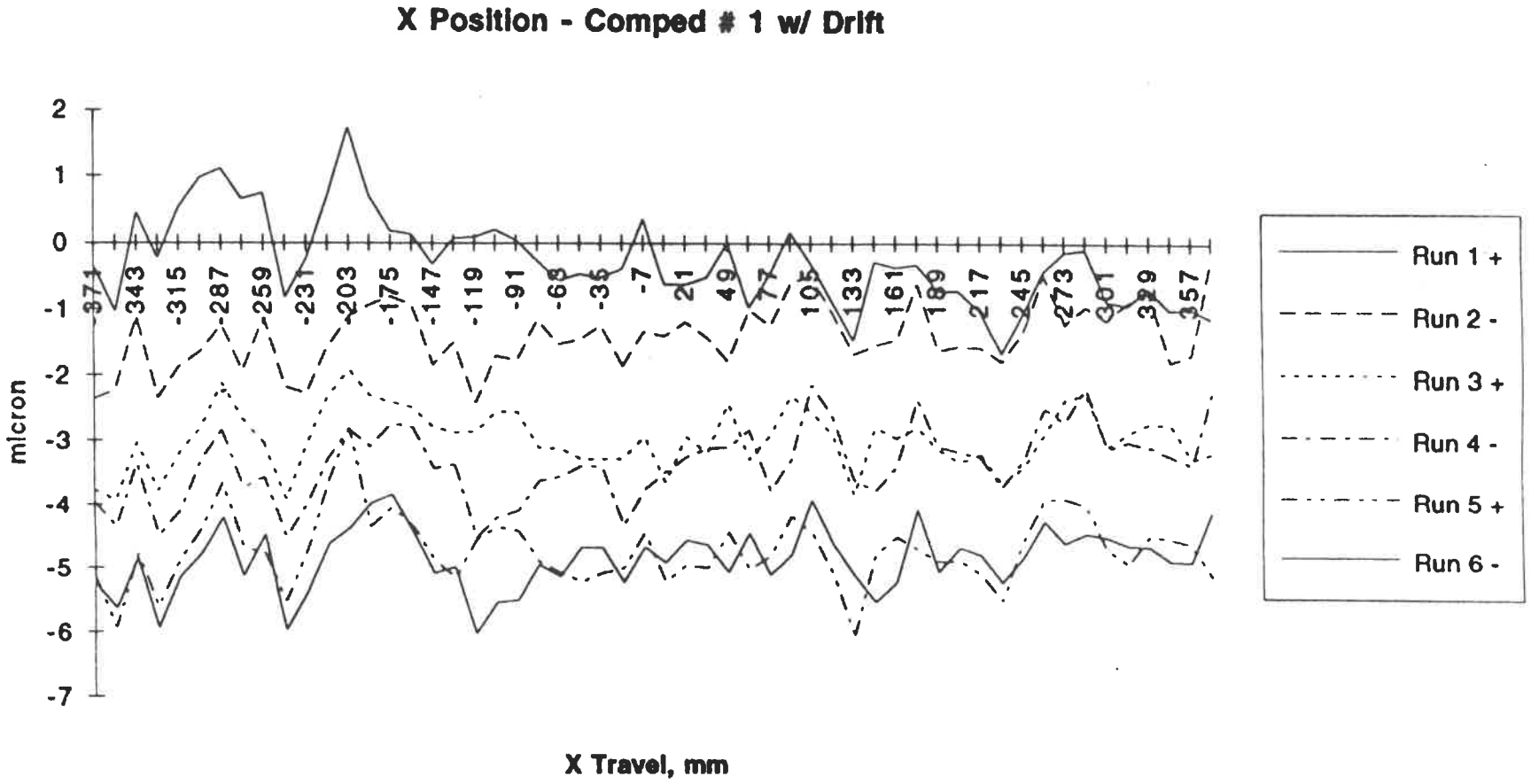

FIG. 12: Data taken after final compensation seemed repeatable but there appeared to be thermal drift between data sets. Drift was always in minus direction and as great between Runs 1 & 2 as between sets of runs.

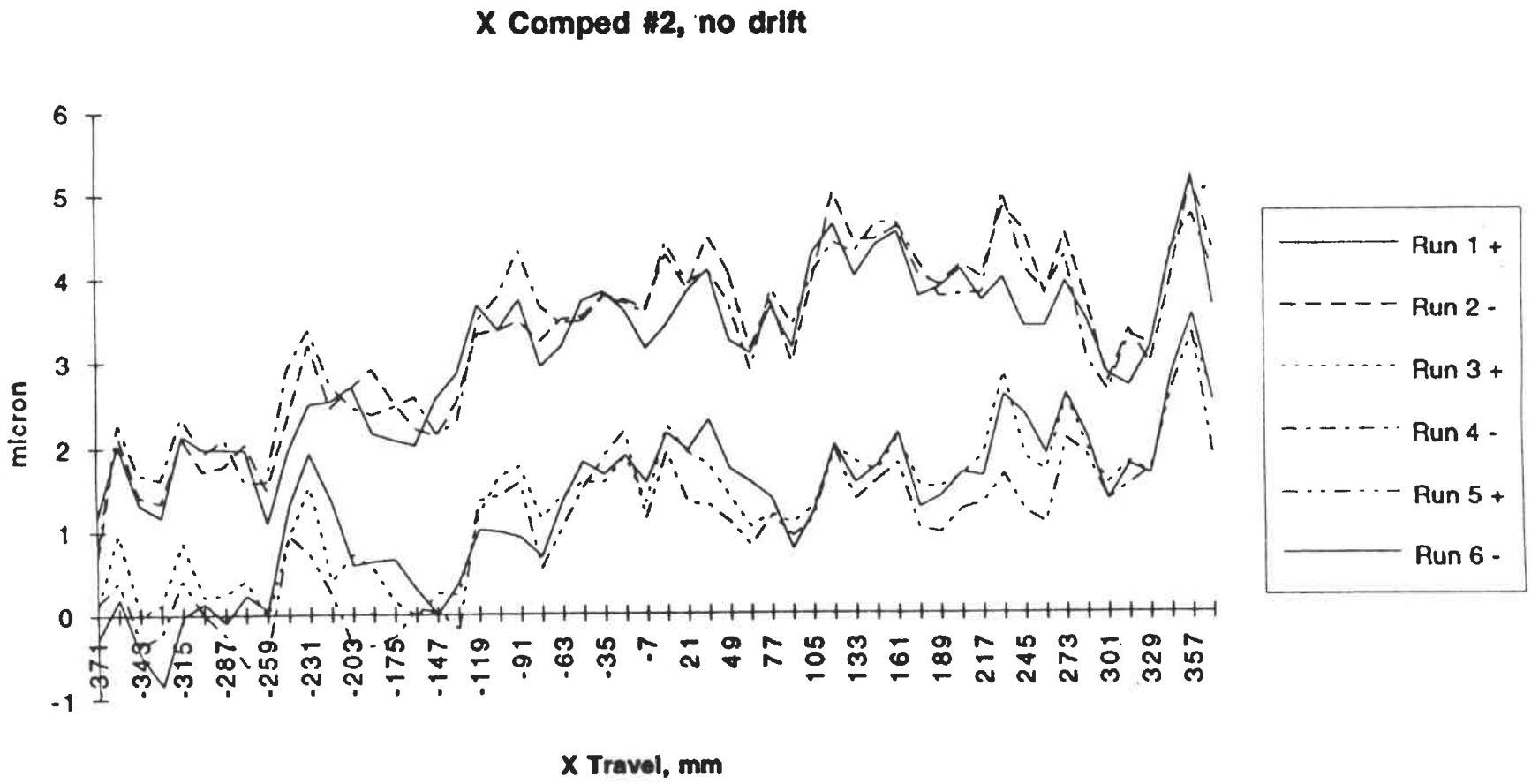

FIG. 13: After moving air weather station, the drift disappeared and only the least count resolution of the machine and a small reversal error component remains.

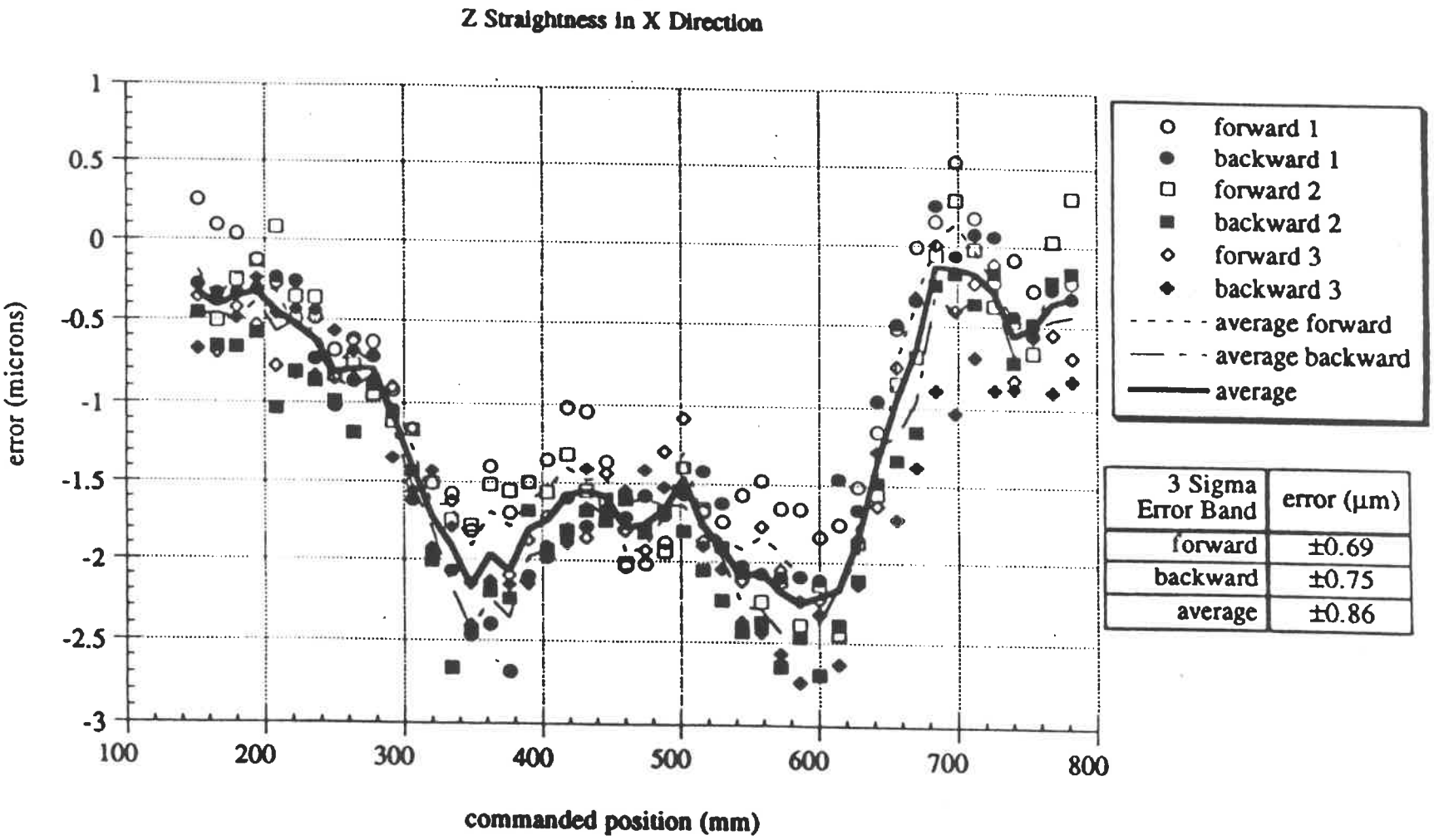

FIG. 14: This straightness chart exhibits the effect of warm exhaust air on the bracketing of the measuring probe and the straightedge. Note the apparent settling between Run 1 and the other five runs at start position.

HIGH-PRECISION MEASUREMENT SYSTEM FOR A ROTARY TABLE

Chengrui Zhang and Frank Margrave
Engineering Department
Lancaster University
United Kingdom

Abstract

A high-precision measurement system to detect the position and kinematic error of a rotational table has been developed. The system is composed of an MCS-8098 microprocessor subsystem, rotary inductosyn and capacitor encoder. A new difference frequency sub-division (DFS) technique is proposed to process the signals of a group of phase-modulated sensors (e.g. from the inductosyn), by which a measurement resolution as high as 0.07 arcsec can be achieved. The new method can be used for measuring not only angular displacements but also linear distances. The system is characterised by high precision, resistance to jamming and adaptability. The system suggests an economic, effective, and reliable means for measurement and close-loop control of NC and other machine tools.

Introduction

With the development of modern technology two main developing trends in manufacturing engineering are high efficiency and high accuracy[1]. Precision position and dimensional measurements are prerequisite conditions for acquiring high accuracy, many measuring elements and methods, such as magnetic grid, optical grating and the use of lasers have been employed in an attempt to improve upon accuracy of measurements[2][3][4]. An inductosyn employed as a measuring element is characterised by its adaptability, low cost, and resistance to jamming and it has been used as a precision element for many linear and rotary measurement solutions. The limitations of resolution and accuracy have restricted it's use in very high precision applications to other devices. The research behind the proposed methods have shown improvements in resolution to 0.04 μm in linear measurement and 0.07 arcsec for angular applications.

1. The principle of the DFS

The basic principle of DFS is shown in Fig. 1. When an inductosyn is operated in a phase-modulation mode and its fixed component is excited by two square waves $A(\omega t)$ and $B(\omega t - \frac{\pi}{2})$ of the same frequency but 90° phase difference, the induced signal of its moving component is also a square wave $C(\omega t - \varphi_0 + \varphi_m)$ with the same frequency of the exciting signals but a phase delay of $(\varphi_m - \varphi_0)$, where φ_0 is initial phase and φ_m is the phase due to the displacement. When φ_m varies through one cycle, this corresponds to 1° of mechanical rotation of an angular inductosyn (with 360 pole pieces in a circle) or 2mm of a linear inductosyn (where the pitch of the coil is 2mm) and $\varphi_m = 0$ when there is no relative motion between two components of the inductosyn. Movement of the inductosyn components will then change the phase (or frequency) of the induced signal $C(\omega t - \varphi_0 + \varphi_m)$. Thus displacement information φ_m is modulated on the stationary inductosyn components signal $C(\omega t - \varphi_0)$ and the relative motion of two components can be measured by detecting φ_m.

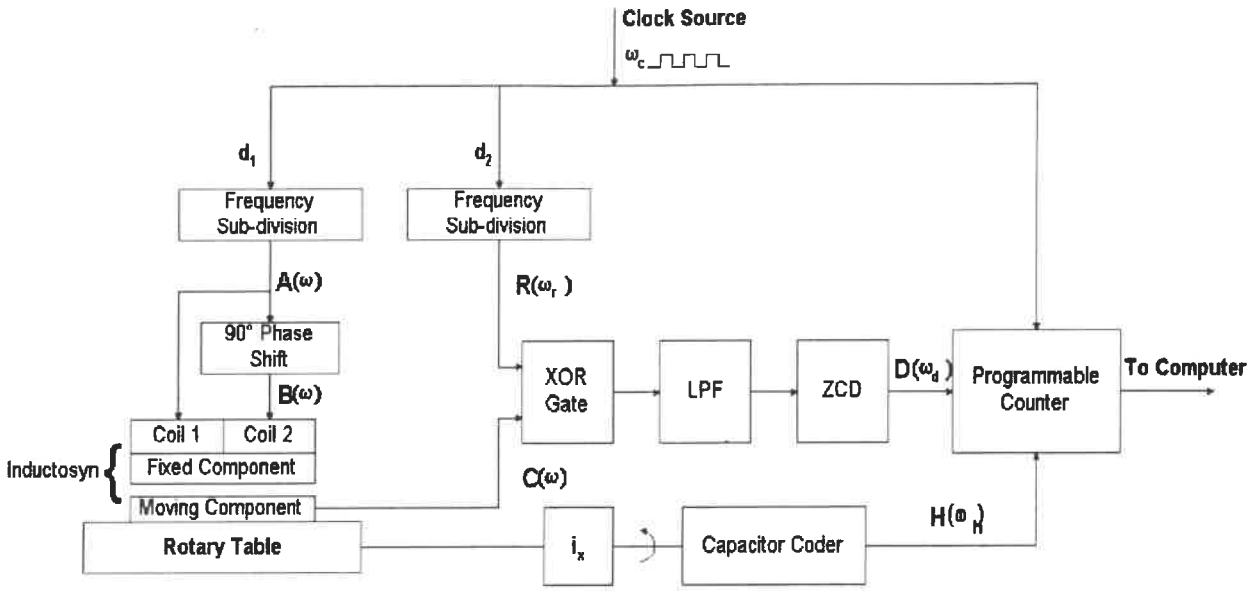

Figure 1. Principle of the DFS method.

The conventional method of detecting φ_m is by direct subdivision of the induced signal $C(\omega t - \varphi_0 + \varphi_m)$, the higher the frequency ω, the lower the resolution of division. Higher resolution may be obtained by one of two methods, either by decreasing the exciting frequency or decreasing the carrier frequency but keeping the exciting frequency in suitable value. It is impractical to adopt the first solution as the lower the exciting frequency, the weaker the induced signal. This is then susceptible to interference from other local electrical noise.

The DFS method decreases the carrier frequency by mixing the induced signal $C(\omega t - \varphi_0 + \varphi_m)$ with the difference-frequency reference signal $R(\omega_r)$, which has a frequency close to that of the induced signal, through an XOR gate. The mixed signal then passes through a lower pass filter (LPF) and zero-crossing-detector (ZCD) to a programmable counter for detection. The frequency of the signal is changed to $(\omega - \omega_r)$ but φ_m remains unchanged through above processes, this can be seen from the following analysis.

Assuming the amplitude of square wave is 1, the square wave C and R can be decomposed with sinusoidal signal, i.e.

$$C(\omega t - \varphi_0 + \varphi_m) = \sin(\omega t - \varphi_0 + \varphi_m) + \tfrac{1}{3}\sin 3(\omega t - \varphi_0 + \varphi_m) + \cdots \quad (1)$$

$$R(\omega_c t) = \sin(\omega_c t) + \tfrac{1}{3}\sin(3\omega_c t) + \cdots \quad (2)$$

then:-
$$\begin{aligned} C \oplus R &= C \bullet \bar{R} + \bar{C} \bullet R = C(\omega t - \varphi_0 + \varphi_m) \bullet R(\omega_r t - \pi) + C(\omega t - \varphi_0 + \varphi_m - \pi) \bullet R(\omega_r t) \\ &= -C(\omega t - \varphi_0 + \varphi_m) \bullet R(\omega_r t) - C(\omega t - \varphi_0 + \varphi_m) \bullet R(\omega_r t) \\ &= -2[\sin(\omega t - \varphi_0 + \varphi_m) \bullet \sin(\omega_r t) + \tfrac{1}{3}\sin(\omega t - \varphi_0 + \varphi_m) \bullet \sin(3\omega_r t) \\ &\quad + \tfrac{1}{3}\sin 3(\omega t - \varphi_0 + \varphi_m) \bullet \sin(\omega_r t) + \cdots] \end{aligned} \quad (3)$$

From equation (3), the frequency of the first harmonic is $(\omega - \omega_r)$, the frequencies of the remaining harmonics are at least tripled, so after passing through the LFP, with a pass band set for the first harmonic, these are removed. The frequency however is much lower than that of induced signal, but the phase is unchanged.

The exciting signal and the difference frequency reference signal are produced from the same clock source, each being divided by a different known factors, d_1 and d_2, thus the frequency of the detected signal is

$$\omega_d = (\omega - \omega_r) = \frac{d_2 - d_1}{d_2 \cdot d_1}\omega_c, (d_2 > d_1) \qquad (4)$$

If the detected signal is counted with the reference to the clock generator the subdivision number, d_s, is

$$d_s = \frac{\omega_c}{\omega_d} = \frac{d_2 \cdot d_1}{d_2 - d_1}$$

The measurement resolution or pulse equivalence, P_r, is defined as the mechanical displacement that one clock pulse can represents, thus

$$P_r = \frac{3600}{d_s} \text{ (arcsec) or } P_r = \frac{2000}{d_s} (\mu m)$$

For example, let $\frac{\omega_c}{2\pi}$ = 10 MHz, (the maximum frequency for #8254), $\frac{\omega}{2\pi}$ = 10 kHz and $\frac{\omega_d}{2\pi} \approx 196$ Hz, then $d_1 = 1000$ and $d_2 = 1020$ and $d_s = 51000$. By calculation the pulse equivalent is found to be:-

P_r = 3600/51000 = 0.07(arcsec) for angular device or P_r = 2000/51000 = 0.04(μm) for linear device.

2. Measuring methods

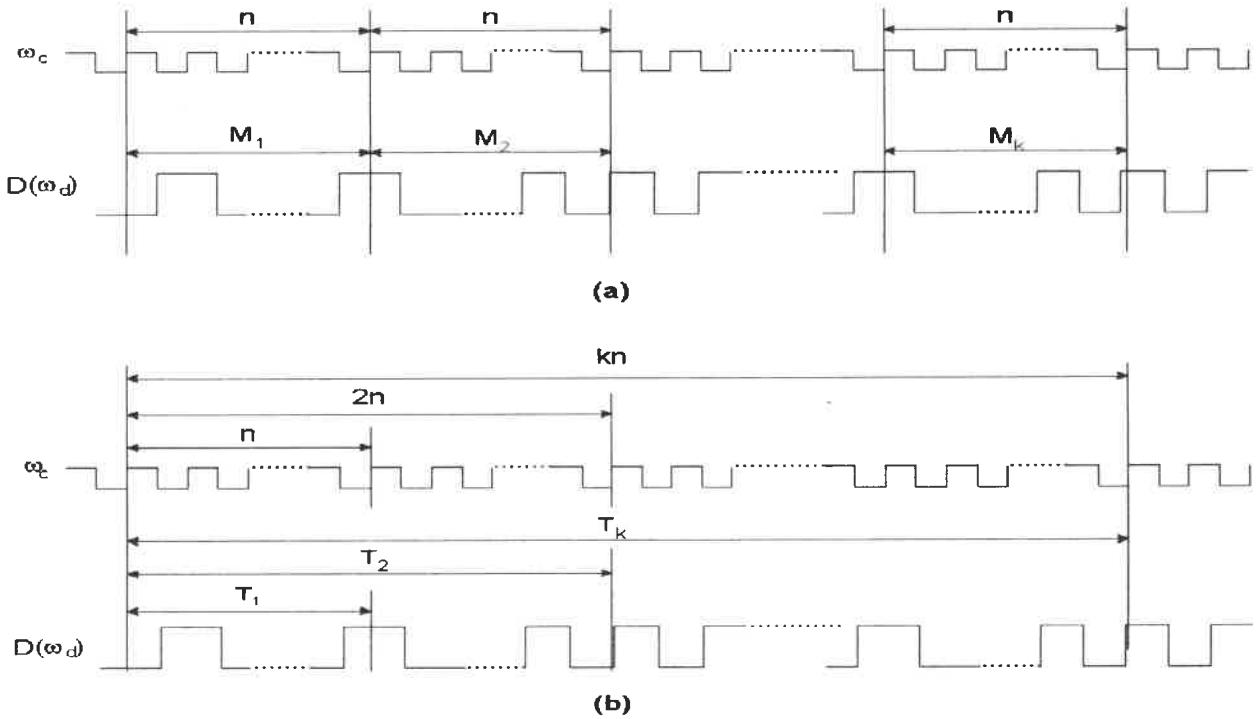

Figure 2. Relative and Absolute Reference Point Phase Comparison.

2.1. Relative and absolute reference point phase comparison

The displacement and the kinematic error of a mechanical transmission chain can be detected either by the relative or absolute reference point phase comparison, taking displacement measuring as an example shown in Fig. 2. The sampling is based on a clock source with an uniform timing of n clock cycles.

The relative reference point measuring, shown in Fig. 2 (a), takes the last sampling point as reference point, while the absolute measuring method, in Fig. 2, (b) takes the start of measuring as a reference point for phase comparison at each sampling. In order to eliminate the accumulative computing error caused by worth length limiting, the absolute measuring method is adopted for measurements of displacement and error of displacement.

2.2. Measurement of displacement and the kinematic error of the transmission chain

The measuring principle of the linear and angular displacement can be clearly seen from Fig. 2 (b). When there is no relative motion between the two components of inductosyn, the timing of the cycle of the detected signal is T_b, which is equal to d_s, refereneced to the clock source. So the displacement D_k at the kth sampling can be represented as follows,

$$D_k = P_r(kn - T_k \cdot T_b) = P_r(kn - T_k \cdot d_s)$$

The measuring principle of the kinematic error of the transmission chain is shown in Fig. 3. The kinematic error of the transmission chain is a difference of the real displacement and nominal displacement,this can be derived from the displacement of the driven end of transmission and the transmission ratio i_x in Fig. 1.

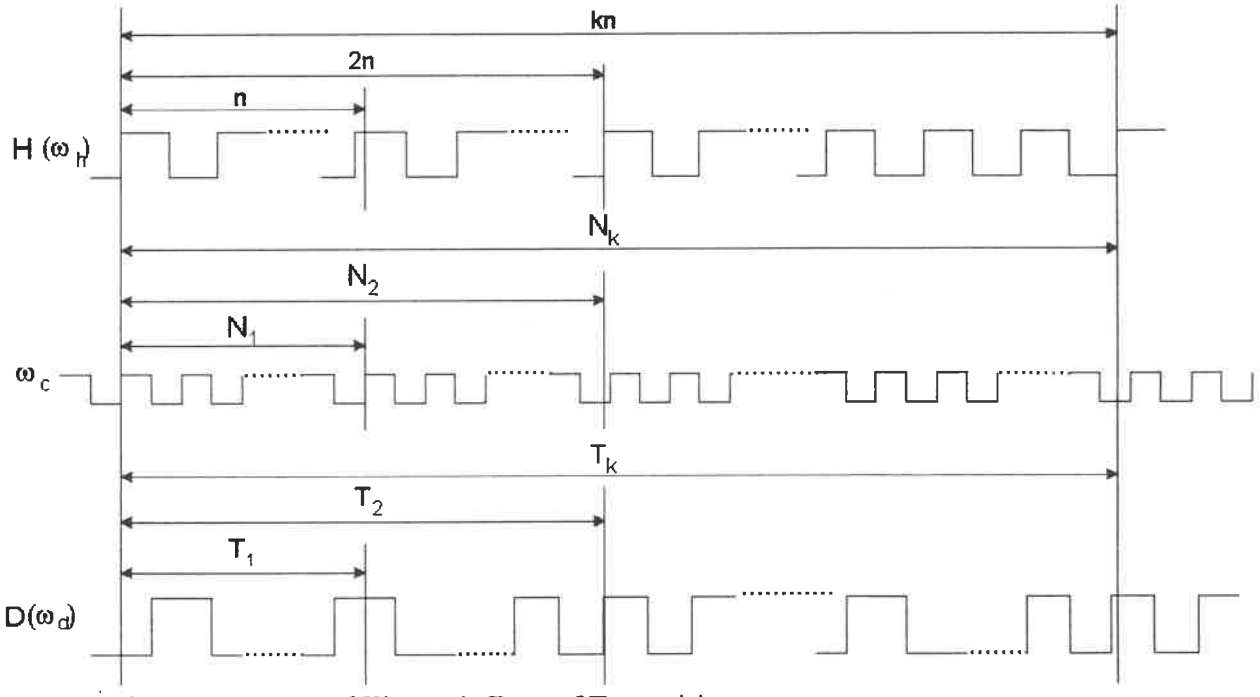

Figure 3. The Measurement of Kinematic Error of Transmision.

The sampling clock can be any of the clock signals and either of the signals of the two ends of transmission. In order to simplify the implementation of the measuring hardware, The signal of high speed end (HSE) which produces m pulses per rotation, is suggested for sampling clock, i.e. sampling every other n cycles of HSE. At the kth sampling, the count of the clock source is N_k and the count of the signal of the low speed end (LSE) is T_k, then the error E_k is

$$E_k = P_r(N_k - T_k \cdot d_s) - \frac{360}{m} i_x nk \qquad (5)$$

From the expression (5), it is can be seen the absolute measurement method prevents accumulation of computing error, if the constant $\frac{360}{m} i_x n$ retains computing accuracy. This measuring system is not limited by the speed of the transmision or its gear ratio, which is the shortcoming of most of other measuring systems such as magnetic grid systems.

3. Measuring experiment

Based on the measuring principle described above, an MCS-8098 based computer measuring system has been developed to detect the displacement and kinematic error of a rotary table. The 8098 system was extended with a measuring interface, I/O ports, CRT monitor, keyboard, pen plotter and D/A converter. The experiment was conducted on a gear hobbing machine to detect the kinematic error between the working table and the worm shaft. A capacitor coder, which produced 360 pulses per revoloution, was mounted on the worm shaft and a rotary inductosyn on the working table with a single-thread worm and gear of 96 teeth.

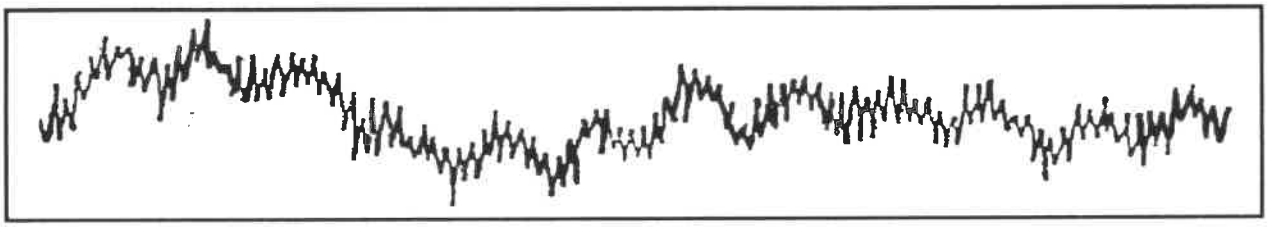

(a) comprehensive error

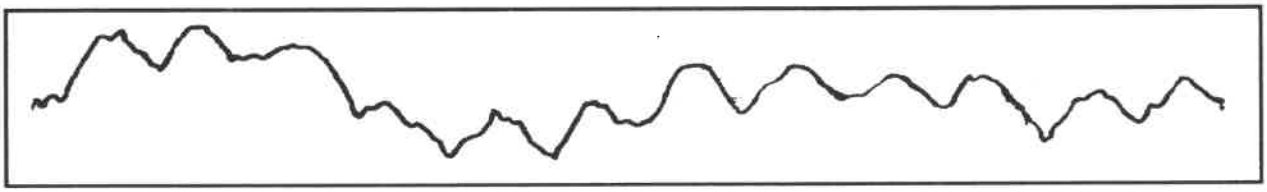

(b) long periodical error

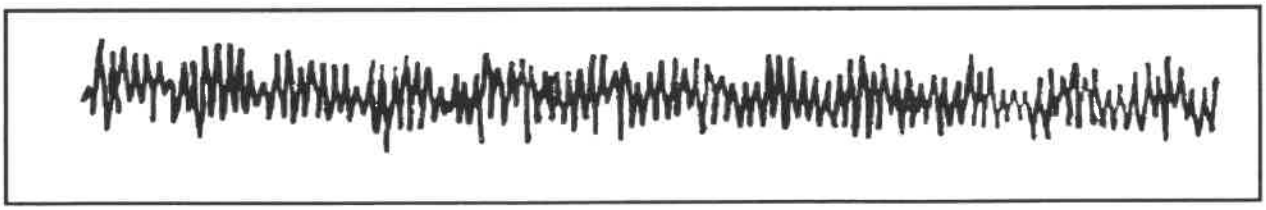

(c) adjacent periodical error

Fig. 4 The kinematic error of the rotary table

The measurment results of the working table operating at 0.8 rpm are shown in Fig. 4. Fig. 4 (a) is the comprehensive error of worm gear pair; 4(b) and 4(c) are long and adjacent periodical errors individually separated from the error curve (a) by digital notch filtering technique. The long periodical error, which is formed by the machining and installation of the worm gear, includes two large waves on which there are twelve smaller fluctuations; the adjacent periodical error including 96 fluctuations which corresponds to the error from the teeth of the worm gear. These practical results were found to coincide with the theoretical case.

4. Conclusion

Using the proposed method it is shown that the resolution and accuracy of an inductosyn can be greatly improved. When combined with its proporties of adaptility, low cost and reliability it can be seen that the inductosyn has an increased range of applications in precision measurement.

5. References

[1] Mekeown P.A., High precision engineering in the 1990's. Proceedings of CIRP conference on PE & MS, Tianjin China, Sept. 1991.
[2] He Zikang, Measurement and improvement of transmission accuracy of machine tools. China Metrology Press, Beijing 1987 (in Chinese)
[3] Han Z.J. & Zhou K. Improvement of positioning accuracy of rotating table by micro-computer compensation. Proceeding of 26th MTDR pp115-120 Sept. 1986.
[4] Bin H.Z. etc. al. Real time control for machine errors, The international conference on advanced mechatronics ICAE pp439-441, Tokyo, 1989

A TRIAL OF FORCE SENSOR WITH ACTIVELY CONTROLLED COMPLIANCE

Kiyoshi MATSUMOTO,Yotaro HATAMURA and Masayuki NAKAO
Department of Engineering Synthesis
Faculty of Engineering
The University of Tokyo
7-3-1 Hongo, Bunkyo-ku, Tokyo, 113
JAPAN

1. Introduction

In the field of precise machining, accurate control of tools and workpiece is required, where force information during machining process is essential. To detect force information, many types of force sensors with parallel plate structures have been developed.[1)2)] But because of low rigidity, usual force sensors might cause disturbances to machining system itself. We have developed a new type of force sensor which detects force and actuates its force- applied surface independently. With this sensor it will be possible not only to improve its rigidity but also to change its compliance actively according to machining conditions.

2. Principle of the sensor

2.1 Concept

Fig.1 is an example to show our concept. In cutting process, cutting force causes deformations of tool and workpiece. When we control the tool to follow aimed configuration, cut surface does not follow the aimed configration because of the deformations. When a force sensor is inserted into this system, deformation of tool will increase and thus cutting error will increase.

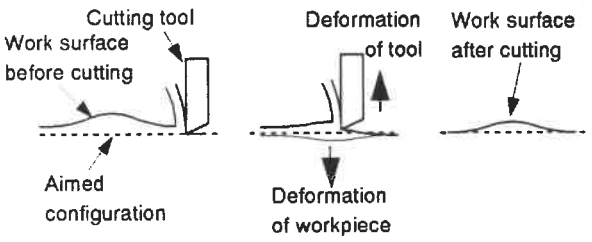

Fig.1 Schematic of cutting process

We pursued to solve this problem as follows.

1) By means of detecting deformation of the tool and of actuating it, the deformation of the tool will be canceled.

2) By means of detecting cutting force and of actuating the tool, the deformation of the workpiece will be canceled.

In order to satisfy these requirements, a new force sensor is developed, which detects force and deformation, and actuates simultaneously and independently.

2.2 Structure and sensing/actuating methods

Fig.2 shows the structure of sensor block. A center pillar is composed of upper/lower seats, and a piezo device which is glued between the seats. The center pillar is connected to outside pillars by upper/lower pairs of thin plates. The two pairs of thin plates compose symmetrically aligned parallel plate structures, and limit the movement of piezo device in one direction. On the surface of the upper/lower thin plates, strain gauges are glued to detect their deformations.

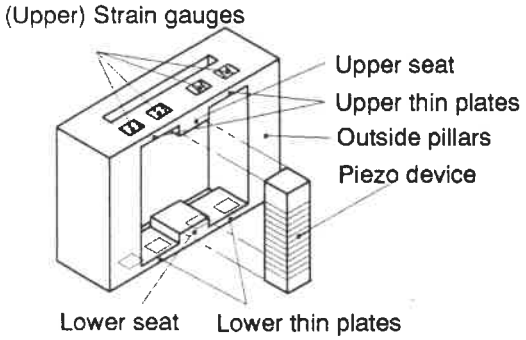

Fig.2 Parallel plate structure with piezo device

Two types of sensing and actuating methods can be realized with this sensor. Fig.3(a) shows type I. The outside pillars are fixed to rigid base, and external force is applied onto the upper

seat. Displacement y of the upper seat represents position of the force-applied surface. Difference between displacements z and y represents applied external force. The center pillar elongates with elongation of the piezo device x, and the position of force-applied surface is controlled.

Fig.3(b) shows type II. The lower seat is fixed to rigid base, and external force is applied onto the outside pillars. Displacement z of the outside pillars represents position of the force-applied surface. Difference between displacements y and z represents applied external force.

The upper seat moves with elongation of the piezo device x and gives driving force to the outside pillars through the upper thin plates, and thus the position of force-applied surface is controlled.

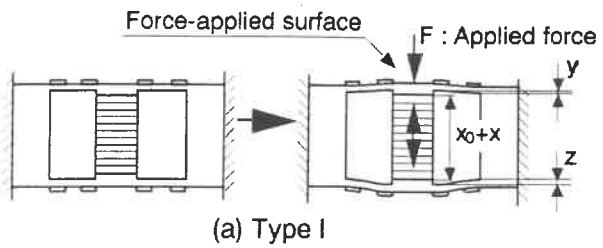

(a) Type I

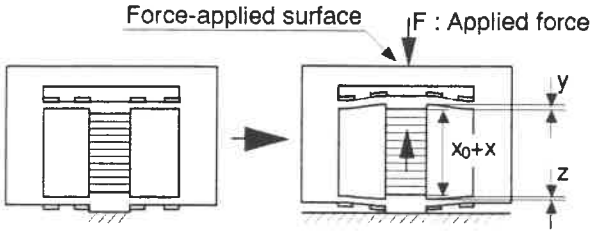

(b) Type II

Fig.3 Two types of sensing and actuating method

2.3 Characteristics

Fig.4(a), (b) show models of type I and II for analyses of dynamic characteristics, and calculated transfer functions. The piezo device is treated as an device which gives only displacement, so its mass is divided into two parts belonging to the upper/lower seats, and its rigidity is assumed infinite.

Fig.5-8 are drawn on the condition that $k=l$, $m>n$ and $m+n<o$. Fig.5 shows transfer function Y/X of type I, which represents the response of the force-applied surface to the movement of the piezo device. First resonance appears at the frequency of $\omega = \sqrt{(k+l)/(m+n)}$. Fig.6 shows transfer function Z/X of type II, which represents the response of the force-applied surface to the movement of the piezo device. First resonance appears at the frequency of $\omega = \sqrt{(k+l)/o}$. In the structure of the sensor shown in Fig.2, o tends to be heavier than $m+n$, and resonance frequency of type I will be higher than that of type II. As

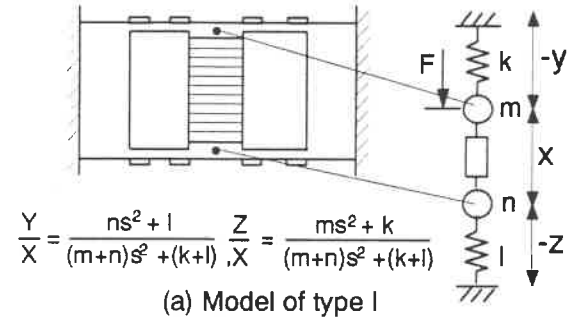

(a) Model of type I

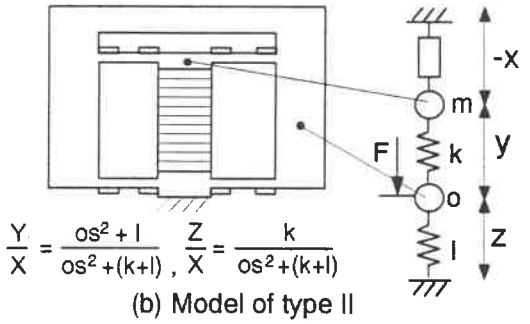

(b) Model of type II

Fig.4 Models for analyses of dynamic characteristics

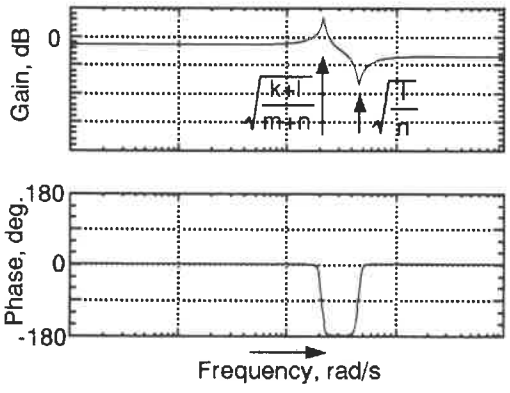

Fig.5 Transfer function Y/X of type I

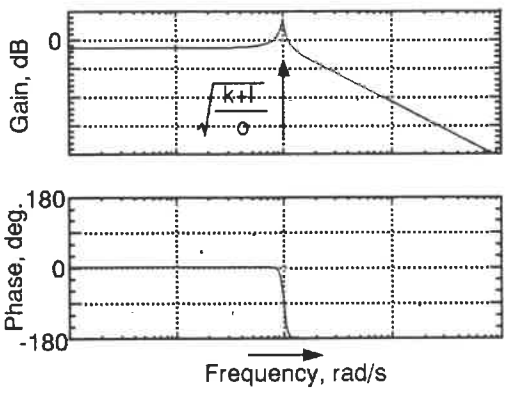

Fig.6 Transfer function Z/X of type II

higher resonance frequency is demanded to extend the bandwidth of servo system, type I is adopted in our experiment.

Fig.7 shows transfer function Z/F of type I representing force detection characteristics on the assumption that $y=0$, which means that y is controlled to be 0 over all frequency. In this case the apparent rigidity becomes infinite. Resonance appears at frequency of $\omega=\sqrt{l/n}$, and in the region under this frequency detection gain remains constant. As the actual bandwidth of servo system stays lower than $\sqrt{(k+l)/(m+n)}$, and $\sqrt{l/n}$ is higher than the upper limit of the bandwidth, this resonance does not affect the force detection performance.

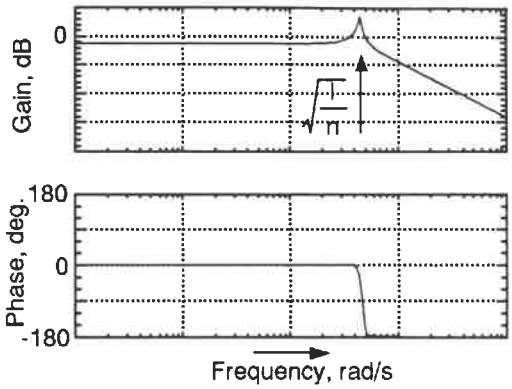

Fig.7 Transfer function Z/F of type I

Fig.8 shows transfer function (Z-Y)/X of type I, which means interference characteristics of the piezo device with force detection output. As the bandwidth of servo system is lower than $\sqrt{(k+l)/(m+n)}$, the interference is estimated to be little enough.

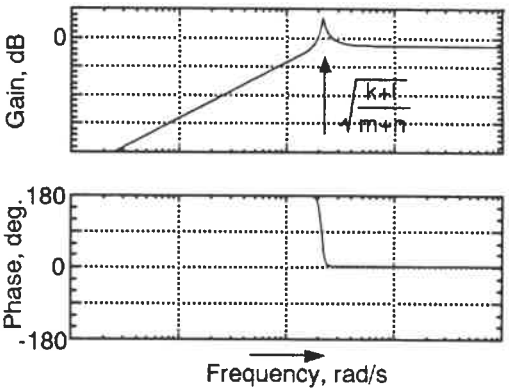

Fig.8 Transfer function (Z-Y)/X of type I

2.4 Sensing and detecting system

Fig. 9 shows block diagram of sensing and detecting system of type I. The output signal Ey of the upper gauges indicates the displacement y, and the output signal Ez of the lower gauges indicates the displacement z. Ey represents displacement of the force-applied surface and difference between Ez and Ey represents the applied external force.

Two types of control modes are possible in this system. In the position control mode, the sensor actuates while detecting force. In the force control mode, the sensor generate force while detecting displacement.

In the position control mode, Ey is fed back to the piezo device through servo circuit and the displacement of the force-applied surface can be controlled to follow the target value t. The force information can be detected independently from actuation.

In the force control mode, Ez - Ey is fed back to the piezo device through servo circuit and contact force to an object can be controlled to follow the target value t. The displacement of the force-applied surface can be detected independently from force generation.

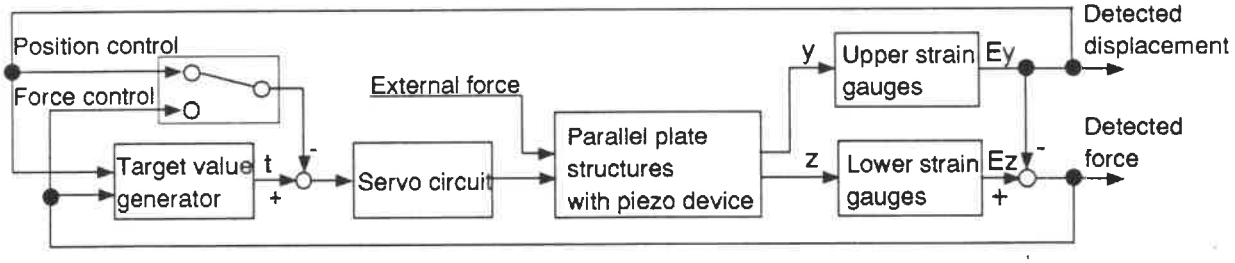

Fig.9 Block diagram of sensing and detecting system of type I

3. Experiment

3.1 Sensor block

Fig.10 shows the sensor block which is used in the experiment. Rated value of force detection is 10N, and working range of the piezo device is 6 um. The parallel plate structures were designed so as that the resonance frequency may be as high as possible and the output signal of strain gauges may be as much as possible. The thickness of thin plates is 0.6 mm, the length is 4mm, and the width is 6 mm. Rigidity of upper pair of thin plates is 1.70×10^6 N/m, and that of lower pair of thin plates is 1.71×10^6 N/m.

Fig. 11 shows measured transfer function Y/X, which is the response characteristics of the force-applied surface to the movement of the piezo device. The first resonance frequency was about 4.3 KHz.

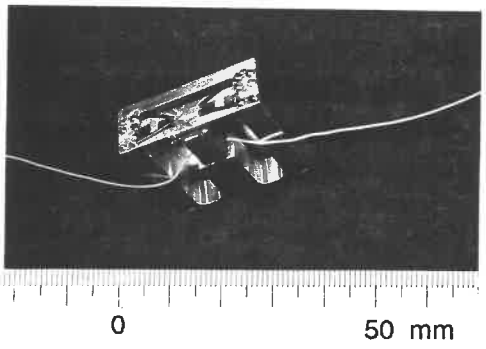

Fig.10 Picture of experimental sensor block

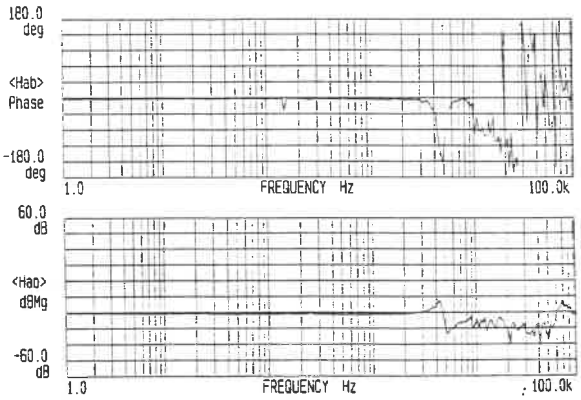

Fig.11 Transfer function Y/X of experimental sensor block

3.2 servo system

Fig.12 shows the open loop characteristics of the servo system. In the servo loop a time lag filter of first order is inserted to determine servo characteristics, and a T-notch filter is inserted to reduce gain peak of resonance. DC gain is about 60 dB. When the target value t is set to zero, rigidity against external force is improved 1000 times higher.

Fig.13 shows the closed loop characteristics of the servo system. Band width is estimated to be about 2 KHz.

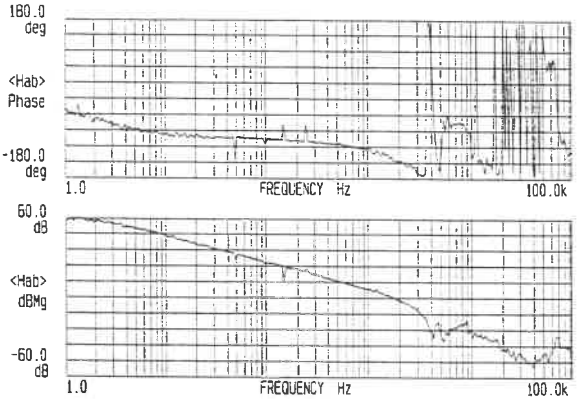

Fig.12 Open loop characteristics of servo system

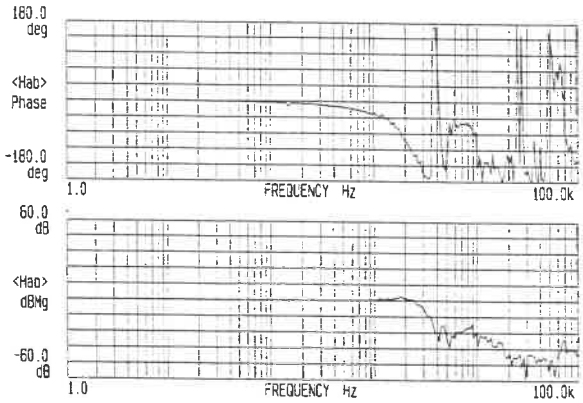

Fig.13 Closed loop characteristics of servo system

3.3 Force detection characteristics

Fig. 14 shows force detection output when external force is applied. The sensitivity is 100.3 ustrain/N.

Fig.15 shows the force detection output to external force when displacement of the force-applied surface is changed. Displacement change has little effect on force detection output. On the other hand there are upper/lower limits of displacement as shown by dotted lines. This

comes from the existence of the working range of the piezo device, and varies in proportion to applied external force.

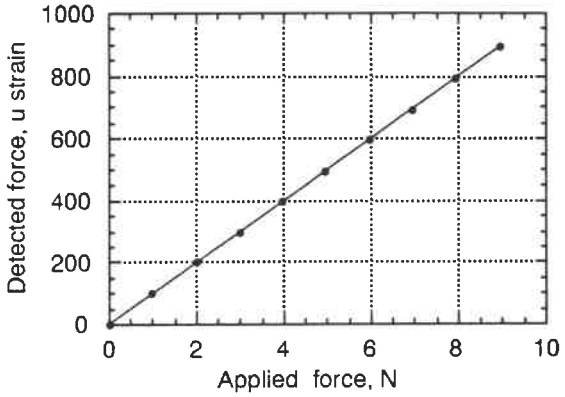

Fig.14 Force detection charachteristic

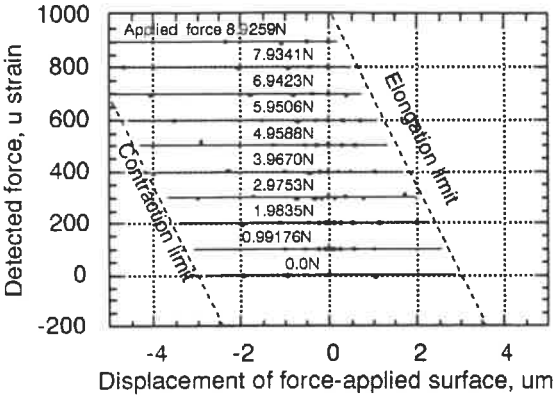

Fig.15 Force detection charachteristic

3.4 Compliance control

The position control mode is used to achieve compliance control. In Fig.9, displacement of the force-applied surface is fed back to the servo system. Position target value *t* is changed on the bases of the detected displacement and force.

Fig.16 shows the displacement of the force-applied surface to applied external force when target value *t* is changed in propotion to the detected force. The compliance can be changed by changing proportion ratio. When target value *t* is decreased in proportion to the detected force, the compliance is positive. And when target value *t* is increased in propotion to the detected force, negative compliance is achieved. When target value *t* is set to zero, the compliance becomes 1000 times higher as mentioned before, and it is estimated to be 1.70×10^9 N/m.

Many kinds of operations can be realized in compliance control. Examples of operations are shown in Fig.17-20.

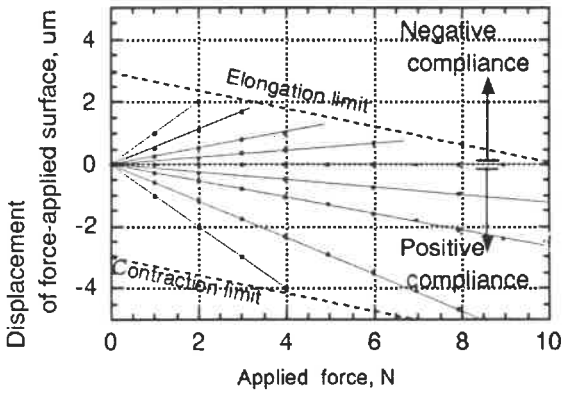

Fig.16 Compliance control operation

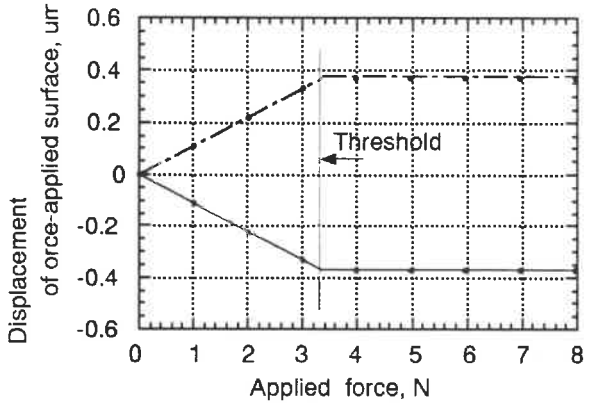

Fig.17 Example of position control operation

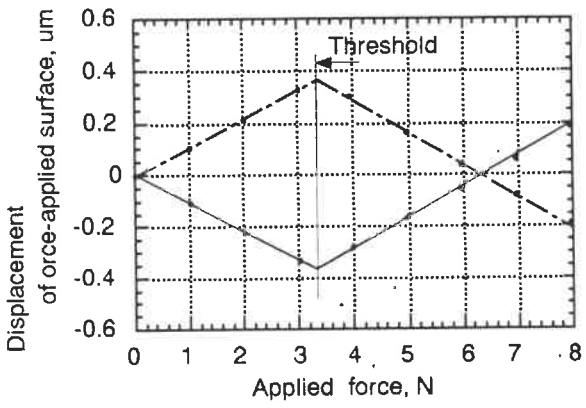

Fig.18 Example of position control operation

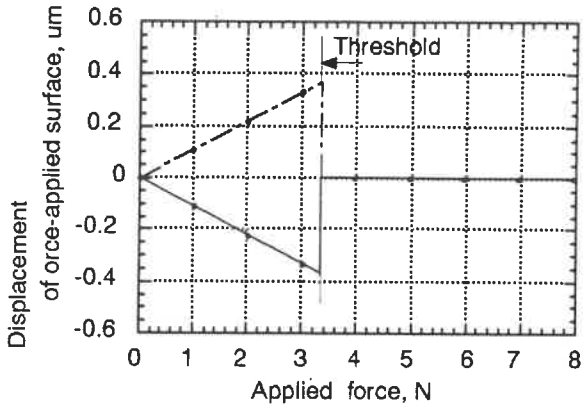

Fig.19 Example of position control operation

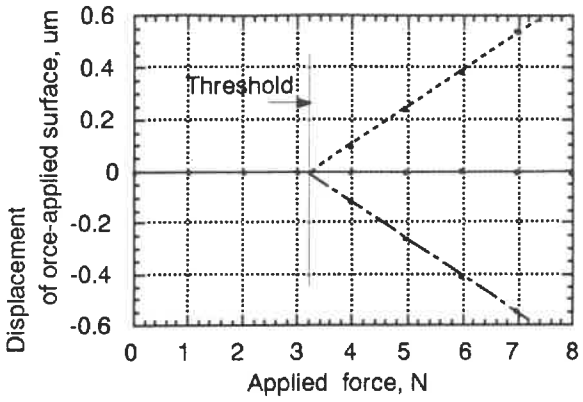

Fig.20 Example of position control operation

In Fig.17, the displacement is constant in the region upper than a threshold force. This operation is used to limit working range of actuation. In Fig.18, polarity of compliance changes at a threshold force. In Fig.19, the displacement is set to zero in the region upper than a threshold force. In Fig.20, the displacement is constant in the region lower than a threshold force. These operations are used as a safety gear for example.

In this way, arbitrary programmed compliance can be realized. This will contribute to the future intelligent manufacturing as an essential technology.

3.5 Force control

The force control mode is achieved when detected force is fed back to the servo system in Fig.9 . Force target value *t* is changed on the bases of the detected displacement and force.

Fig.21 shows the detected force to the displacement of the force-applied surface when target force value *t* is set to several values. Force is constant within working range of piezo device. But the working range of the sensor is so small that it must be used together with an coarse actuator of wider working range to achieve wide dynamic range and precision positioning, when it is used in manufacturing.

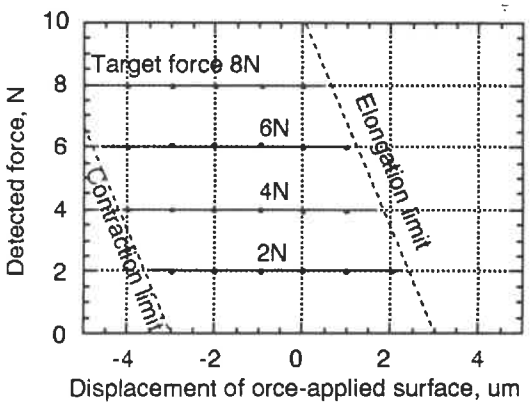

Fig.21 Force control operation

4. Conclusion

A new type of force sensor which can detect force and actuates simultaneously and independently. By using this sensor, the compliance control operation and the force control operation are executed successfully. Moreover it is confirmed that arbitrary programmed compliance can be realized through this system.

Now we are trying to apply our new sensor to the cutting system of magnetic disk substrates or copying drums, and to manufacturing system of 3D LSI where high rigidity and precise positioning are demanded.

References

1) Y. Hatamura, K. Matsumoto and H. Morishita : A Miniature 6-axis Force Sensor of Multi-layer Parallel Plate Structure, Proc. IMEKO, Houston, USA, (1988) 621.

2) Y. Hatamura : A Ring Shape 6-axis Force Sensor and its Applications, The Int. Conf. Advanced Mechatronics, Tokyo, (1989) 647.

LLNL/Lion Precision LVDT Amplifier

D. J. Hopkins
Lawrence Livermore National Laboratory
P.O. Box 808, L-792, Livermore Ca. 94550

Abstract

A high-precision, low-noise, LVDT amplifier has been developed which is a significant advancement on the current state of the art in contact displacement measurement. This amplifier offers the dynamic range of a typical LVDT probe but with a resolution that rivals that of non contact displacement measuring systems such as capacitance gauges and laser interferometers. Resolution of 0.1 μin with 100 Hz bandwidth is possible. This level of resolution is over an order of magnitude greater than what is now commercially available. A front panel switch can reduce the bandwidth to 2.5 Hz and attain a resolution of 0.025 μin. This level of resolution meets or exceeds that of displacement measuring laser interferometry or capacitance gauge systems. Contact displacement measurement offers high part spatial resolution and therefore can measure not only part contour but surface finish. Capacitance gauges and displacement laser interferometry offer poor part spatial resolution and can not provide good surface finish measurements.

Machine tool builders, meteorologists and quality inspection departments can immediately utilize the higher accuracy and capabilities that this amplifier offers. The precision manufacturing industry can improve as a result of improved capability to measure parts that help reduce costs and minimize material waste.

Introduction

This paper discusses the LVDT amplifier that was designed as part of a Cooperative Research and Development Agreement (CRADA) between Lawrence Livermore National Laboratory (LLNL) and Lion Precision a Division of Automated Quality Technologies. The Technology Transfer to Industry (TTI) program sponsored by the Department of Energy (DOE) provided the means to implement the CRADA with Lion Precision for the commercialization of the amplifier. Industry benefits because they receive technology available at LLNL and LLNL benefits because it now has a commercial source for these high-precision, low-noise amplifiers. LLNL designed the amplifier with requirements input from LLNL and Lion Precision and Lion Precision agreed to market and package the amplifier for sale. (See figure 1.)

This paper also presents a discussion of contact versus non-contact displacement measuring systems, the LVDT, the LVDT probe and an air bearing LVDT, and some application of these sensors at LLNL. Desirable characteristics of a LVDT amplifier are also included.

Contact vs. Non-contact Displacement Measurements

Measurement of precision machined parts and metrology measurements made at LLNL are done by using both non-contact and contact based displacement measuring systems. The most common non-contact displacement measuring systems in use are capacitance gauges and laser interferometers. The most common contact based displacement measuring systems are LVDT based.

Capacitance Gauge (Non-contact Sensor)

Capacitance gauges can be used as probes for part inspection or as feedback sensors for machine control as in the control system of the Large Optics Diamond Turning Machine (LODTM). A capacitance gauge is made from one or more capacitors. A capacitor is simply two conductors separated by an insulator. The equation for capacitance is;

$$C = eA/d \qquad (1)$$

e is the dielectric constant of the insulator, usually air
A is the area which is common to both conductors
d is the distance between the conductors.

Capacitance gauges measure displacement by solving for (d) in equation (1). A single capacitor system will require electronics to linearize the output. A double or differential capacitance gauge system can be configured to provide a linear output as a function of displacement. Advantages of capacitance gauges are extremely good displacement resolution for part figure measurements that approaches the atomic diameter level (0.3 nm) and because they are non contact based sensors there is no part deformation. Disadvantages of capacitance gauges are; probe travel is typically limited to a few thousands of an inch with reasonable probe diameters, the probe must be kept normal to the part surface or a displacement error will result, and as can be seen from equation (1), the capacitance gauge is an area averaging device and therefore high part spatial resolution for surface finish measurements is not possible. Also, the material under inspection must generally be conductive and grounded and finally the dielectric must be constant i.e. the part should be clean and free of oil and contaminants.

Displacement Measuring Laser Interferometry (Non-contact Sensor)

Displacement measuring laser interferometry is an optical and electronic method for measuring displacement. An AC or heterodyne interferometer system is preferred over a DC interferometer because it translates the displacement information to a higher frequency band for increased accuracy, reduced noise and repeatability. The following is a simplified theory of operation. Two collinear orthogonally polarized different frequency beams of light originate from a laser that is typically a HeNe with a wavelength (λ) of approximately 25 μin. A portion of this laser beam is diverted and passed to a detector. The detector is a fast photo diode plus a focusing lens and a polarizer that is at 45 degrees relative to the plane of polarization of the beam. This polarizer causes the two beams to mix creating a beat frequency that is sensed by the detector. This beat frequency or difference frequency is known as the reference frequency and is generally 2 or 20 MHz depending on the laser manufacturer. The non-diverted portion of the laser beam passes through an interferometer where one polarization of light passes through a fixed path length in the interferometer. The other polarization leaves the interferometer and is reflected off a corner cube or a plane mirror that is located on the object whose distance is to be measured. This beam then returns to the interferometer where it recombines with the fixed path beam. A detector mounted on the output of the interferometer with a polarizer at 45 degrees to the plane of polarization of the beam will sense a phase change with respect to the reference frequency as the object whose distance to be measured is changed. A doppler shift in frequency occurs when the object is in motion. The two types of return mirrors, mentioned above, along with the laser wavelength determines the displacement resolution of the system. A corner cube or retroreflector system has an optical resolution of $\lambda/2$ and a plane mirror system has an optical resolution of $\lambda/4$. Commercially available interferometer electronics can then be used to extend this resolution by a factor of 128. It is therefore possible with plane mirror interferometers to achieve a displacement resolution of $\lambda/512$ or 0.05 μin.

The advantages of displacement measuring interferometry are the resolution and dynamic range it provides. A dynamic range of several feet with the above mentioned resolution is possible and is in use on LLNL's LODTM. However, some of the disadvantages are; it is an optical measurement and is typically used only for machine control and metrology measurements with a known return mirror. Direct part inspection is normally not possible due to beam alignment, part contour and part finish. Also, to obtain accuracy and the above resolution, it is important to minimize index of refraction changes along the path length and polarization mixing of the two different frequency beams. Alignment is important to minimize cosine error and maintain overlap of the two polarized beams recombining in the interferometer. Polarization mixing can cause a periodic error in the displacement measurement. It is related to alignment and the quality of the optical components. Another disadvantage to this system is that it is a relative displacement measuring system and can only measure displacement from a starting position.

LVDT Sensors for Displacement Measurement (Contact Sensor)

Electrical Characteristics

Linear Variable Differential Transformers (LVDTs) are used as contact based sensors for precision displacement measurement. An LVDT is a magnetic induction transducer with a primary winding, a movable magnetic core, and two secondary windings symmetrically spaced from the primary. A stylus, held in contact with a part to be measured, is mounted on a shaft extending from the magnetic core. (See figure 2.). The movement of the core causes changes in the magnetic coupling of primary to secondaries and induces a voltage in each secondary proportional to the core location. Connection of the secondary windings, in series opposing, will generate a null or zero-volt signal at the core center position where equal coupling exists into each secondary. This core null position is stable and repeatable and allows the LVDT to be an absolute positioning sensor. Any deviation of the core from the null will generate an abrupt change in phase of the secondary signal with respect to a reference signal, generating a linearly increasing voltage as the core is displaced from center. (See figure 3.) The LVDT operates on the principle of magnetic coupling; resolution is essentially infinite and depends on the signal-to-noise ratio of the signal conditioning electronics. Additional information on the electrical characteristics follows in the section; The Amplifier and Desirable Amplifier Characteristics.

Mechanical Characteristics

An LVDT is technically the transformer and the moveable magnetic core. Generally the term LVDT or LVDT probe as referred to in the literature is the transformer, the mechanical housing, the shaft that extends from the magnetic core, a radial bearing for the shaft and a stylus that mounts on the workpiece end of the shaft. The housing of the LVDT probe is held in a fixture that may be part of a structure or mounted on a moveable part of a machine e.g. one of the machine slides. Axial movement of the shaft is free within the mechanical constraints of the housing and is sensed as discussed under electrical characteristics. An important consideration of the LVDT probes includes the stylus force applied to the part under inspection. Most LVDTs require the part to support the full force of the stylus, shaft and core weight. This can result in part deformation at the point of contact and lead to incorrect displacement measurement when high precision is required. Use of the probe at any angle other than normal to the surface of the part is another important consideration because a lateral deflection force on the shaft/stylus exists that can lead to an axial movement component and therefore an error. This error is minimized by having high shaft bearing stiffness.

LVDTs are contact displacement measuring devices so it is possible to measure part contour figure and measure part surface finish. Part surface finish measurement requires high part spatial resolution which is a function of the stylus tip. This ability to measure part surface finish is one of the advantages of this type of sensor over capacitance gauges and laser interferometers.

Air Bearing LVDTs

An air bearing LVDT provides the ultimate in mechanical configurations. It provides essentially a friction free movement in the axial direction providing non-stick operation when high precision and repeatability are required. It also provides, high shaft radial bearing stiffness that reduces lateral deflection errors. To minimize part deformation, adjustment of stylus force to 0.1 gram is possible with this type of probe. Another consideration in the use of the probe, is to deflect the air exhausted from the probe away from the surface of the part to be measured to minimize the Joule-Thomson effect. LLNL has built air bearing probes with super invar housings and Zerodur shafts for the ultimate reduction in temperature induced errors.

Application of LVDTs at LLNL

There are many applications of LVDTs and air bearing LVDTs in use at LLNL. Principle applications include machine tool metrology, CMMs, inspection machines, tool set stations, diamond turning machines, roundness gauges, diamond tool mapping and precision manufacturing. Parts made at LLNL by machines such as the Large Optics Diamond Turning Machine, typically require

the ability to measure part figure to better than 1 μin and part surface finish to better than 0.05 μin.

The Amplifier and Desirable Amplifier Characteristics

This amplifier is a precision high-gain, low-noise instrument designed to work with LVDT sensors for precision contact displacement measurement. The amplifier provides resolution an order of magnitude or better over similar amplifiers with a reduced level of sensor excitation. LVDTs are specified with a nominal linear range of travel of ± X inches, then a sensitivity of secondary volts per primary volts of excitation per core displacement. Effective resolution of the amplifier is equal to probe sensitivity times amplifier gain times volts of primary excitation resulting in volts per displacement. At the highest gain range of this amplifier, with a ± 0.020 inch LVDT, the effective resolution of the amplifier is 0.5 volts per microinch.

Small levels of primary excitation of the LVDT minimize probe heating, decrease thermal distortion of a part and provide higher measurement precision and repeatability. Constant current excitation of the LVDT maintains the same voltage across the primary coil; hence the same level of coupling is provided to the secondaries even if the coil resistance should change because of temperature changes.

An oscillator provides a fixed frequency, highly stable LVDT primary winding excitation or carrier signal. This carrier is coupled to the secondaries and amplitude modulated by the core position. The signal is then AC amplified and demodulated with a phase sensitive detector, obtaining the magnitude of displacement and sign data about the core null position. This signal is then low passed filtered to remove the carrier, providing a bipolar output with respect to the null position. Maximum frequency response or bandwidth of the amplifier is a function of the frequency of excitation of the sensor and the low pass filter setting. The output bandwidth is front panel switch selectable in this amplifier and is set for desired signal vs. noise performance.

The heart of the amplifier is a phase sensitive detector. This kind of detector has excellent signal to noise rejection. It will pick out a signal hidden by high levels of noise. The detector is driven with two signals. The input signal (the amplified secondary signal) and a reference signal derived from the oscillator. The output is a function of the input signal amplitude and the cosine of the phase between the input signal and the reference signal. Phase adjustment for maximum detector sensitivity is automatically done in this amplifier. Manual adjustment is done in other amplifiers with this type of detector. Incorrect phase adjustment can lead to errors and decreased amplifier sensitivity.

Systems of this type take information at a low frequency band and translate it to a higher frequency band to minimize the effects of noise. Since these systems have a carrier frequency, it is possible for two independent units to have slightly different carrier frequencies. Unless perfect shielding exists between the two units, a small signal from one unit may couple into the other unit through e.g. the sensor's cable and create a beat frequency. This beat frequency may show up as a slow drift or an erratic reading in the displacement measurement depending on the difference in the two units' frequencies. This amplifier prevents this condition because it provides for master-slave operation i.e. all amplifiers operate off a common frequency carrier.

The signal from the LVDT is composed of two components: the desired displacement signal and the undesired constant amplitude quadrature signal. The amplifier cancels this undesirable signal and allows maximum predetector gain and minimum post detector gain. High post detector gain can lead to output drifts because of electronic thermocouple effects and excess amplifier 1/f noise.

This amplifier offers four front panel selectable gain ranges, analog and digital front panel (F.P.) displays, two channel operation, arithmetic output that includes peak and valley detectors for maximum (max.) minimum (min.) and total indicator runout (TIR), autotuning, quadrature cancellation, offset adjustment, output polarity select, overload detectors, separate bipolar outputs analog ± 10 volt outputs for channel A, channel B and arithmetic output, F.P. selectable bandwidth and English/Metric (ENG/MET) settings.

Summary

In conjunction with an LVDT, this amplifier provides ultraprecision contact displacement measurements . It defines the state-of-the-art in contact displacement gauging. Using a typical probe with ± 0.020 inch of travel, it can resolve to 0.1 µin with 100 Hz bandwidth. Resolution to 0.025 µin is possible with a reduction in bandwidth to 2.5 Hz. It achieves this level of resolution with a sensor excitation that is approximately 5 to 10 times smaller than similar products.

This amplifier and sensor combination allow resolution equal to greater than non-contact capacitance gauges, but the combination provides a dynamic range (measurement range) which is typically 10 times that of a capacitance gauges with the stated resolution. The amplifier can exceed the displacement resolution of commercial displacement interferometry, but the dynamic range is limited to that of the probe travel. Contact displacement measurements with LVDTs provide high part spatial resolution and can measure both part figure and surface finish.

Acknowledgments

I thank Gary Armstrong and Ross Castleton of LLNL and Don Martin of Lion Precision for their effort in negotiating the CRADA. Special thanks for Gary Armstrong for starting the project and for project management and Ross Castleton for his support. I would also like to thank Bob Donaldson and Jim Hamilton of LLNL for their support during the amplifier design and development. Also, thanks to Ray Herbst of Lion Precision for his valuable technical input.

This work was performed under the auspices of the U.S. Department of Energy by Lawrence Livermore National Laboratory under contract No. W-7405-Eng-48.

References

1. Donaldson, R.R. and Patterson, S.R., **"Design and Construction of a Large , Vertical Axis Diamond Turning Machine,"** Proceedings SPIE, Vol. 433, August 1983, pp. 62-67

2. Hewlett Packard, **"Lasers and Optics,"** HP Application Note 197-2.

3. Zygo Corporation, **"ZMI-1000 Measurement Board,"** Operation Manual, August 1992.

4. Herceg, E.E., **"Handbook of Measurement and Control,"** Schaevitz Engineering, Handbook HB-76 Copyright 1976.

Fig. 1 The LLNL/Lion Precision Amplifier with an air bearing LVDT probe.